UC San Diego

UC San Diego Electronic Theses and Dissertations

Title

Investigations of runaway electron generation, transport, and stability in the DIII-D tokamak

Permalink

https://escholarship.org/uc/item/8v07812x

Author

Tronchin-James, Alexander Nevil

Publication Date

2011

Peer reviewed|Thesis/dissertation

eScholarship.org Powered by the California Digital Library
University of California

UNIVERSITY OF CALIFORNIA, SAN DIEGO

Investigations of runaway electron generation, transport, and stability in the DIII-D tokamak

A dissertation submitted in partial satisfaction of the
requirements for the degree
Doctor of Philosophy

in

Engineering Science (Engineering Physics)

by

Alexander Nevil Tronchin-James

Committee in charge:

George Tynan, Chair
C. Fred Driscoll
Eric Hollmann
Stefan Llewellyn Smith
Richard Moyer
Thomas O'Neil

2011

Copyright
Alexander Nevil Tronchin-James, 2011
All rights reserved.

The dissertation of Alexander Nevil Tronchin-James is approved, and it is acceptable in quality and form for publication on microfilm and electronically:

_____

_____

_____

_____

_____

_____
Chair

University of California, San Diego

2011

DEDICATION

Dedicated to all the people who have treated me like family
and made me feel at home, wherever I am.

Also dedicated to the pursuit of flying motorcycles.

EPIGRAPH

Twenty years from now you will be more disappointed by the
things that you didn't do than by the ones you did do.
So throw off the bowlines.
Sail away from the safe harbor.
Catch the trade winds in your sails.
Explore.
Dream.
Discover.
–Mark Twain

TABLE OF CONTENTS

Signature Page . . . iii

Dedication . . . iv

Epigraph . . . v

Table of Contents . . . vi

List of Figures . . . x

List of Tables . . . xvi

Acknowledgements . . . xvii

Vita . . . xix

Abstract of the Dissertation . . . xx

Chapter 1 Introduction . . . 1
- 1.1 Energy in modern civilization . . . 1
- 1.2 Nuclear Fusion . . . 3
  - 1.2.1 Natural reactors . . . 3
  - 1.2.2 Manmade reactors . . . 4
    - 1.2.2.1 Inertial confinement . . . 4
    - 1.2.2.2 Magnetic confinement . . . 4
- 1.3 Runaway electrons . . . 6
  - 1.3.1 Basic theory of runaway generation . . . 6
  - 1.3.2 Natural occurrence . . . 7
  - 1.3.3 Laboratory occurrence . . . 8
- 1.4 Tokamak Disruptions . . . 9
  - 1.4.1 Causative factors . . . 10
  - 1.4.2 Thermal Quench . . . 10
  - 1.4.3 Current Quench . . . 11
  - 1.4.4 Runaway plateau . . . 11
  - 1.4.5 Runaway termination . . . 12

Chapter 2 A brief history of runaway electron studies . . . 13
- 2.1 Theory . . . 13
  - 2.1.1 Generation . . . 13
    - 2.1.1.1 Dreicer generation . . . 14
    - 2.1.1.2 Hot-tail generation . . . 15
    - 2.1.1.3 Avalanche generation . . . 16

2.1.2 Energy limit and energy distribution 17
2.1.3 Transport, equilibrium, and stability 19
2.1.3.1 Diffusion 19
2.1.3.2 Force equilibrium 20
2.2 Prior Experiments 21

Chapter 3 Experimental techniques for studying runaway electrons in tokamak disruptions 26
3.1 Argon killer pellet injection and plasma shaping to generate runaway electrons 26
3.2 Diagnostics for studying rapid shutdowns and runaway electrons 29
3.3 Hard x-ray sensing scintillators 31
3.3.1 Motivation 31
3.3.2 Modelling bremsstrahlung from runaway electrons 31
3.3.3 Detector design 32
3.3.3.1 Scintillator selection 32
3.3.3.2 Amplifier and electronics 37
3.3.3.3 Electromagnetic shielding 38
3.3.4 Array arrangement 38
3.3.5 Runaway energy resolution 39
3.3.5.1 Photo-neutron signals 41
3.3.5.2 Radiation damage to silicon detectors . . 45
3.4 Magnetic diagnostics 46
3.5 Bolometer and soft x-ray arrays 49
3.6 Interferometers 50
3.6.1 Fringe skips, and corrections 51
3.7 Electron cyclotron emission 55
3.7.1 ECE cutoff 55
3.8 Other diagnostics 56
3.8.1 Fast visible camera 56
3.8.2 Reflectometers 56
3.8.3 EUV Spectroscopy 57
3.8.4 Other spectroscopy 57
3.9 Flux function reconstructions 58
3.9.1 EFIT 58
3.9.2 JFIT 59

Chapter 4 Hard x-ray emission from runaway electrons in DIII-D 64
4.1 Experimental findings 65
4.2 Discussion and Analysis 70
4.2.1 Limitations of thermal quench measurements . . . 70
4.2.2 Prompt-loss phenomena 72

4.2.3 Plateau phenomena . . . 73
4.2.4 Termination phenomena . . . 80
4.2.5 NIMROD modeling . . . 84
4.2.6 RE energy and loop voltages . . . 86
4.2.7 Bremsstrahlung from runaways . . . 88
4.3 Conclusions . . . 90

Chapter 5 Interaction between runaways and injected pellets . . . 92
5.1 Motivation . . . 92
5.2 Impurity pellet injection . . . 93
5.3 Visible Imaging . . . 95
5.4 Observed cyclotron emission . . . 97
5.5 Discussion of cyclotron emission in the relativistic limit . 99
5.6 Pellet heating and breakdown by runaways . . . 101
5.7 Conclusions . . . 102

Chapter 6 Determining loop voltages during tokamak rapid shutdowns . 105
6.1 Review of voltage sources in a cooling plasma . . . 106
6.1.1 Spitzer resistivity and hyper-resistivity . . . 107
6.1.2 Models of radiative cooling and killer pellet ablation 108
6.1.2.1 Radiative cooling modelled by KPRAD . 108
6.1.2.2 Killer pellet models . . . 110
6.2 Thermal quench timing with bolometer tomography . . . 110
6.3 Inferring the loop voltage using magnetic diagnostics . . 114
6.3.1 Derivation of loop voltage for changing current from Faraday's equation . . . 114
6.3.2 Limitations of magnetic diagnostics . . . 116
6.3.3 Inverse techniques for inspecting loop voltages before the current quench . . . 118
6.4 Conclusions . . . 123

Chapter 7 Conclusions and outlook . . . 125

Appendix A Table of symbols . . . 127

Appendix B History of runaway electron observation in DIII-D . . . 130

Appendix C Pellet injector . . . 134
C.1 Repairs . . . 134
C.2 Modifications . . . 136
C.3 Pellet material selection . . . 139

Appendix D Comparison of various techniques for calculating runaway current due to avalanche 143
D.1 Empirical techniques 143
D.2 Coupled inductor model 144
D.3 Calculation of runaway electron seed current 148

Bibliography 151

LIST OF FIGURES

Figure 0.1: The DIII-D Team xvii

Figure 1.1: A cartoon of the DIII-D tokamak operated at General Atomics in San Diego. 5

Figure 2.1: A 3D rendering of the DIII-D tokamak. From the outside in are: toroidal field coils (black), poloidal field/shaping coils (red), center solenoid windings (green), the Inconel vacuum vessel (grey), and graphite limiting surfaces (black). 25

Figure 3.1: A histogram of plateau phase runaway current plotted for the two different experimental shapes showing increased frequency of runaway plateau for the limited shape. 28

Figure 3.2: Histograms of the initial a) electron temperature, b) electron density, c) stored thermal energy, and d) edge safety factor. . . 28

Figure 3.3: Diagnostic and hardware arrangement for the experiments discussed. 30

Figure 3.4: A cartoon of the EGSnrc geometry used for modelling x-ray spectra from runaways striking the DIII-D wall, and a series of those spectra observed outside the DIII-D vessel. Each curve terminates at approximately the incident RE energy. 33

Figure 3.5: A cartoon of the EGSnrc geometry used for modelling x-ray fluence (color) vs. angle of incidence α and energy (radius) from runaways impacting a 2mm $\times$ 2mm carbon pellet, and a series of the resulting fluences for three different energy incident electrons. 34

Figure 3.6: Drawing of detector assembly with a) side view and b) rear view. 35

Figure 3.7: A detailed drawing of the scintillator detector design. 36

Figure 3.8: Spatial arrangement of a) midplane toroidal and b) poloidal scintillator arrays. 39

Figure 3.9: Scintillator array signals in a disruption with a) significant runaway electron current I_r (measured by subtracting a fitted L/R current decay $I_{L/R}$ from the total measured current I_m), b) time traces from the poloidal array at 90 degrees with detectors above, near (mostly saturated), and below the midplane, c) energy estimated with the shielded detectors, and d) contour plots showing spatially resolved emission at two times, with detector locations circled. 40

Figure 3.10: A cartoon of the processes contributing to finite energy resolution in scintillators, and energy resolution curves calculated for a $1in \times 1in$ BGO scintillator to various photon energies using EGSnrc Monte-Carlo modelling. Each curve terminates at approximately the incident photon energy, with the full energy peaks marked with an $\times$ where visible. 42
Figure 3.11: A cartoon of the geometry used in EGSnrc to model the apparent attenuation length in detectors shielded by various thicknesses of lead, and the resulting detector dosages per electron for various incident electron energies. 43
Figure 3.12: Photoneutron production cross sections for a selection of common tokamak materials [127, 1]. 44
Figure 3.13: A 3D rendering of the various magnetic probe arrays installed at DIII-D. 47
Figure 3.14: Flux loops (blue circles) and magnetic probes (red arrows) shown in a poloidal cross-section. 48
Figure 3.15: A 3D rendering of the various flux loops installed at DIII-D. . . 49
Figure 3.16: A 3D rendering of views for the various soft x-ray and bolometer arrays installed at DIII-D. 50
Figure 3.17: Poloidal cross-section views of the soft x-ray and bolometer arrays. 51
Figure 3.18: Geometry used for the interferometers, with corner reflectors shown. 52
Figure 3.19: Interferometer data from a rapid-shutdown with corrections from fringe skips. 53
Figure 3.20: Processed interferometer data including effective path lengths through the last closed flux surface (LCFS) found using JFIT [68] reconstructions. The LCFS is plotted from green to blue along the time interval shown. 54
Figure 3.21: Geometry of magnetic diagnostics and coarse current grid used by JFIT. Flux loops are shown as blue circles, Mirnov coil magnetic probes are shown as red arrows in the direction of probe orientation, and the external Rogowski coil encloses the vacuum vessel shown in grey. 60

Figure 4.1: Overview data of typical observations during the thermal quench, current quench and runaway plateau phases including a) total measured plasma region current I_p, wall current I_w, inductive decay model current $I_{L/R}$, and plateau phase runaway current I_r, b) runaway energy measured with scintillators, visible synchrotron emission [83], and a theoretical maximum, c) hard x-ray emission measured by a mid-plane detector at 90 degrees toroidal, and d) the edge safety factor calculated [40] by JFIT. An expansion of the thermal quench is shown to detail fast response of the following: e) broadband cyclotron emission, f) soft x-ray emission with inner and outer divertor strike points labeled (ISP and OSP respectively), g) visible line radiation from the pellet and hard x-ray emission, and signals on a neutron counting plastic scintillator. Temporal phases including the thermal quench and current quench are indicated along the top of each section. 66

Figure 4.2: Correlation of times recorded for prompt hard x-ray bursts in detectors on the bottom of the machine and soft x-ray bursts in chords viewing the outer strike point. The inlay shows hard x-ray (HXR) and soft x-ray (SXR) time traces during prompt loss for one example shot. 69

Figure 4.3: Total line averaged density shown with both broadband and channelized ECE systems for a-c) diverted and d-f) limited configurations. 71

Figure 4.4: a) A histogram illustrating that the average intensity of the time integrated prompt loss hard x-ray burst is greater in diverted experiments compared to limited experiments. An inlay shows the respective time histories of I) current and II) hard x-ray emission in lower detectors in two example discharges. Also shown are b) the time integrated prompt bursts plotted against the RE plateau current magnitude. 72

Figure 4.5: Spatial hard x-ray emission profiles with detector locations circled and JFIT magnetic reconstructions of last closed flux surface location and shape. Panels are shown for the prompt loss phase (a), the steady and bursty emission during the plateau phase (b & c), and the kink-like termination phase with apparent toroidal mode numbers labeled (d & e). Amplifiers are saturated at 10V. 74

Figure 4.6: Plasma motion in a shot where a) RE current was moved off of the limiter, showing b) hard x-ray emission. The current centroid major radius R_c is shown with the gap size between the LCFS and limiter in (c). In the cross-section plots, the current centroid is marked by an 'X'. The blue circle in the bottom right panel marks the location of peak limiter activation. 76
Figure 4.7: Signals on differential magnetic probes which occur coincident with hard x-ray bursts at different phases. Expanded views of the I) prompt loss phase, II) plateau phase, and III) final termination phase are also shown. 77
Figure 4.8: a) Total measured current, b) hard x-ray signals on midplane scintillators at three toroidal locations, c) the toroidal peaking factor for these scintillators, and d) a histogram of the plateau phase toroidal peaking factor for all plateaus. 79
Figure 4.9: Final termination mode for RE plateaus. 81
Figure 4.10: Integrated final hard x-ray bursts in lower detectors plotted against final measured RE current for terminations at the top of the vessel, as discussed in the text. 82
Figure 4.11: Midplane toroidal array of hard x-ray scintillators showing a consistent final loss sequence of toroidal asymmetry, with detector toroidal locations marked in degrees. 83
Figure 4.12: A histogram of a) the toroidal peaking factor (TPF) averaged during late loss hard x-ray emission, b) the phase of the peak, c) the duration of final loss, and d) the integrated intensity of final loss. 85
Figure 4.13: Experimental shapes with Poincaré plots generated by NIMROD showing closed surfaces (red and blue) and stochastic field regions (black) at the peak of stochasticity during a disruption. Green X's on the limiting boundary mark strike points for RE de-confined through stochastic regions. 86
Figure 4.14: A comparison of electron stopping powers (ie drag forces $F_d = dW/dz$) normalized by mass density for carbon and argon as tabulated in the NIST ESTAR database [15]. 89

Figure 5.1: Layout of diagnostics and experimental hardware used in pellet injection experiments studying runaways, with a) a top down midplane cross-section, and b) a poloidal cross-section. Note that not all diagnostics lie in the same poloidal plane. 94

Figure 5.2: Data observed during the experiment including a) plasma current I_p, fit to L/R current decay time, I_{LR}, subtraction of the two for runaway current I_r, b) density, c) soft x-ray data shown by chord number (see fig 3.3), d) a poloidal array of three hard x-ray scintillators [79], e) cyclotron emission power spectrum, and f) a portion of the visible emission spectrum. 95
Figure 5.3: Measurements of plasma current, line integrated electron density, neutral pressure at the wall, reflectometer measured electron density profile, and the maximum radius of the last closed flux surface. 97
Figure 5.4: On the left, a) a visible camera frame mapped into the poloidal R,Z plane from just before injecting the first pellet. The last closed flux surface, pellet trajectory, and pellet explosion location are marked in red. On the right, b) a sequence of three images for the first pellet injected, with the pellet trajectory in red, and the LCFS in the poloidal plane of pellet injection in red in the foreground, and the background LCFS marked at various toroidal locations in blue. The view spans a curving plasma geometry which is mapped to the R,z plane with the tangency points between magnetic field lines and pixel lines of sight, accurate to a few millimeters. 98
Figure 5.5: a) Cyclotron emission bursts featuring a fast and slow component, and b) a zoom on the fast component in arbitrary log scale, with possible frequency drift annotated. 100
Figure 5.6: Energy deposition simulation using EGSnrc for a pencil beam of 20MeV RE impacting various materials from the left at $r = 0$, $z = 0$. 103

Figure 6.1: Time histories of various quantities of relevance during a disruption calculated with the KPRAD code, and runaway production corresponding to the generation mechanisms described by equations 2.4, 2.7, and 2.8. 109
Figure 6.2: A view from the top of the torus showing toroidal spacing between the bolometer view and killer pellet injection locations, and poloidal views showing the emission region covered by the numbered bolometer chords and the flux function grid used for tomographic inversion. 111
Figure 6.3: Tomographic inversion of an argon killer pellet shutdown at various times. Overview time histories are also shown of the data as prepared for inversion and the data reconstructed after the inversion, both of which look similar. 112

Figure 6.4: The flux function, poloidal magnetic field, and current density inferred using the codes JFIT and EFIT at a time just before a killer pellet shutdown. 119
Figure 6.5: Results from analysis of loop voltages during a shutdown using the codes JFIT and EFIT. a) Electron temperature and b) total current are shown for timing reference, along with the c) apparent inductance and (d, e and lower panels) the apparent voltages inferred from either code using several techniques. Quantities inferred from EFIT are lightened where convergence failed. . . . 121
Figure 6.6: Voltages measured directly on flux loops located on the a) outboard and b) inboard sides of the vacuum vessel near the midplane, with c) broadband ECE shown for a TQ timing reference and d) plasma current shown for a CQ timing reference. 122
Figure 6.7: Fitting quality and convergence results from EFIT showing error increasing after $2ms$ after a shutdown. 123

Figure C.1: A diagram of the impurity pellet injector vacuum system. . . . 137
Figure C.2: A sketch of the pellet jamming condition and modifications made to eliminate jamming. 138
Figure C.3: New parts installed on the pellet injector including a) larger diameter bore pellet catchers and b) an alignment jig. 139
Figure C.4: Timing histograms for $d = 2mm$ polystyrene pellets fired along the curved guide tube in a mockup test. 141

Figure D.1: Runaway electron current I_r calculated by subtracting three different models for thermal current I_t from total measured current I_m, with the density used to calculate the avalanche rate, and the effective time dependent rates for each of the three models. Vessel current I_v is also shown for comparison with the following model. 145
Figure D.2: Current and magnetic energy histories for the avalanche model. An exponential fit to the CQ and the subtraction of this fit from total measured current are shown dashed for comparison with modeled quantities. 147
Figure D.3: a) Integrated toroidal field plotted versus the final RE current, and b) initial seed RE current plotted from these versus final RE current. 149

LIST OF TABLES

Table 3.1: Primary diagnostics used in this thesis. 29

Table A.1: A listing of the numerous symbols used throughout this thesis. . 129

Table B.1: A non-exhaustive DIII-D shot history of runaway electron observation demonstrating the wide variety of experiments which can generate runaway electrons. 133

ACKNOWLEDGEMENTS

To:

George Tynan and Eric Hollmann my two advisors and mentors throughout graduate school for their unwavering support,

James Kulchar, Derek Sundstrom, Ron Ellis, and David Ayala in the DIII-D diagnostics lab for entertainment, assistance, and moral support,

Figure 0.1: The DIII-D Team

Gary Jackson for help with the DIII-D pellet injector,

the entire DIII-D team for countless hours of assistance and operating an excellent experiment,

Sergei Krasheninnikov for consultations and his preliminary service on the thesis committee,

Robert Parker and Kerry Key of Scripps Institution of Oceanography for their consultations regarding inverse problems,

Ryan Hill of Don Carlos Burritos and Chuck of Bird Rock Coffee Roasters for sustenance and community,

my friends who helped me get out when I needed to and listened to my wild ideas about flying motorcycles,

my girlfriend Deborah for her unmeasurable tolerance,

to all of these people, for all of these things, and for many others I surely have forgotten

thank you.

Chapters 3, 4, and 5 contain material from the following publications:

- A. N. James, E. M. Hollmann, and G. R. Tynan. "Spatially distributed scintillator arrays for diagnosing runaway electron transport and energy behavior in tokamaks", Rev. Sci. Instrum. 81, 10E306 (2010)

- A. N. James, E. M. Hollmann, J. H. Yu, M. E. Austin, N. Commaux, T. Evans, D. A. Humphreys, T. C. Jernigan, P. B. Parks, S. Putvinski, E. J. Strait, G. R. Tynan, and J. Wesley. "Pellet interaction with runaway electrons", J. Nuc. Mater., In press (2011)

- A. N. James, E. M. Hollmann, G. R. Tynan, M. E. Austin, N. Commaux, N. Eidietis, T. Evans, D. A. Humphreys, A. Hyatt, V. A. Izzo, T. C. Jernigan, R. J. La Haye, P. B. Parks, E. J. Strait, J. C. Wesley, and J. H. Yu. "Measurements of hard x-ray emission from runaway electrons in DIII-D", Nucl. Fus., to be submitted (2011)

The dissertation author was the primary investigator and author of these papers, and would like to acknowledge contributing support from the co-authors and the publishers.

VITA

January 10, 1983	Born, San Clemente, California
2005	Bachelor of Science, University of California, San Diego
2007	Master of Science, University of California, San Diego
2011	Doctor of Philosophy, University of California, San Diego

A full curriculum vitae and more information about the author can be found at `http://cer.ucsd.edu/~james/`

ABSTRACT OF THE DISSERTATION

Investigations of runaway electron generation, transport, and stability in the DIII-D tokamak

by

Alexander Nevil Tronchin-James

Doctor of Philosophy in Engineering Science (Engineering Physics)

University of California, San Diego, 2011

George Tynan, Chair

Energy production is a continuing problem in the modern world, and nuclear fusion in tokamak reactors may be a viable solution. One remaining problem for tokamaks is the generation of runaway electrons (RE) during shutdown of these reactors, the focus of this thesis. Energy and runaway electrons are both briefly reviewed, with emphasis on prior theses, prior theoretical developments, and prior experimental studies which establish context in the pre-existing body of knowledge.

New experimental techniques tailored for studying RE are described. These techniques include plasma shaping optimized for RE generation via argon killer-pellet shutdown, which increased the probability of RE plateau in a shutdown from 30% to over 80%.

A newly developed hard x-ray sensing scintillator array is described in detail, and this new diagnostic is used along with pre-existing diagnostics to explore the temporal and spatial character of hard x-ray emission resulting from RE. X-ray emission associated with RE impact at divertor strike points was observed after thermal quench (TQ) but before current quench (CQ). Instabilities of the RE current were observed during the plateau and at termination.

Experiments probing RE in-situ by injecting polystyrene diagnostic pellets are also discussed. Pellets were observed disintegrating before reaching the last closed flux surface (LCFS), suggesting that substantial RE transport beyond the LCFS occurs, which is consistent with observed activation of the low field side midplane limiters.

Inference of loop voltages during the pre-current quench (CQ) phase using inverse techniques and a discussion of limitations of this technique are also presented. Loop voltages exceeding $1kV$ are inferred peaking well before the beginning of CQ, and are capable of accelerating RE to energies of over $10MeV$ at the time of the first x-ray emission from RE impact with the wall. During the later CQ phase, this inferred voltage matches a simpler estimate for the loop voltage $-LdI/dt$.

Chapter 1

Introduction

The problem studied in this thesis is the phenomena of runaway electrons, and the damage that these electrons can cause to tokamaks: the machines proposed as a way to generate power via nuclear fusion. This chapter is written as a general introduction for non-expert readers to establish this work in the context of the greater problems around it. Chapter 2 serves as a brief review of prior work studying runaway electrons, and is separated into two main sections describing theoretical work and experimental work. Chapter 3 describes the experimental methods and the various diagnostic techniques used for studying runaway electrons during tokamak shutdowns, with emphasis on a hard x-ray diagnostic developed specifically to study runaway electrons. Primary results from this new hard x-ray diagnostic and relevant observations about runaway electrons are described in chapter 4. Experiments studying the interaction between small diagnostic pellets and pre-existing runaway electron current are discussed in chapter 5. Chapter 6 describes investigations into the earliest loop voltages which likely generate a small seed population of runaway electrons, which is subsequently amplified.

1.1 Energy in modern civilization

Since the dawn of modern civilization, mankind has used energy for heat, light, and increasingly complicated industrial and commercial activities which require an always increasing supply of energy. The sources of this energy have varied

over time as a result of mankind's always advancing technologies and awareness of resources.

Today, energy is provided primarily by burning fossil fuels such as coal, natural gas, and processed crude oil. However, harvesting and combusting these sources for energy generates undesirable pollution and greenhouse gases. The available supply of crude oil in the world is forecast using Hubbert peak theory [66], which predicts a rapid decline in the coming century. In addition, since large scale storage of oil is prohibitively difficult and expensive, the supply rate of oil is matched closely with demand, which requires large fluctuations in the price of oil to control demand, as predicted by queue theory [24]. Both this declining supply and the wildly fluctuating price of oil press the need for replacement energy sources.

A portion of our energy also comes from nuclear fission power stations, which split heavy atoms such as uranium for energy. While only roughly $1.5cm^3$ of high level radioactive waste is generated per person per year in the entire world [4] by nuclear fission reactors, processing of this waste is illegal in the US due to the risk of nuclear proliferation, and siting of a long term storage facility is difficult due to public perception. Despite the fact that much fewer deaths result from nuclear power compared with fossil fuels per terawatt-hour of energy generated (0.04 deaths/TWh vs. 201 deaths/TWh respectively [3], roughly a factor of one thousand), again public perception of the consequences of accidents at nuclear power plants limits their expanded use.

Alternative sources of energy such as solar photovoltaics, wind and water turbines, and geothermal heat are becoming increasingly attractive but they each suffer from limitations including location restrictions and intermittency which requires storage of energy for later use. While these sources may work for some applications, a more controllable source of energy with a larger fuel supply may be necessary for others, and one possible solution is power from nuclear fusion.

1.2 Nuclear Fusion

Fusion is a nuclear reaction where two atoms combine together to form heavier atoms, releasing energy in the process. Typically light atoms like hydrogen are used for fusion energy, but atoms as heavy as iron can release some energy during fusion. The repulsive Coulomb forces of the positively charged nuclei in hydrogen atoms prevent fusion from happening in most scenarios on Earth however. For fusion to occur, these repulsive forces must be overcome, which can be achieved most easily by increasing the temperature to roughly ten times that of a star (about ten million degrees Celsius) so that hydrogen atoms collide together hard enough on average to result in substantial fusion. Heating hydrogen to such high temperatures is not easy however, since most materials will vaporize at temperatures much lower than those of a star. To illustrate how fusion can occur, several types of reactors are described below.

1.2.1 Natural reactors

Nature's fusion reactor is the star: a giant sphere of mostly hydrogen in which pressure from its own gravity results in a temperature high enough to cause fusion, which then heats the star further, balancing the gravitational pressure and preventing collapse of the star. Thermal radiation produced by fusion in the sun is precisely the source of our solar power which heats the surface of the Earth, drives the water cycle, makes plants grow, and powers photovoltaic cells. The sun has produced energy reliably for an incredibly long time, but the rotation of the Earth, cloud cover, and other factors can make the delivery of solar power to Earth intermittent.

At the high temperatures found in stars, electrons separate from their atomic nuclei due to high-energy collisions, and the resulting mixture of free electrons and ionized nuclei is called a plasma: the fourth and most common state of visible matter in the universe. Plasma physics is the study of how these electrical charges behave differently from a neutral gas, and is introduced for curious readers in a book by Francis Chen [22]. The physics of plasmas in stars and other

astrophysical systems are described in more detail in a book by Russel Kulsrud [100]. While we can learn much and otherwise benefit greatly from the stars, there are many reasons for bringing these processes down to Earth where we can apply them for our own purposes, but unless the reactor is much larger than a star (ie a Dyson sphere) gravity cannot be used for confinement.

1.2.2 Manmade reactors

Attempts at designing fusion reactors smaller than stars have revealed a long list of challenges and problems to solve, so plasma confinement remains an active scientific research topic today. Towards the end of World War II, scientists from around the world on both sides of the war poured enormous effort into making the first atomic devices and they succeeded for the first time in achieving nuclear fusion shortly thereafter. Fortunately, since those first accomplishments and through hard political work (described briefly among other places in a book by Freeman Dyson [32]), peaceful applications of nuclear power have advanced substantially through ongoing efforts to achieve power from confined nuclear fusion. There are two primary techniques for confining a fusion reaction: inertially and magnetically.

1.2.2.1 Inertial confinement

In the scheme of inertial confinement, fuel is heated faster than it can blow itself apart, which John Lindl describes more thoroughly in his book [112]. This has been attempted using many techniques including wire array Z pinches and laser heating. Of these, laser heating has received the most attention so far, and the National Ignition Facility (NIF) at Lawrence Livermore National Laboratory is presently the largest facility in the world attempting to achieve fusion using lasers. If everything goes as planned, the NIF may achieve ignition of small fuel capsules within a year of this thesis.

1.2.2.2 Magnetic confinement

Magnetic fields have also been used to confine hot plasma, as described in an excellent book by R. D. Hazeltine and J. D. Meiss [57]. Among the many

types of devices used historically for magnetic confinement are: magnetic mirrors, stellarators, and the type focused on in this dissertation: tokamaks, illustrated in figure 1.1.

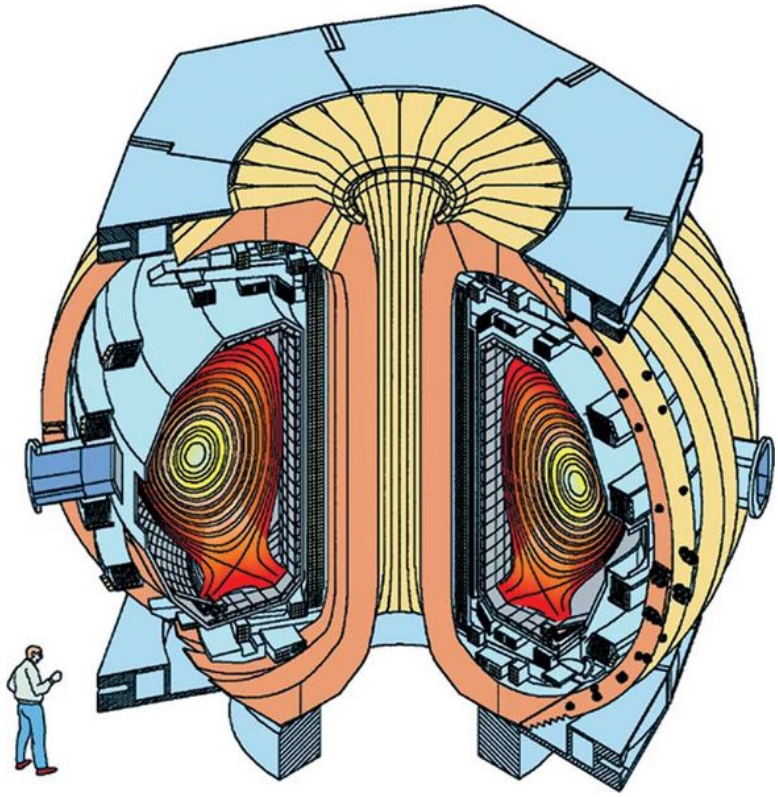

Figure 1.1: A cartoon of the DIII-D tokamak operated at General Atomics in San Diego.

Operating these devices at high performance requires an understanding of magnetohydrodynamics (MHD) and MHD stability, a topic discussed thoroughly in a seminal paper by J.P. Friedberg and his associated book [39, 40]. The quest for fusion power pushes the envelope of MHD stability limits in search of operating regimes which will achieve ignition: when the fusion power produced exceeds the power necessary to sustain a burning fusion reaction. The first magnetic confinement fusion machine designed to achieve ignition is called ITER [8], an international collaboration including: China, the European Union, India, Japan, Korea, Russia, and the United States of America, but while the site is selected and the design is well under way, a few outstanding problems remain for ITER. One of

those outstanding problems is called a disruption, a situation in which a plasma stability limit is accidentally crossed, which results in sudden and sometimes catastrophic deposition of the previously confined thermal and magnetic energy to the machine vessel and plasma facing components. The work in this dissertation was performed on the DIII-D tokamak hosted by General Atomics, a machine which fortunately has a low enough power density during disruptions that the machine can be safely and repeatedly disrupted to study disruption physics. Disruption mitigation techniques such as the injection of radiating impurities have been shown [62] to significantly decrease the potential for damage from thermal and mechanical loads. However, still another problem remains, investigation of which is the focus of this dissertation: runaway electrons.

1.3 Runaway electrons

Simply stated, runaway electrons are electrons moving so quickly that they undergo almost no drag forces, which allows them to accelerate to relativistic energies.

1.3.1 Basic theory of runaway generation

The essential phenomena of runaway electrons can be explored through a simple derivation. In a plasma, electrons and ions with charge $q_e = -e$, $q_i = Ze$ and density $n_e = Zn_i$, n_i respectively, undergo an accelerating force $F_E = qE$ from any electric field E present, which generates the current density j needed to stabilize a toroidal plasma according to Ohm's law

$$E = \eta j, \tag{1.1}$$

$$\eta = \frac{m_e \nu_{ei}}{n_i q^2} \tag{1.2}$$

where $\nu_{ei} = n_e \sigma_{ei} v_{Th,e} = \frac{n_i e^4 Z^2 ln\Lambda}{4\pi\epsilon_0^2 m_e^2 v^3}$ is the electron-ion collision frequency for electrons with thermal velocity $v_{Th,e} = \sqrt{T_e/m_e}$, and $ln\Lambda$ is the Coulomb logarithm. The Rutherford scattering cross-section σ_{ei} can be estimated from an energy prin-

ciple equating the electrostatic coulomb energy and the kinetic energy

$$q^2/r = mv^2/2 \rightarrow r = 2q^2/mv^2 \tag{1.3}$$

$$\sigma = \pi r^2 = 4\pi q^4/m^2v^4(ln\Lambda) \tag{1.4}$$

where the Coulomb logarithm is included to incorporate large angle collisions. This cross-section asymptotically approaches zero for large velocities, which is the essential cause of runaway phenomena. Combining this all back into the resistivity results in

$$\eta = \frac{4\pi q^2 ln\Lambda}{m_e n_i v^3} \tag{1.5}$$

which recovers the well known $\eta \propto T^{-3/2}$ result discovered by Spitzer [155]. The associated resistive drag force is

$$F_D = m_e v \nu_{ei} = n_i e^4 Z^2 ln\Lambda_{ei}/4\pi\epsilon_0^2 T_e \tag{1.6}$$

For low velocity particles (i.e. most particles in a thermal distribution), this drag balances the electric acceleration. For particles with large velocity, this resistive drag vanishes so the electric force is unbalanced and electrons accelerate and run-away: the primary generation mechanism.

Once a small population of electrons first run away, a secondary generation occurs due to rare large-sangle collisions between runaway and thermal electrons, which result in both electrons having velocities high enough to runaway and causes an avalanche-type evolution of the number of runaways. These effects, which will be elaborated on later in section 2, describe the basic process of runaway electron generation for various scenarios both in nature and in the laboratory.

1.3.2 Natural occurrence

In nature, runaway phenomena occur in lightning bolts and a variety of astrophysical situations, studies of which date at least back to 1925 [167]. Charge separation in a thundercloud results in buildup of an electric field between the top and bottom. One might expect that the breakdown potential for lightning in a thundercloud is close to the typical $16kV/cm$ potential measured in air, but

investigations have revealed a much lower breakdown potential [54, 55]. This occurs due to the above avalanche effect in which low-energy electrons are knocked into runaway by high-energy electrons, with the original high-energy electrons presumably generated by a cosmic ray or radioactive decay of an atmospheric atom. Such high-energy electrons can have a mean free path of a few kilometers over which they gain even more energy. In the atmosphere, these high-energy electrons have the distance necessary to accelerate and avalanche, but a laboratory discharge setup typically features two high voltage electrodes only a few centimeters apart, hence the apparent variation in the breakdown potential. Runaways generated in lightning bolts resulted in a temporary scare at nuclear monitoring sites around nuclear reactors in Japan, where they observed radiation bursts (now associated with runaways) during lightning storms [161].

Runaway is also observed in the outer radiation belt and at the Earth's magnetic bow shock. In these situations, the accelerating fields come instead from interactions between the Earth's magnetic field and the solar wind, such as reconnection of magnetic field lines [162] or from low-frequency radio waves [175]. Astrophysical systems are inherently a large enough scale for runaway to occur, again contrary to a typical laboratory experiment.

1.3.3 Laboratory occurrence

While electron runaway is not possible in the typical laboratory high-voltage breakdown experiment described above because of the small length scale compared with the runaway mean free path, some laboratory systems exist in which the length scale is large. Toroidal devices such as tokamaks are one such system, due to the magnetic topology of closed magnetic flux surfaces. In such a system, charged particles move along helically shaped magnetic field lines which have essentially infinite length since they wrap back onto themselves, so the effective path length approaches infinity. In tokamaks, the conditions for runaway generation can occur in a number of scenarios including:

- low-density startup, where the low density and higher than normal loop voltage enable runaway,

- lower hybrid and electron cyclotron current drive, in which large-amplitude microwave radiation accelerates runaways,
- sawtooth crashes, where magnetic reconnection may accelerate runaways similar to the above astrophysical example, and
- disruptions and rapid shutdowns, where loop voltages from rapid cooling and current decay sometimes accelerate runaways, resulting in damage to the machine.

Further understanding the last item is the focus of this dissertation since many questions remain about runaway behavior in this scenario, and the resulting damage may obstruct progress toward operation of a power-producing tokamak fusion reactor.

At the end of a disruption, the energy carried by runaways is rapidly deposited to the vessel. The kinetic energy $W_k = \gamma m_e c^2 I_r 2\pi R/ec \sim 500kJ$ and magnetic energy $W_m = L_r I_r^2/2 \sim 250kJ$ present different hazards due to the different timescales and mechanisms of deposition. Solutions to the problem of runaway generation remain elusive and are important for the success of future burning plasma devices, and chapter 2 presents a brief review of prior work studying runaway generation, transport, and stability in tokamak rapid shutdowns and disruptions.

1.4 Tokamak Disruptions

During a disruption the energy stored in a plasma is rapidly deposited to the vessel due to loss of confinement. The thermal energy $W_t = \int nkTdV \sim 1MJ$ and magnetic energy $W_m = L_p I_p^2/2 \sim 1MJ$ stored in the plasma are transferred to the vessel at different rates, and through different mechanisms, roughly analogous to the earlier mentioned runaway energy deposition.

1.4.1 Causative factors

Disruptions can occur as a result of several different causes. Generally, breaching some MHD stability threshold results in a mode increasing in amplitude enough that the hot plasma contacts and ablates impurities from the wall. Signatures of this mode growth before a disruption occurs are referred to as the precursor, which is sometimes observed on a variety of diagnostics for a period of several milliseconds.

Sometimes there is no apparent pre-cursor activity before a disruption. This variety of disruption can have numerous causes including: failure of plasma control system computers, power supplies, or feedback critical diagnostics; or even failure of the armor wall tiles causing them to fall into the hot plasma region.

The hot plasma can also be intentionally terminated by injecting some variety of radiating impurities, referred to as a rapid shutdown. Rapid shutdowns utilizing argon killer pellets are used in experiments described in this thesis to generate runaway electrons.

1.4.2 Thermal Quench

The thermal quench (TQ) results from convection of plasma thermal energy into the armor tiles and line radiation from assimilated impurities. Through thermal collisions, the hot plasma excites any assimilated impurities, which emit line radiation and rapidly cool the plasma, resulting in the TQ. This cooling period generally lasts for $\tau_{TQ} \sim 300\mu s$ and is accompanied by a rapid re-organization of plasma current through a sequence of MHD instabililties. During the thermal quench, rapid heating of the first wall and other plasma-facing components can result in melting, vaporization, cracking, and other damage associated with thermal loading. Rapid shutdown techniques significantly reduce these hazards due to uniformity of a radiative thermal quench which results in reduced thermal loads, however runaway electrons can remain confined and avalanche to a new problem. Runaways generated during the thermal quench phase which remain confined are referred to as seed runaways, since the runaway current grows later only if this seed is still present.

1.4.3 Current Quench

After the plasma current re-organization from the thermal quench completes, the plasma current begins to drop on an inductive timescale $\tau_{CQ} = L/R \sim 5ms$ to adjust to the decreased conductivity associated with the reduced temperature. During the current quench, mechanical forces from plasma current conducted into the wall and vacuum vessel, called halo currents, can result in mechanical damage to the wall structure. Halo current hazard is significantly reduced, however, by rapid shutdown techniques [68] and by keeping the decaying current vertically centered in the vessel.

If too few runaways remain confined for avalanche to occur, then the disruption ends at this phase after the current decays completely. When enough runaways remain for avalanche to occur, a loop voltage $V_{loop} = -d/dt(LI)$ induced by the decaying current drives runaway avalanche which increases the initially small runaway seed current, a concept built upon in section 2.1.1. Often the inductance is assumed to remain constant so the loop voltage simplifies to $V_{loop} = -LdI/dt$, however the full voltage is considered in chapter 6. Typical values for these quantities during the current quench are $L = 2\mu H$ and $dI/dt = -200kA/ms$, so that the loop voltage is about $-LdI/dt = 400V$, corresponding to an electric field at the machine axis $R = 1.67m$ of $E = V_{loop}/2\pi R \sim 40V/m$. Since runaway current has a large conductivity, the avalanche eventually shorts out this loop voltage after the current quench begins as runaway current increases and the loop voltage drops correspondingly.

1.4.4 Runaway plateau

During the runaway plateau, up to hundreds of kilo-Amperes of relativistic electrons carry current in the plasma. Generally runaway current gradually decreases or remains roughly constant during this phase, which can therefore last up to a few hundred milliseconds. Infrared camera studies of the first wall at JET show [7] a series of runaway impacts on the first wall which result in rapid heating and appear in roughly the same location shot to shot, suggesting that the deconfinement occurs due to some persistent parameter such as machine geometry.

Soft and hard x-ray emission occur during this phase due to collisions between runaways and plasma and neutral impurities and due to gradual diffusion of runaways across magnetic flux surfaces to impact the first wall, both discussed more thoroughly in section 2.1.3.

1.4.5 Runaway termination

After some duration the runaway plateau terminates abruptly, resulting in final termination of any remaining current. During this termination, large magnitude x-ray emission occurs corresponding to bremsstrahlung from runaway impact on solid first wall materials. All of these processes are described more fully in the following chapters.

Chapter 2

A brief history of runaway electron studies

To establish context and motivation for the studies described in this thesis, this chapter recounts almost one hundred years of theoretical and experimental investigations of runaway electron physics, which chapters 4, 5, and 6 later build upon. No less than eight, and likely many more, PhD and Master's theses have been written on runaway electron studies in the past, and countless journal articles have been published describing progress on runaway electron physics. Still, many questions remain unresolved, and those which will be addressed in this thesis will be highlighted in these following sections. The chapter is separated into two summary divisions of runaway electron studies: theoretical studies, and experimental studies.

2.1 Theory

The theories of RE generation, energy limit and energy distribution, transport, equilibrium, and stability are recounted in this section.

2.1.1 Generation

The following sections discuss selections from prior efforts to understand runaway generation.

2.1.1.1 Dreicer generation

Harry Dreicer wrote a PhD thesis at Massachusets Institute of Technology in 1955 [29] titled "The extension of the kinetic theory of ionized gases to include Coulomb interaction, elastic, and inelastic collisions with molecules", where foundational work on the critical field for runaway electron generation was originally written. Dreicer's generation mechanism describes how electron runaway can occur in a plasma with a thermal distribution of electron and ion velocities in the presence of a strong electric field. This primary runaway generation mechanism is derived by setting the electric and drag forces (introduced in section 1.3.1) equal: $m_e \nu v = eE$, where $\nu = n_e e^4 ln\Lambda / 4\pi\varepsilon_0^2 m_e$, assuming a thermal electron distribution, and solving for the electric field, which recovers the minimum field necessary for runaway originally discovered by Dreicer [30, 31], and later reformulated [129] as

$$\begin{aligned} E_D &= \frac{e^3 ln\Lambda}{4\pi\varepsilon_0^2}\frac{n_e}{T_e} \\ &= 26kV/m\frac{ln\Lambda}{10}\frac{10eV}{T_e}\frac{n_e}{10^{15}cm^{-3}} \end{aligned} \tag{2.1}$$

This quantity differs from a later expression [43] for general charge states Z_{eff} also including relativity by a factor $1 + (Z_{eff} + 1)/\gamma$.

To find the critical energy above which particles will run away given a certain field in Dreicer's theory, again set the forces equal but now solve for the energy normalized to temperature:

$$\begin{aligned} eE = mv\nu = eE_D &= \frac{e^4 ln\Lambda}{4\pi\varepsilon_0^2}\frac{n_e}{T_e}, \\ \frac{W_D}{T_e} = \frac{E_D}{E} &\equiv \frac{1}{\epsilon_D}, \\ W_D &= 26keV\frac{ln\Lambda}{10}\frac{1V/m}{E}\frac{n_e}{10^{14}cm^{-3}} \end{aligned} \tag{2.2}$$

The fraction of electrons beyond this critical energy which can immediately runaway once the electric field is applied is the complementary error function of the ratio W_D/T_e, essentially zero in almost all cases:

$$\begin{aligned} \frac{n_r}{n_e} &= \int_{W_D}^{\infty} f_e(W)dW = \mathrm{erfc}(W_D/T_e) \\ &= \mathrm{erfc}(26) \sim 3 \times 10^{-297} \end{aligned} \tag{2.3}$$

In any thermal distribution of electron velocities, particles gradually diffuse across the W_D boundary due to random collisions with each other, resulting in a growth of the number of runaways at a rate [87]

$$\gamma_D = \frac{1}{n_e}\frac{dn_r}{dt} = A(Z_{eff})\epsilon_D^{-(Z_{eff}+1)3/16}\nu_{ee}e^{-1/4\epsilon_D-\sqrt{(Z_{eff}+1)/\epsilon_D}} \tag{2.4}$$

where $A(Z_{eff}) \sim 0.4$ is roughly constant, Z_{eff} is the effective charge state, the electron-electron collision frequency is [87]

$$\begin{aligned}\nu_{ee} &= \frac{e^4}{4\pi\varepsilon_0^2}\frac{n_e}{m_e^2 v_t^3} ln\Lambda \\ &= 6.65kHz\frac{n_e}{10^{13}cm^{-3}}\left(\frac{3keV}{kT}\right)^{3/2}\frac{ln\Lambda}{10}\end{aligned} \tag{2.5}$$

and the Coulomb logarithm is [138] [1]

$$\begin{aligned}\ln\Lambda_{ee} = \;& 23 - log\left(\sqrt{n_{e,cm^{-3}}}T_{e,eV}^{-3/2}\right) && T_e < 10eV \\ & 24 - log\left(\sqrt{n_{e,cm^{-3}}}T_{e,eV}^{-1}\right) && T_e \geq 10eV\end{aligned} \tag{2.6}$$

This runaway growth rate γ_D becomes large when the electric field becomes large compared to Dreicer's field. Using simple analysis of the electric field and associated loop voltage during a rapid shutdown, the electric field was previously inferred to be roughly $E_\phi \sim 40V/m$, which is small compared to the above estimate of the post-TQ Dreicer field. Chapter 6 will explore this electric field further, demonstrating that it may be much closer to the Dreicer field for a brief period.

2.1.1.2 Hot-tail generation

Runaway generation is also predicted to occur as a result of fast particles being stranded at large energies when cooling occurs faster than the collision time for those fast particles. In disruptions, high-Z impurities often cool the particle

[1] For later reference, the Coulomb logarithms for pre- and post-disruption quantities respectively are

$$\begin{aligned}ln\Lambda_{ee}(n_e = 10^{13}cm^{-3}, T_e = 3\times10^3 eV) = 17 \\ ln\Lambda_{ee}(n_e = 5\times10^{14}cm^{-3}, T_e = 1.5eV) = 6.7\end{aligned}$$

however, a value of 10 is often assumed for brevity.

distribution at a rate faster than or comparable to the time between collisions for high energy particles, generally $\lesssim 100\mu s$. This situation results in the high energy portion of the distribution remaining as a warm tail [23] while the rest of the distribution cools, so that the critical velocity falls past some of the high energy electrons before they slow, hence they runaway. From this mechanism, the runaway growth rate is [152]

$$\gamma_H = \frac{1}{n_e}\frac{dn_r}{dt} = \frac{1}{n_e}\frac{d}{dt}\int_{v_D}^{\infty} f(v,t)(v^2 - v_D^2)4\pi dv \tag{2.7}$$

where $f(v,t)$ is the distribution of speeds. Due to the inherently non-thermal nature of this rapid cooling, the distribution function is likely to be non-Maxwellian and strongly varying in space during TQ. Since the precise spatially dependent electron distribution function during TQ is not experimentally known, numerical analysis such as Fokker-Planck techniques must be used. This mechanism is not considered in depth in this thesis due to experimental uncertainty about the distribution of electron speeds during shutdowns, but the mechanism has been modeled elsewhere [151].

2.1.1.3 Avalanche generation

A secondary process of avalanche type runaway generation was first suggested by Sokolov [154], and is associated with large angle electron-electron scattering described originally by Møller [120, 121]. While the Coulomb scattering cross-section nearly vanishes for relativistic electrons, the Møller scattering cross section remains finite and results in rare large angle scattering from which both the incident and the target electron depart with sufficient energy to run away. This produces an avalanche type effect in the number, and hence current, of runaway electrons which results in further growth of the number of runaways at a rate [145]

$$\gamma_A = \frac{1}{n_r}\frac{dn_r}{dt} = \frac{1}{2\tau_A ln\Lambda_{ee}}(\frac{E}{E_A} - 1), \tag{2.8}$$

where

$$\begin{aligned} E_A &= \frac{e^3 ln\Lambda}{4\pi\varepsilon_0^2}\frac{n_{e\star}}{m_e c^2} \\ &= 0.051 V/m \frac{ln\Lambda}{10}\frac{n_{e\star}}{10^{14} cm^{-3}} \end{aligned} \tag{2.9}$$

is the critical field necessary for avalanching [87], $\tau_A = m_e c/eE_A$, and $n_{e\star} = 2n_{e,free} + n_{e,bound}$ is the sum of twice the free electron density and the bound electron density as prescribed by [145, 61, 107]. [2]

Conversely, this equation describes the density, often attributed to Rosenbluth [145], above which collisional suppression of avalanche occurs

$$\begin{aligned} n_{Rosenbluth} &= \frac{E m_e c^2 4\pi\varepsilon_0^2}{e^3 ln\Lambda_{ee}} \\ &= 2\times 10^{17} cm^{-3} \frac{E}{100V/m} \frac{10}{ln\Lambda_{ee}}. \end{aligned} \tag{2.10}$$

This density, calculated for a typical electric field during a CQ, is orders of magnitude above the plasma density even after mitigation techniques such as injecting large quantities of gas or cryogenically frozen noble gas, so other techniques are necessary to suppress runaway generation during a CQ.

2.1.2 Energy limit and energy distribution

Once runaways are generated, they continue to gain energy as they fall down any electric potential present, but there is an upper limit to their energy due to synchrotron radiation which results in an effective drag force. At least one study has linked the plateau phase runaway current decay to synchrotron drag [6]. The synchrotron drag force is [9]

$$F_{syn} = \frac{2}{3} r_e m_e c^2 \beta^3 \gamma^4 \frac{1}{\langle R\rangle^2}, \tag{2.11}$$

where the gyro-averaged radius of curvature is determined by

$$\frac{1}{\langle R\rangle^2} \simeq \frac{1}{R_0^2} + \frac{sin^4\theta}{r_g^2}, \tag{2.12}$$

[2] The factor of two difference between free and bound electrons is not explained in any of the above references, so is here briefly discussed. This factor results from the Coulomb logarithm $ln\Lambda = ln(b_{max}/b_{min})$, the logarithm of the ratio between the maximum effective collision length b_{max} and the minimum effective collision length b_{min}. Collision lengths below are calculated for $W_k = 10MeV$ runaways in a post-TQ plasma with parameters: $T_e = 10eV$, $n_e = 10^{15} cm^{-3}$, $Z = 8$. For free electrons, the maximum length b_{max} is typically associated with the Debye length $\lambda_D e = \sqrt{\varepsilon_0 T_e/n_e e^2} \sim 740nm$, while for bound electrons it is instead associated with Bohr's atomic radius $a_0 = 4\pi\varepsilon_0\hbar^2/m_e e^2 \sim 53pm$. The minimum effective length b_{min} is the same for free and bound electrons: whichever is larger of the de Broglie wavelength $\lambda_B = ch/W_k \sim 1.2\times 10^{-13} m$ or the Landau length $b_0 = Ze^2/4\pi\varepsilon_0 W_k = 1.2\times 10^{-15} m$. The resulting Coulomb logarithms are then $ln\Lambda_{free} = 15.6$ and $ln\Lambda_{bound} = 6.09$, which differ by roughly a factor of two.

with R_0 the tokamak major radius, θ the electron pitch angle, $r_g = p_\perp/eB$ the relativistic gyro-radius, $r_e = \hbar\alpha/m_e c$ the classical electron radius, and the typical relativistic parameters $\gamma = W_r/mc^2 = 1/\sqrt{(1-\beta^2)}$ and $\beta = v/c = \sqrt{(1-1/\gamma^2)}$. The runaway energy limit is found by setting this force equal to the electric force, taking the limit $\beta \to 1$ and solving for the energy

$$\begin{aligned} W_{r,max} &= m_e c^2 \left(\frac{eE\langle R \rangle^2}{\frac{2}{3} r_e m_e c^2} \right)^{1/4} \\ &= 211 MeV \left(\frac{E}{10V/m} \right)^{1/4} \left(\frac{\langle R \rangle}{1.67m} \right)^{1/2} \end{aligned} \tag{2.13}$$

Neglecting drag and assuming unvarying electric field, the time it takes for runaways to achieve this energy is

$$\begin{aligned} t &= W_{r,max}/eEc \\ &= 70ms \sqrt{\frac{E}{10V/m} \frac{\langle R \rangle}{1.67m}} \end{aligned} \tag{2.14}$$

Generally, calculation of a runaway electron energy distribution requires invoking the time history of the electric field, density, temperature, and effective charge state in a Fokker–Planck treatment. With the simplifying assumptions that the plasma quantities and the applied field do not vary in time, and neglecting any drag forces, Jayakumar obtained [87] a simple expression from the energy differential Møller scattering cross section for secondary runaways [121, 86]

$$\frac{d\sigma}{dW_s} = \frac{Z_f^2 e^4}{8\pi\varepsilon_0^2 m_e v_f^2 W_s^2} \tag{2.15}$$

for the energy distribution expected for an avalanche dominated runaway population:

$$\frac{1}{n_r}\frac{dn_r}{dW_r} \sim \frac{1}{W_r} e^{-W_r/\delta W_r} \tag{2.16}$$

where δW_r is the characteristic width of the runaway energy distribution.

Runaway energy distributions similar to this expression have been observed at TEXTOR using a set of scintillators inserted into the runaway current [99, 97]. Including a synchrotron radiation imposed energy limit would result in electrons

piling up at this limit, hence producing a distribution peaked at both the high and the low energy ends. Kinetic modelling using Fokker-Planck techniques is typically used for this type of study, and at least two PhD theses have been been founded on such work. Fredrik Andersson wrote a PhD thesis [5] at Chalmers University of Technology in 2003 titled 'Runaway electrons in tokamak plasmas', which focused primarily on Fokker-Planck and Monte-Carlo numerical studies of runaway generation and transport. Another thesis written by Tamás Fehér [37] at Chalmers University of Technology in 2011 titled 'Simulation of runaway electron generation during plasma shutdown by impurity injection' used similar techniques to study runaway generation and transport in killer pellet shutdowns.

2.1.3 Transport, equilibrium, and stability

The physics of runaway transport, equilibrium, and stability are of particular interest since they govern when and where runaway impact occurs on various components. When runaway current settles into a stable controllable equilibrium, the possibility exists of gradually dissipating runaway energy by applying reverse voltages or through bremsstrahlung from scattering with injected impurities. However just as in ideal MHD, a stable equilibrium is subject to various criteria, the breaching of which can destabilize the equilibrium and result in damage to sensitive machine surfaces due to uncontrolled deposition of runaway energy. Since these concepts are invoked later in this dissertation, the principles are presented below.

2.1.3.1 Diffusion

A study of electron heat transport [143] in regions with a radial component of stochasticity δB_r in the magnetic field B revealed a corresponding diffusion coefficient $D_{RR} = \pi q v_{\parallel} R(\delta B_r/B)^2$. A later study and corresponding PhD dissertation [60, 5] investigated this result in tokamaks, finding that runaway avalanche should

be suppressed by sufficiently large magnetic perturbations

$$\frac{\delta B}{B} \gtrsim= \frac{a}{2.4}\sqrt{\frac{E_\parallel/E_{av}-1}{\pi qcR\tau p_{crit}/m_e c} ln\left(\frac{I}{NI_A ln\Lambda}\right)} \tag{2.17}$$

for major and minor radius R and a, parallel electric field $E_\parallel$, safety factor q, relativistic electron collision time

$$\begin{aligned}\tau &= 4\pi\varepsilon_0^2 m_e^2 c^3/n_e e^4 \\ &= .33s\frac{10^{14}cm^{-3}}{n_e},\end{aligned} \tag{2.18}$$

critical momentum $p_{crit} > m_e c$ corresponding to the momentum at which the runaway orbit width becomes comparable to the mode width of the magnetic turbulence, the tolerable number of avalanche folding times $N \sim 1$, and the Alfvén current $I_A = 4\pi m_e c/\mu_0 e = 17kA$. For DIII-D geometry and typical post-disruption parameters: $n_e = 10^{14}cm^{-3}$, $E_\parallel = 10V/m$, a estimate for this quantity works out to $\frac{\delta B}{B} \sim .0002$ for assumed $q = 1$ and $p_{crit}/m_e c = 1$, an order of magnitude smaller than calculated in the reference $\frac{\delta B}{B} \geq .003$.

When considering this mechanism for suppressing runaway generation however, one must recall the importance that this stochasticity exist everywhere runaways exist, otherwise runaways may remain confined to avalanche. For example: with runaways in the core, a resonant magnetic perturbation (RMP) cannot deconfine runaways if it doesn't penetrate beyond the plasma edge. For another example, runaways in islands which do not overlap with others during a disruption can result in runaway snakes such as those observed in TEXTOR [84].

Runaway transport is explored further in chapter 4 using x-ray emission from RE impact with vessel surfaces, and also in chapter 5 using small diagnostic probe pellets.

2.1.3.2 Force equilibrium

During typical tokamak operation from the perspective of ideal MHD, two forces generally balance each other to establish an equilibrium: the plasma thermal pressure gradient ∇p and the magnetic force on plasma current $j \times B$ [164]:

$$j \times B - \nabla p = 0 \tag{2.19}$$

The resulting equilibrium field is represented by a flux function ψ which is determined by the Grad-Shafranov equation [149]

$$\begin{aligned} -L\psi &= -R\frac{d}{dR}\frac{1}{R}\frac{d\psi}{dR} - \frac{d^2\psi}{dz^2} \\ &= \mu_0 R^2 p'(\psi) + \mu_0^2 f(\psi) f'(\psi) \end{aligned} \tag{2.20}$$

where the prime indicates a derivative with respect to ψ, and $f(\psi)$ is the poloidal flux function. This equilibrium fails, resulting in a disruption, when certain criteria for stability are breached, represented as gradient limits for the current, density, and pressure.

This classic result was later extended to include a relativistic beam (i.e. a runaway current) in a runaway plasma system by adding the runaway inertial pressure $F_r = -n_r(v_r \cdot \nabla)\gamma m_e v_r$ to the equilibrium force balance [170], in a continuation of earlier relativistic equilibrium studies [56, 122]

$$j \times B - \nabla p - F_r = 0. \tag{2.21}$$

The resulting equilibrium field is again represented by a flux function ψ, now determined by the modified Grad-Shafranov equation

$$-L\psi = \mu_0 R^2 p'(\psi) + I(\psi) \cdot I_p' + \mu_0 R(j_r + j_v), \tag{2.22}$$

where $I(\psi) = I_p + I_r + I_v$ is the poloidal current times $\mu_0/2\pi$ and the subscripts represent contributions from the plasma, runaways, and external coils respectively.

Since this equilibrium differs from the conventional Grad-Shafranov equilibrium, stability criteria of a high-energy runaway plasma therefore will likely also differ. A thorough analysis of the Yoshida equilibrium stability criteria may help to identify the currently unidentified instabilites observed in chapter 4 during the plateau and termination phases of a shutdown, however such analysis is beyond the scope of this thesis.

2.2 Prior Experiments

As stated previously, runaway phenomena have occurred in the cosmos and lightning since antiquity. One of the earliest studies of charged particle acceleration

in thunder-clouds dates back to 1925 [167]. More recently, Nicolai Lehtinen wrote a PhD thesis [109] at Stanford University in 2000 titled "Relativistic runaway electrons above thunderstorms", describing observations of 'red sprites', terrestrial γ-ray flashes, and other phenomena associated with runaway above thunderstorms, and also associated theoretical development including Monte-Carlo modeling. While the 'red-sprites' are claimed to result from atmospheric heating due to runaways, they resemble synchrotrom emission from tokamak runaways in color. Gammay ray flashes observed from lightning likely result from scattering of runaways with the atmosphere.

Since the 1950's, experiments worldwide have studied runaway phenomena in the laboratory and now represent a rich history. One of the earliest experiments studying runaways in the context of particle accelerators was called a plasma betatron [144, 150], an early toroidal pulsed power device developed at CERN of striking resemblance to the modern tokamak. The betatron used a helicon type plasma source wrapped around a section of the toroidal vessel, and a series of solenoid type windings which were pulsed by a capacitor bank to generate the accelerating electric field necessary for runaway generation. Since these early experiments studying runaways many more have followed, each steadily advancing our state of knowledge regarding runaway physics and observations.

The Priceton Large Torus (PLT) produced much of the early work on runaway transport and drift orbit displacement [12, 177]. Another tokamak at Princeton, the Tokamak Fusion Test Reactor (TFTR), saw some of the first serious damage due to runaway generation [82, 81], and some scientists from that project remain the strongest proponents of runaway electron research today [169]. Runaway electron currents in the range of several hundred kiloamps sometimes occurred in TFTR during disruptions. Chris Barnes wrote a PhD thesis [12] at Princeton University in 1981 titled 'Studies of runaway electron transport in PLT and PDX', studying the energy deposition of runaways on the limiters in those machines, which is similar to analysis in chapters 4 and 5.

At Oak Ridge National Laboratory in Tennessee, runaway electrons were studied in the Oak Ridge Tokamak (ORMAK). Stewart Zweben wrote a PhD thesis

[176] at Cornell University in 1978 titled 'An Investigation of High Energy Runaway Electron Confinement in the Oak Ridge Tokamak', studying the transport of runaways resulting from sawtooth oscillations and other MHD.

A German Tokamak Experiment for Technology Oriented Research (TEXTOR) conducted some developmental work on infrared imaging of runaway synchrotron emission and energy deposition [85, 34, 107], and more recently has advanced the state of runaway diagnosis from x-ray emissions [98, 99]. Scientists at TEXTOR have also studied runaway suppression using resonant magnetic perturbations [108] and runaway confinement in magnetic islands [84]. Roger Jaspers wrote a PhD thesis [85] at Eindhoven University of Technology in 1995 titled 'Relativistic runaway electrons in tokamak plasmas', about experimental studies from the TEXTOR tokamak studying runaway synchrotron emission, transport, and pitch angle scattering. Timur Kudyakov more recently wrote a PhD thesis [98] at Heinrich Heine University of Dusseldorf in 2009 titled 'Spectral measurements of runaway electrons in the TEXTOR tokamak', which describes development of a scintillator probe used to study the spatial distribution, energy spectrum, and transport of runaways. At TEXTOR, runaway electron currents in the range of several hundred kiloamps are generated during rapid shutdowns and disruptions.

Another German tokamak called ASDEX conducted early studies primarily on runaways generated during plasma startup [44] and focused on RE confinement [102]. More recent work from ASDEX has experimentally explored halo currents, disruption prediction, and also gas injection [136, 137].

The French machine Tore-Supra has also experienced damage from runaways which pierced cooling lines in their limiter [126, 113], and has developed runaway position control, and has attempted suppression using impurity injection [146] and has applied loop voltages to runaway current. Still, Tore-supra generates runaway electron currents in the range of several hundred kiloamps, so these mitigation techniques have only had limited success suppressing runaway generation.

In Japan, the tokamak JT-60U conducted experiments studying the conditions for runaway generation [172], injecting cryogenic neon pellets into a developed runaway current [90], and also studying the conditions for runaway current termi-

nation [159]. Scientists at this tokamak also conducted studies of high-Z mixed gas shutdowns using mixtures of hydrogen with argon, krypton, and xenon [11]. At JT-60U runaway electron currents in the range of several hundred kiloamps can occur during rapid shutdowns and disruptions.

In China, the EAST tokamak conducted experiments which resulted in RE generation, as recorded by a vertical array of collimated and externally mounted NaI scintillators [115].

In India, the SINP tokamak has conducted experiments on RE generation during plasma startup [70] to study diffusion [125].

The Joint European Torus (JET) in England has conducted excellent studies of soft and hard x-ray emission during disruptions [139, 48, 49], and also infrared imaging of runaway impact with divertor surfaces [107]. Shutdowns and disruptions at JET can generate runaway plateau currents in the range of $1MA$, one of the highest in the world currently.

At the Massachusetts Institute of Technology's Alcator C-mod tokamak, runaways can be generated using lower hybrid current drive, but are all lost during the thermal quench of disruptions [51] so that no runaway avalanche or plateau occurs. Rapid shutdowns at C-mod are possible using gas injection, but killer pellet shutdowns were not possible at C-mod as of the writing of this thesis.

The DIII-D tokamak, depicted in figure 2.1, is uniquely capable of studying runaway electrons due to the flexibility in shape and other operating parameters enabled by its design [116]. Disruption experiments date back to before 1996 [92], and have since been a vigorous focus of the DIII-D program [63]. Several generations of disruption mitigation experiments have occurred at DIII-D, including a variety of massive gas injection (MGI) valves and gas species [62], some of the earliest work on argon killer pellet injection [35], and most recently large shattered cryogenic pellets and thin shell pellets surrounding a shutdown payload [26]. Most of these techniques generate either no or few runaways, however argon killer pellets have been shown to generate the largest amount of runaways [63]. In addition, DIII-D has been fortunate that no significant damage from runaway impact on wall surfaces has occurred, likely due to the thick graphite wall tiles [13], which

has enabled continuing experiments to study runaway phenomena.

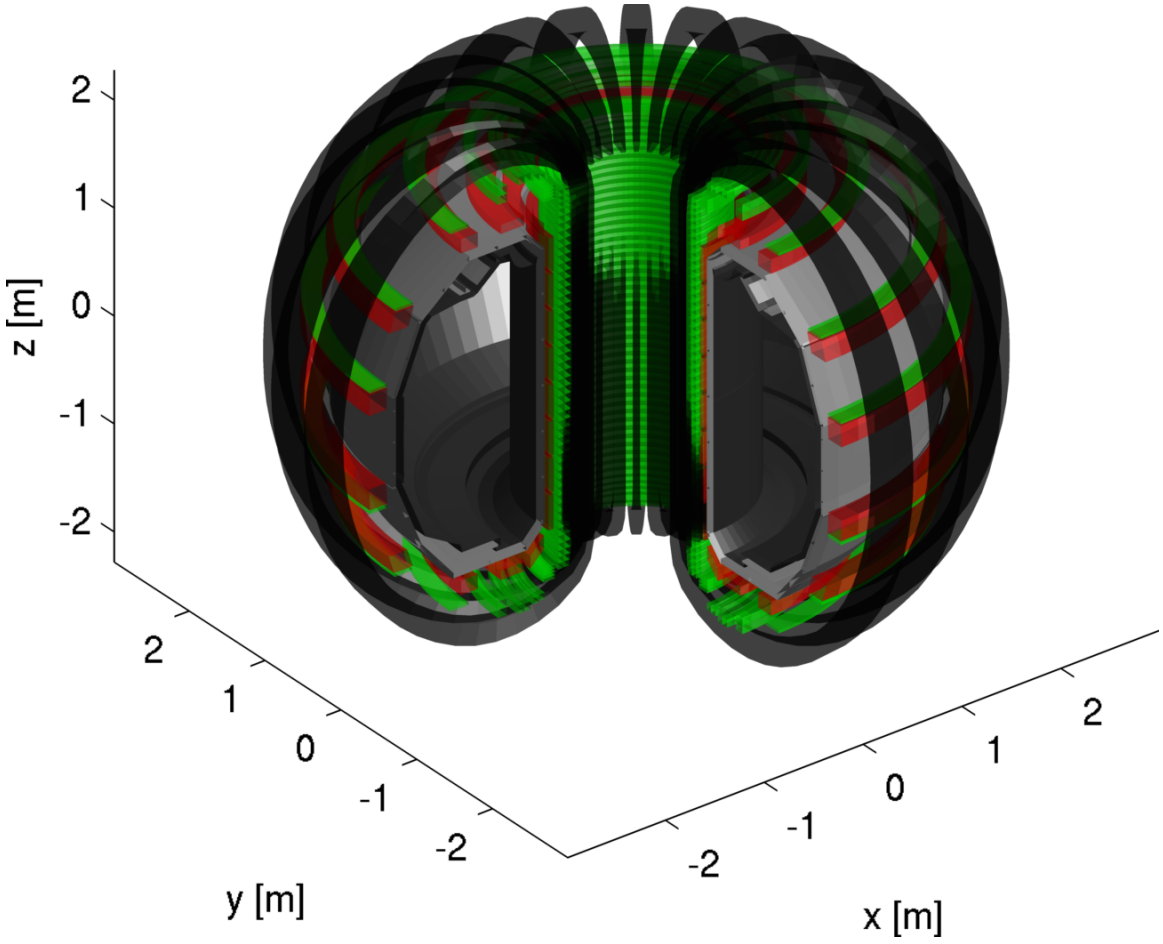

Figure 2.1: A 3D rendering of the DIII-D tokamak. From the outside in are: toroidal field coils (black), poloidal field/shaping coils (red), center solenoid windings (green), the Inconel vacuum vessel (grey), and graphite limiting surfaces (black).

Chapter 3

Experimental techniques for studying runaway electrons in tokamak disruptions

Over the course of this thesis work, new diagnostic and experimental techniques were developed for studying runaway electrons. Diagnostic analysis and interpretation was also adapted for the unusual conditions present during rapid shutdown experiments. This chapter summarizes these developments and adaptations.

3.1 Argon killer pellet injection and plasma shaping to generate runaway electrons

Studying runaway electrons (RE) required tailoring the tokamak operation and shutdown to generate as many RE as possible. These experiments begin by injecting an argon 'killer pellet' into a stable plasma, a technique first reported elsewhere [35] and previously shown [64] to generate more runaway electrons than other rapid shutdown techniques. Experiments were performed over a period of two years on six separate days of DIII-D operation, and represent results from 131 successful argon killer pellet shutdowns.

The killer-pellet is composed of frozen solid argon with dimensions $d = 2.7mm$ and $l = 2.7mm$, and is injected at velocities of $v = 500 - 800m/s$ using a cryogenic pellet injector developed at Oak Ridge National Laboratories. Argon has an atomic mass $A = 39.948g/mol$, and the solid has a mass density $\rho_{Ar} = 1.616g/cc$, and hence a number density $n_{Ar} = \rho_{Ar}/m_{Ar}N_A = 2.4 \times 10^{22}cm^{-3}$. The pellet volume of $V = \pi(2.7mm/2)^2(2.7mm) = 15.5mm^3$ contains $N_{Ar} = V \times n_{Ar} = 3.8 \times 10^{20}$ argon atoms, equivalent to $11.3torr \cdot L$ at room temperature. After spreading throughout the DIII-D vessel ($R = 1.67m$, $a = .67m$), this contributes an atomic density of $n_{Ar} = 2.5 \times 10^{13}cm^3$, or a total electron density of $n_e = Z_{Ar}n_{Ar} = 4.5 \times 10^{14}cm^3$. In practice, most of the injected argon remains only partially ionized and many electrons remain bound, so the resulting free electron density only reaches levels this high as a result of additional impurities assimilated from the vessel walls.

Two different plasma configurations were studied: a diverted, elongated ($\kappa = 1.7$), neutral beam heated, H-mode discharge; and a limited, lower elongation ($\kappa = 1.3$), electron cyclotron heated, L-mode discharge. Low elongation shapes were used because they were previously predicted [52] to result in greater and more frequent RE currents. Substantial RE current plateaus occured more frequently in the limited configuration, as shown in figure 3.1.

Plasma conditions in the two configurations were similar in some respects, but also differed in others. The average pre-shutdown core temperature $T_e \sim 2.3keV$ was similar in both cases, but ranged from $1 - 3.5keV$. In the diverted configuration the pre-shutdown line averaged density tends to be larger at $n_e \sim 1.7 \times 10^{14}cm^{-3}$ compared to $n_e \sim 6 \times 10^{13}cm^{-3}$ for the limited configuration. The edge safety factor $q_{95} \sim 3.3$ was similar in both cases, but ranged from $3.1 - 5$. In most of the diverted shutdowns, beam heating was used which continued roughly $10ms$ into the shutdown, while in all limited shutdowns, gyrotron heating was used instead of beams and was turned off a few ms before the shutdown. These quantities are shown in histograms in figure 3.2

Also similar in both cases are the apparent TQ and CQ timescales, which are found by fitting different functionals which best describe the dynamics. The

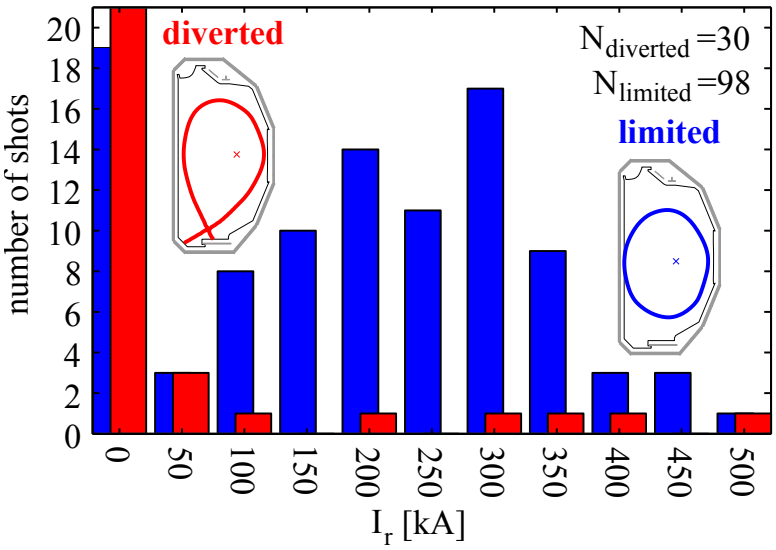

Figure 3.1: A histogram of plateau phase runaway current plotted for the two different experimental shapes showing increased frequency of runaway plateau for the limited shape.

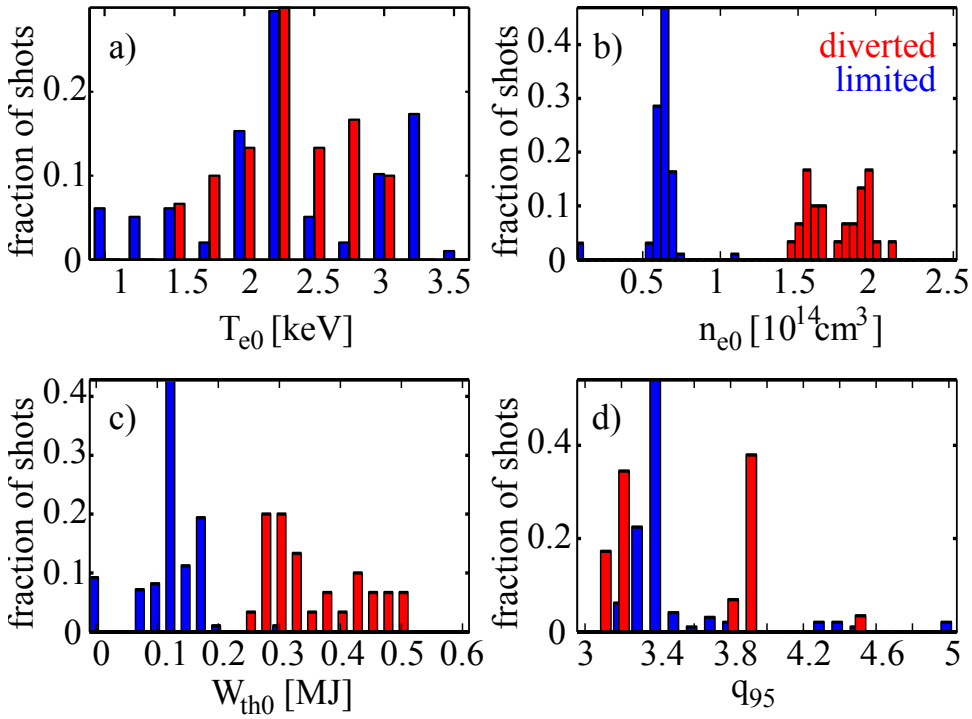

Figure 3.2: Histograms of the initial a) electron temperature, b) electron density, c) stored thermal energy, and d) edge safety factor.

TQ timescale $\tau_{TQ} \sim 200 - 300\mu s$ is found by fitting an error function $T(t) = T_0(\text{erf}(-t/\tau_{TQ}) + 1)/2$ to the broadband ECE signal during TQ. The CQ timescale $\tau_{CQ} \sim 3 - 4ms$ is found by fitting an exponential decay $I(t) = I_0\text{exp}(-t/\tau_{CQ})$ to the current measured during CQ.

RE signatures appear, in either case, only after inducing a rapid shutdown and not after occasional unintentional disruptions. This suggests that REs are generated as a consequence of the shutdown and are not remnant startup runaways.

3.2 Diagnostics for studying rapid shutdowns and runaway electrons

A thorough understanding of precisely how various measurements are made in a tokamak is important for unravelling the complicated physical phenomena which occur during operation. While a detailed explanation of every diagnostic used in a tokamak is outside the scope of this dissertation, this chapter summarizes the essential concepts important to diagnostics which are later invoked, and provides references which contain a more thorough explanation. For a general diagnostic overview, the 2008 special issue of Fusion Science and Technology on Plasma Diagnostics for Magnetic Fusion Research is an excellent reference [2]. Table 3.1 lists the primary diagnostics discussed and their relevant measured properties, and figure 3.3 shows each of these diagnostics situated with respect to each other.

Section	Diagnostic	Measured properties
3.3	Scintillators	Neutron flux and hard x-ray flux
3.4	Magnetic measurements	Plasma current and position
3.5	Bolometer arrays	2D radiated power profile
3.6	Interferometers	Line integrated electron density $\int n_e dl$
3.7	Electron cyclotron emission	Electron temperature profile $T_e(r)$

Table 3.1: Primary diagnostics used in this thesis.

Emphasis is placed on diagnostic hardware developed by the author during work on this thesis in section 3.3. Sections 3.4-3.7 describe diagnostics used extensively in this thesis, with considerations important for interpretation during disruption studies. Diagnostics which are only briefly mentioned in this thesis, or which do not function well during disruptions, are discussed in section 3.8.

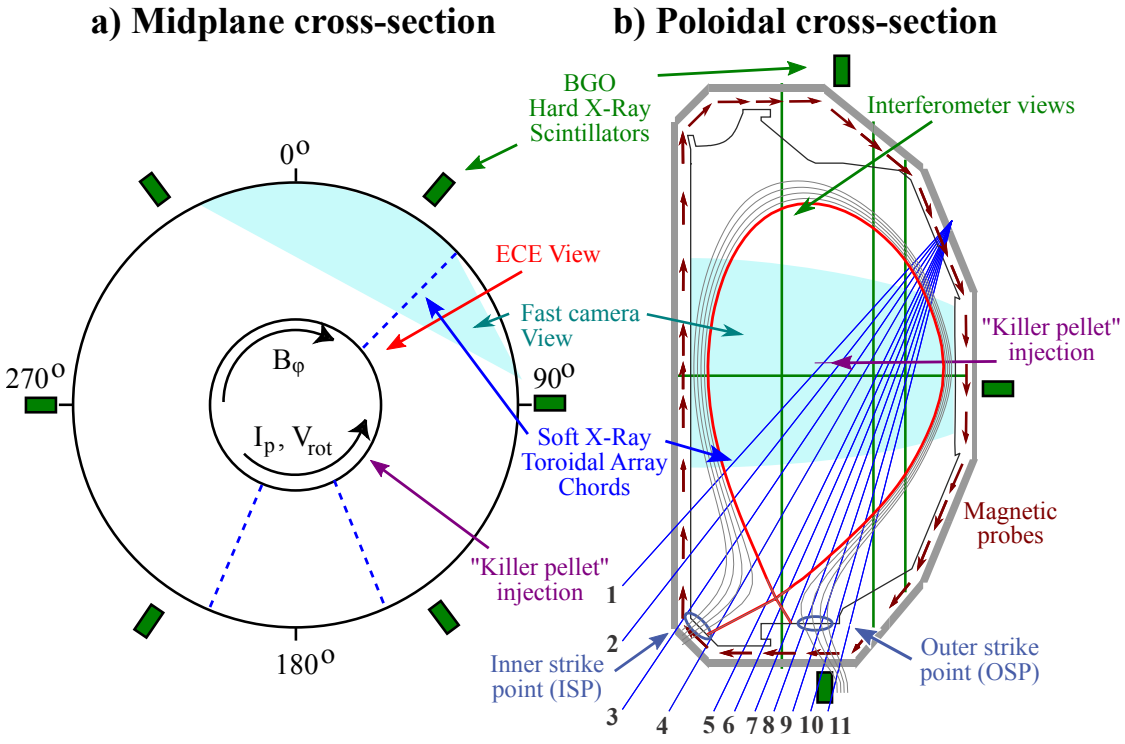

Figure 3.3: Diagnostic and hardware arrangement for the experiments discussed.

3.3 Hard x-ray sensing scintillators

This section presents details of a new bismuth germanate (BGO, $Bi_4Ge_3O_{12}$) scintillator array designed to diagnose the transport and energy behavior of runaway electrons (RE) in DIII-D by their emitted bremsstrahlung. It begins with some motivating comments, followed by a simple then thorough numerical consideration of bremsstrahlung emitted by runaways, later with a discussion of the scintillation detector design considerations, and finally with a presentation and physical interpretation of the resulting data.

3.3.1 Motivation

The design of this array was originally motivated by the large shot-to-shot variation of x-ray intensity from runaways observed on the neutron counting scintillator at DIII-D. Uncertainty existed over the cause of these variations: was there a shot-to-shot variation in the number or energy of runaways generated, was there an irregular impact location on the vessel wall causing an apparent variation, or could something else be going on? Since runaways are known to cause damage to vessel components, the answers to these questions would help guide placement of sensitive components, and also perhaps to prevent runaway generation through further understanding of the runaway phenomena. By surrounding the vessel with an external array of compact scintillators, these questions could be answered without the need for port access or the high cost and complexity of some type of camera system. The array described here provides clues to the answers of these questions by providing a measurement of hard x-ray emission with spatial, temporal, and energy resolution.

3.3.2 Modelling bremsstrahlung from runaway electrons

Modelling of relevant hard x-ray phenomena was performed using code 'Electron Gamma Shower' (EGSnrc) [91]. EGSnrc was developed at SLAC and the Canadian National Research Council (hence 'nrc'), and uses Monte-Carlo techniques to model the transport of electrons, positrons, and photons through ma-

terials. Most known scattering physics are contained in the code including non-exhaustively: photo-electric absorption, Compton scattering, pair production, and other mechanisms. The code has been well benchmarked against experiments at SLAC, and is used throughout the high energy physics and medical physics community for design of shielding, detection, and sources of high energy radiation.

Using EGSnrc, the x-ray spectrum absorbed in a 1"$\times$1" bismuth germanate scintillator from an electron beam striking a mock-up of the DIII-D graphite tiles and inconel vacuum vessel is shown in figure 3.4. The simulation geometry consists of a pencil beam of relativistic electrons ($r = 0.1mm$) impacting on a first wall graphite tile mocked up as a cylindrically symmetric disk of graphite ($r = 10cm$, $z = 7cm$), which is backed by a mocked up vacuum vessel section disk of Inconel 625 alloy ($r = 10cm$, $z = 17mm$). Another mock-up of runaways striking a small carbon pellet reproduces the well known relativistic forward beaming [75] that is more pronounced for higher energy RE than lower energy, and also more pronounced for the higher energy portion of the hard x-ray spectrum than the lower energy portion, shown in figure 3.5.

3.3.3 Detector design

Among the considerations important for the detector design were compactness, response time, dynamic range and signal intensity, shielding of electromagnetic noise, spatial distribution, and energy resolution. Brief discussions of each of these are presented below. For reference, a schematic of one detector of the array is shown in figure 3.6, and also a more detailed drawing in figure 3.7.

3.3.3.1 Scintillator selection

Important considerations in the selection of scintillators for measuring bremsstrahlung emitted by runaway electrons included high radiation stopping power and high light yield which enable compactness. Neutron blindness was also important as much as possible to simplify signal interpretation.

A high radiation stopping power maximizes the signal per unit mass of detector [94, 111], so that even compact detectors produce measurable signals with

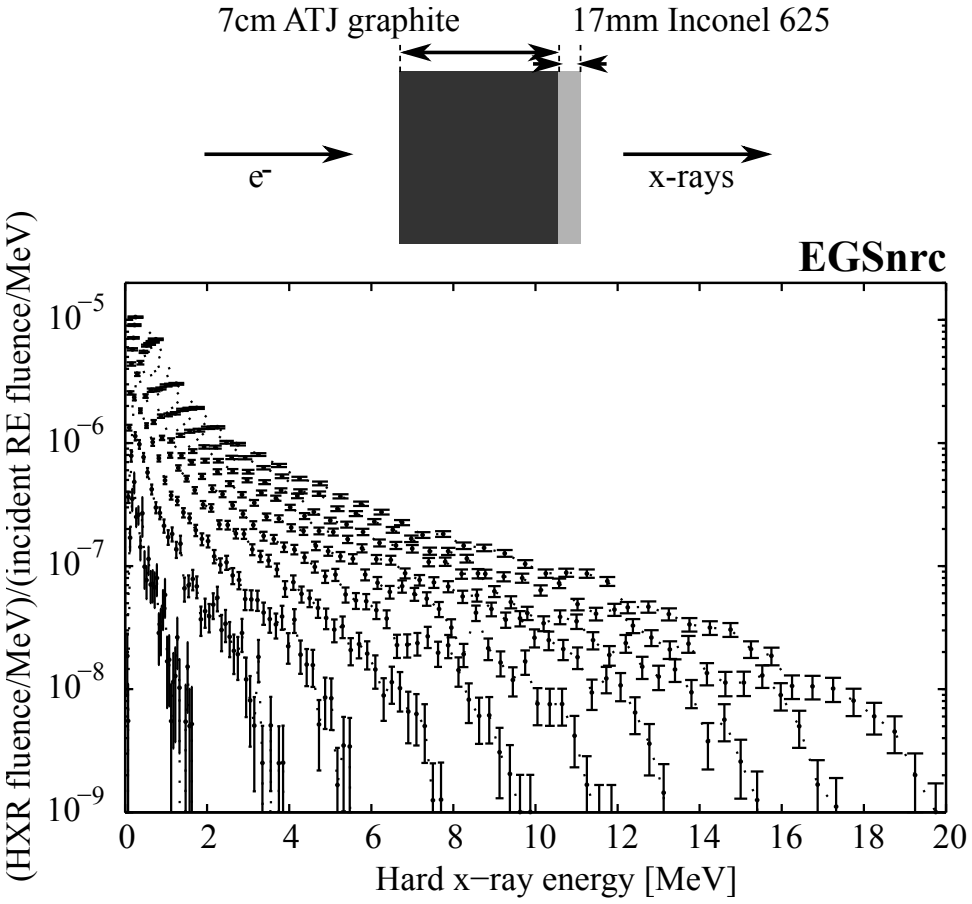

Figure 3.4: A cartoon of the EGSnrc geometry used for modelling x-ray spectra from runaways striking the DIII-D wall, and a series of those spectra observed outside the DIII-D vessel. Each curve terminates at approximately the incident RE energy.

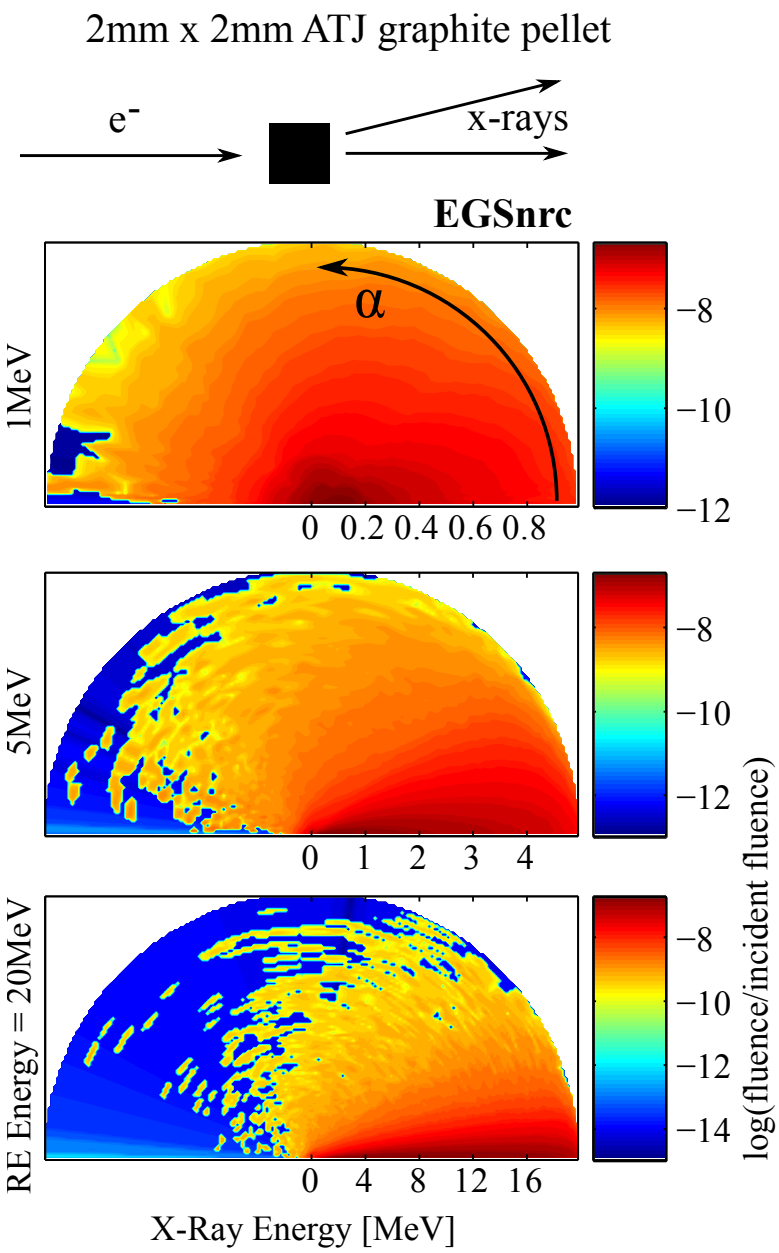

Figure 3.5: A cartoon of the EGSnrc geometry used for modelling x-ray fluence (color) vs. angle of incidence α and energy (radius) from runaways impacting a 2mm $\times$ 2mm carbon pellet, and a series of the resulting fluences for three different energy incident electrons.

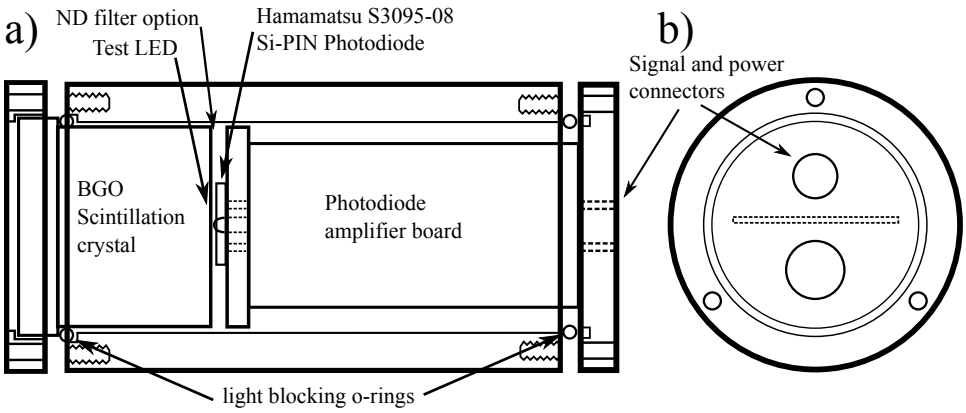

Figure 3.6: Drawing of detector assembly with a) side view and b) rear view.

decent energy resolution. To estimate the needed crystal size, it should attenuate roughly 50% of incident radiation at the desired photon energy, calculated as:

$$1 - \frac{I}{I_0} = 1 - e^{-t\rho\mu(W_\gamma)} \tag{3.1}$$

For photons with energy $W_\gamma = 10MeV$ incident on a BGO slab with thickness $t = 1in \sim 2.5cm$, density $\rho = 7.13g/cm^3$, and total attenuation cross section [16] $\mu = 4.24 \times 10^{-2}cm^2/g$, the attenuation is roughly $1 - I/I_0 = .54$ which indicates suitability for the common $1in \times 1in$ BGO cylinders commercially available.

During RE deconfinement, neutron radiation from D-D fusion reactions and photo-neutron emission from interaction between RE bremsstrahlung and tokamak components can complicate interpretation of observations. To avoid these complications, it is important to minimize energy deposition from neutrons in the scintillation medium. A typical collision analysis including conservation of energy and momentum between an incident neutron and various scintillator atomic constituents reveals that energy transfer per collision scales as $1 - (\frac{m_n - m_{sc}}{m_n + m_{sc}})^2$, where m_n is the neutron mass and m_{sc} represents the atomic mass of various scintillator constituents. Due to the high atomic weights of bismuth (Z=83, A=209), germanium (Z=32, A=73), and oxygen (Z=8, A=16), a BGO scintillator absorbs much less energy per neutron collision than organic scintillators which are typically rich in hydrogen, boron, carbon, and other low mass constituents, and are used for observing neutrons. This was confirmed by the observation during experiments

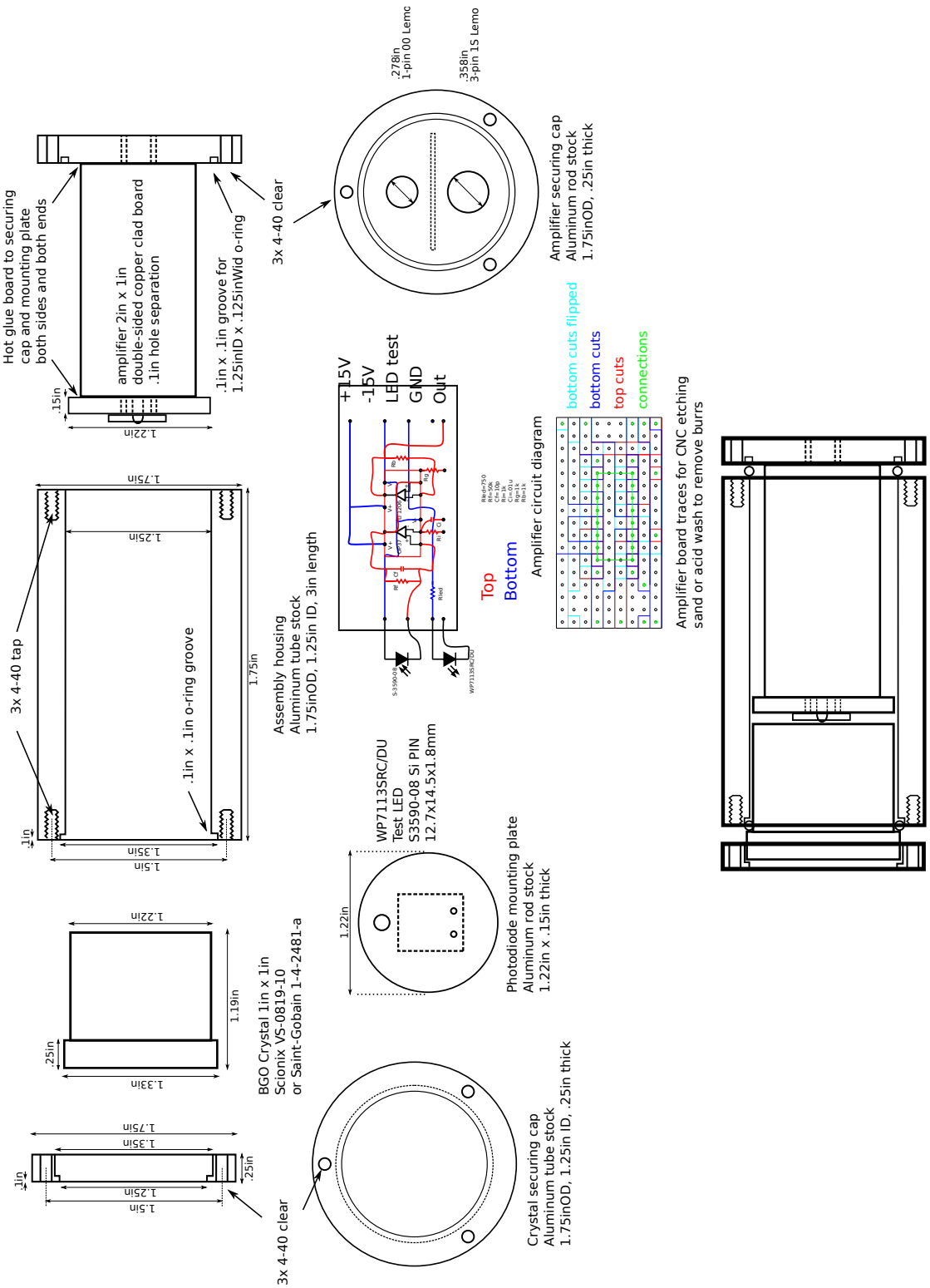

Figure 3.7: A detailed drawing of the scintillator detector design.

that BGO signals are entirely absent or small when a plastic scintillator used for sensing neutrons [58] measures peak neutron emission.

3.3.3.2 Amplifier and electronics

To convert the visible scintillation light into a line voltage a current amplifier was designed with gain and bandwidth selected to match the BGO scintillation time of $300ns$ and optimized for amplifier stability.

Current produced by photoelectric absorption of scintillator light in the Hamamatsu S3590-08 silicon PIN photodiode drives the positive input of an OP37 amplifier. The amplifier was configured for positive gain of $R_f = 50k\Omega = 50V/mA$ with a $C_f = 10pF$ capacitor added in parallel as a filter to enforce a bandwidth limit of $1/\tau_{RC} = 2MHz$. A line buffer amplifier supplies sufficient current to drive the resulting voltage signal down the $R = 50\Omega$ coaxial signal cable, which has a 50Ω termination at the high impedance input to the digitizer. A small gap was left between the photodiode and scintillator so that the signal could be adjusted by inserting a neutral density filter in addition to adjusting amplifier gain.

A light emitting diode was also installed to illuminate the photodiode for generating test signals, due to the unavailability for testing on the bench or in-situ of a radiation source with large enough flux of hard x-rays to sufficiently excite the detector as well as the severe hazard associated with such a source.

The frequency response was improved by reverse biasing the photodiode to narrow the depletion region, hence reducing internal capacitance. However, this also required that the reverse bias be filtered with a $.01\mu F$ capacitor to minimize coupling of power supply noise into the pre-gain stage. This filtering capacitor had little effect in in-situ implementation, but for bench testing the short power cables coupled small power supply switching oscillations into the pre-gain stage otherwise.

Power conditioning capacitors near the amplifier prevent a drain in line voltage and subsequent amplifier instability caused by high frequency current demand from a long power cable slowed in response by its own inductance. On the bench, the amplifier may function well without these conditioning capacitors, and

the transient overcurrent caused by charging the capacitors at powerup sometimes faults the power supply.

Two low-cost $15V$ switching power supplies rated at $150W$ were used for supplying power to 24 detectors each of which deliver up to $10V$ into a 50Ω line, for a design demand of $48W$.

Special attention to connecting assembly and connector housings to the digitizer ground required that they remained separate from machine ground in order to minimize noise and avoid ground loops which could occur if the assembly or connectors came into contact with grounded machine surfaces. Ground loop faults were protected against by electrically insulating connectors when not in use, and mounting detectors to the machine on $.5in$ insulating Lexan blocks.

3.3.3.3 Electromagnetic shielding

During operation, the tokamak environment contains many magnetic coils with high current and rapidly varying current which produces electromagnetic noise in nearby high gain amplifiers such as those used here. Any thin conducting housing easily shields out static electric fields, but magnetic fields still penetrate on long enough time scales. These problems were avoided through application of electromagnetic shielding with a $\delta = 0.25in$ thick high conductivity $\sigma = 3.77 \times 10^7/\Omega m$ aluminum housing. Magnetic fields changing faster than the inherent field penetration time τ do not penetrate to the amplifier, and hence are shielded out.

$$\tau = \pi \mu_0 \mu_r \sigma \delta^2 = 6ms \tag{3.2}$$

3.3.4 Array arrangement

To provide coverage for observation points surrounding the machine, scintillators were arranged into four separate arrays: three poloidal arrays of three detectors placed near the bottom of the machine, the midplane, and near the top respectively; and one toroidal array of six detectors arranged around the midplane with sixty degree separation. This layout arrangement is shown in figure 3.8. The

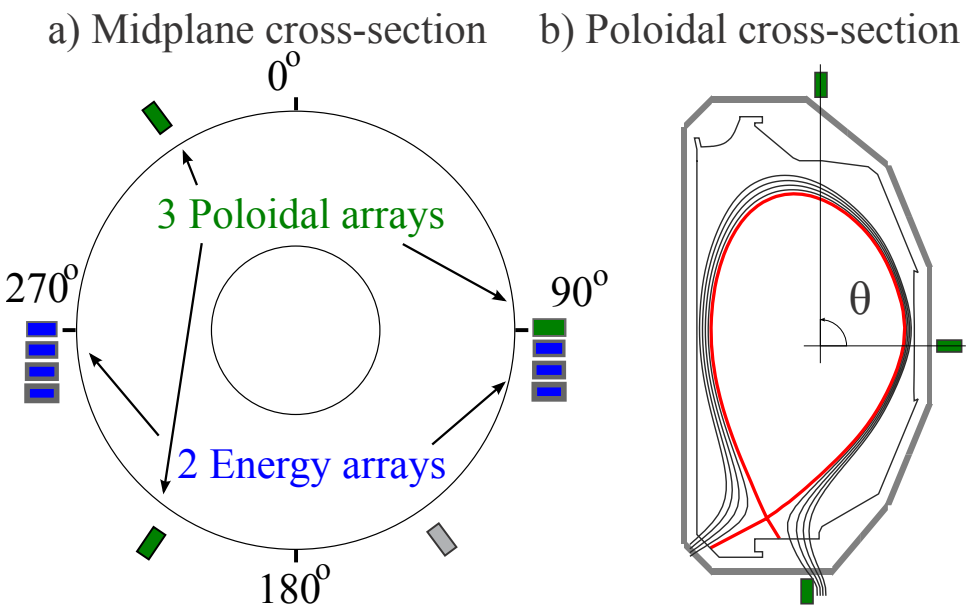

Figure 3.8: Spatial arrangement of a) midplane toroidal and b) poloidal scintillator arrays.

arrangement was chosen to reveal small hard x-ray bursts from runaways striking first wall materials on the opposite side of the machine from the existing BC400 neutron scintillator [58], and to identify the runaway strike topography throughout a disruption [78]. Visualizing the strike topography revealed by this arrangement is most straighforward by plotting detector intensities on a contour plot with the toroidal and poloidal detector locations roughly mapped to the x and y axes respectively, as shown in figure 3.9d, though caution is merited for interpretation between detectors due to the array sparsity. Most detector locations were shifted slightly to work around space constraints on the tokamak, and one detector failed so only five are shown at the midplane.

3.3.5 Runaway energy resolution

Energy resolution is limited by the size of the scintillator crystal due to the possibility of partial x-ray energy deposition in the crystal, since some energy from the electron, positron, and x-ray shower can escape. Such escape manifests as various features in the energy resolution curves: peaks located one and two

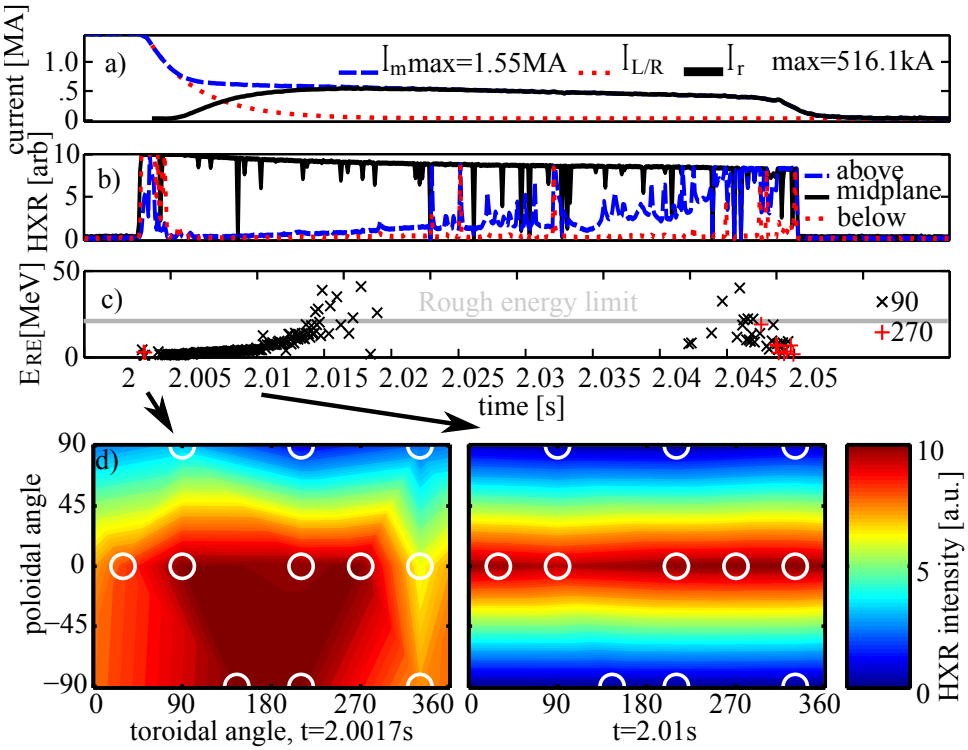

Figure 3.9: Scintillator array signals in a disruption with a) significant runaway electron current I_r (measured by subtracting a fitted L/R current decay $I_{L/R}$ from the total measured current I_m), b) time traces from the poloidal array at 90 degrees with detectors above, near (mostly saturated), and below the midplane, c) energy estimated with the shielded detectors, and d) contour plots showing spatially resolved emission at two times, with detector locations circled.

times the electron rest energy $m_e c^2 = .511 MeV$ below the full energy peak result from escape of either or both particles in electron-positron pair production, and a lower energy Compton continuum from partial energy deposition via Compton scattering in the crystal. As photons become too high energy to stop in the crystal, the full energy peak decreases in amplitude, and the entire deposited spectrum washes out into one broad Compton continuum. For energies above which the full energy peak decreases beneath this compton continuum, the energy resolution of the crystal becomes poor. A typical energy resolution simulation is shown for a BGO scintillator performed with the EGSnrc code in figure 3.10, which indicates the rough limit of full photon energy detection of around $20 MeV$. For photons of higher energy than $20 MeV$ the full energy peak gradually vanishes, indicating that most photons of these energies incident on the detector only deposit some fraction of their energy there.

Even after passing through the DIII-D vessel wall, enough energy information remains in the x-ray spectrum (shown in figure 3.4) to estimate electron energy. This can be done by blanketing a series of four detectors in varying thicknesses (0, $1mm$, $2mm$, and $4mm$) of lead shielding, which attenuates x-ray intensity on the detectors with an energy dependence. Matching the attenuation length measured by this set of detectors with an attenuation length simulated for the system using EGSnrc [91], shown in figure 3.11, allows us to infer runaway energy. Figure 3.9c depicts time histories of runaway energy estimated with this technique throughout a runaway plateau, where the energy limit described above is apparent.

3.3.5.1 Photo-neutron signals

This method of energy detection increases in complexity with the presence of photo-neutrons generated by observed x-ray emission. These would appear as a signal in the detectors unvarying with shielding thickness since neutrons penetrate lead far better than photons, reulting in an anomolously large measured energy. Other studies [139] attribute radiation emission from RE deconfinement to these photo-neutrons, however a majority of radiation flux results from hard x-ray photons, with only a small proportion of hard x-rays converted to photo-neutrons.

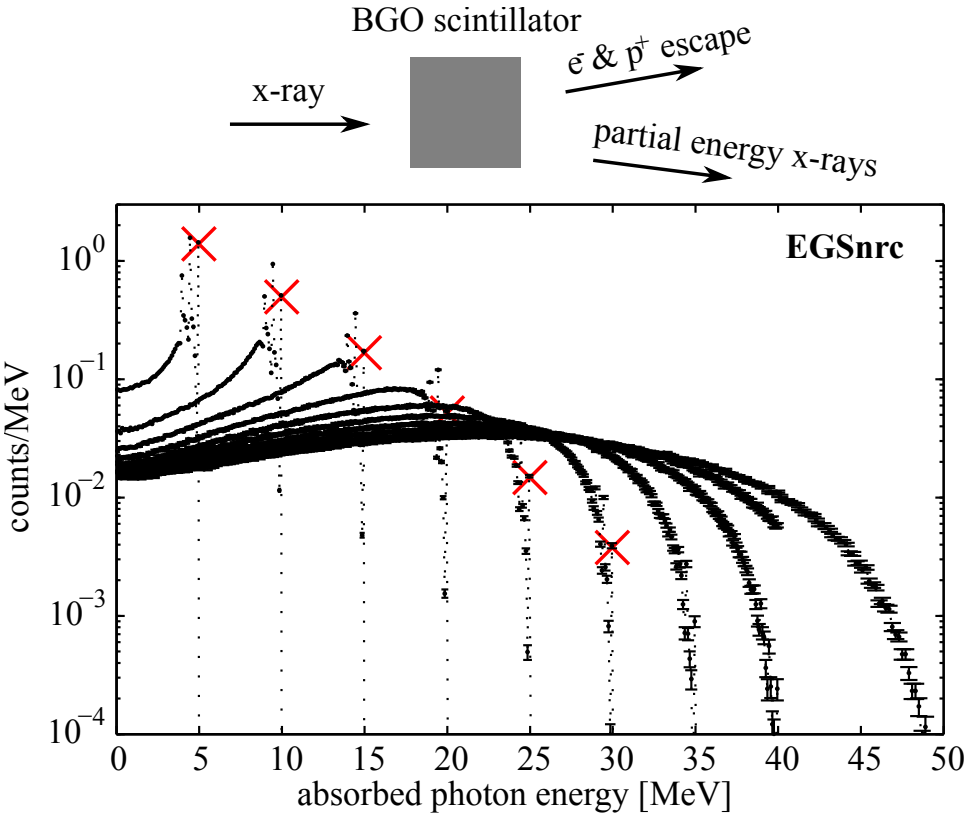

Figure 3.10: A cartoon of the processes contributing to finite energy resolution in scintillators, and energy resolution curves calculated for a $1in \times 1in$ BGO scintillator to various photon energies using EGSnrc Monte-Carlo modelling. Each curve terminates at approximately the incident photon energy, with the full energy peaks marked with an $\times$ where visible.

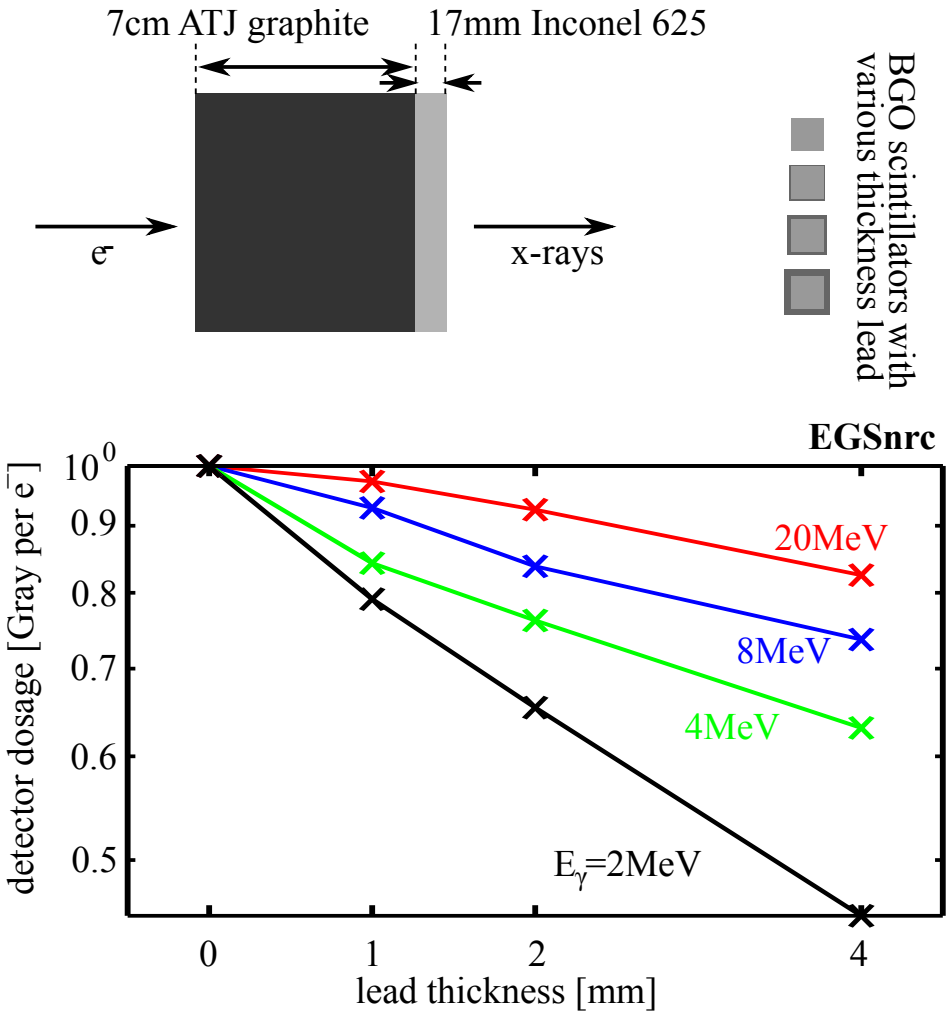

Figure 3.11: A cartoon of the geometry used in EGSnrc to model the apparent attenuation length in detectors shielded by various thicknesses of lead, and the resulting detector dosages per electron for various incident electron energies.

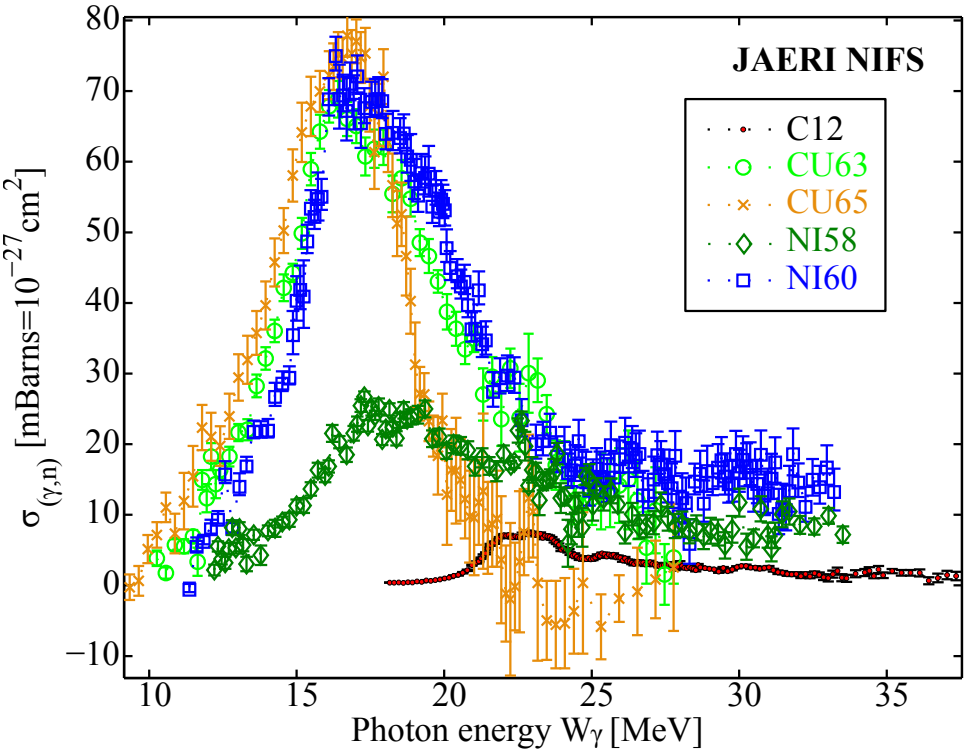

Figure 3.12: Photoneutron production cross sections for a selection of common tokamak materials [127, 1].

Certain materials common in tokamaks dominate photo-neutron production due to their 'giant resonance' photo-neutron cross-sections (fig 3.12). These materials include nickel, copper, and carbon. The exponential decay of the hard x-ray bremsstrahlung spectrum approaching the incident electron energy (fig 3.4), results in only about 10% of the hard x-ray flux falling within the giant-resonance, even for the highest energy ($50 - 100MeV$) runaway electrons. Considering only this interaction cross-section and neglecting others, an upper limit for the photo-neutron conversion fraction is predicted:

$$f \leq nl \int f_\gamma(W_\gamma)\sigma_{(\gamma,n)}(W_\gamma)dW_\gamma \tag{3.3}$$

where l is the material thickness, n is the material solid density of relevant atomic centers, $f_\gamma(W_\gamma)$ is the hard x-ray source probability distribution function (see fig 3.4), and $\sigma_{(\gamma,n)}(W_\gamma)$ is the energy dependent photo-neutron production cross-section. Even for x-ray sources from the highest energy RE, this fraction usually works out to only about 0.1%. In addition, much of the photon energy is expended breaking the neutron loose from nuclear bonds, so the resultant neutron carries only a small fraction of the incident energy.

In addition to the smallness of photo-neutron flux compared with hard x-rays, BGO detectors absorb much less neutron flux than they do x-ray flux, again due to the high constituent atomic masses and the high density and constituent atomic numbers. X-rays deposit energy in the detector primarily by Compton-scattering, with deposition strongly increasing with atomic number Z and material density. By contrast, neutrons deposit energy primarily through elastic nuclear scatterings with reduced energy deposition as Z increases. The result is that BGO scintillators are poor neutron detectors, and exhibit substantial neutron blindness.

3.3.5.2 Radiation damage to silicon detectors

Silicon photodiode properties degraded significantly over the two years of array operation. In two years since the detectors were first installed at DIII-D, dark current increased by an order of magnitude or more, and the photodiode gain reduced by roughly a factor of two. Damage occurs to the silicon junction from neutron flux [118, 47, 20], resulting in an increased dark current and a decreased gain.

This change in the detector characteristics requires a more frequent detector calibration than was executed during the array operation, so that the energy resolved results were invalidated except shortly after installation of the array. Consideration of the damage described above could restore the energy resolution even without frequent calibrations, but that analysis has not been attempted presently. This damage will eventually degrade the detector properties enough that replacement will be necessary, so future modifications should also consider neutron degradation lifetime of detectors. New large area (1cm x 1cm) CMOS photomultipliers are becoming available [88], and will hopefully be less susceptible to neutron degradation while also giving a higher gain than the photodiodes currently in use.

3.4 Magnetic diagnostics

Magnetic measurements are one of the most robust diagnostics during disruptions, but there are a few caveats in interpretation and processing of the data for analysis. For an overview of magnetic diagnostics in general, an excellent review article exists written by E. J. Strait [157].

A poloidal array of magnetic probes measures the poloidal magnetic field generated by the plasma. While these probes are often digitized at a rate of $5kHz$ during disruptions, certain calculations (eg the loop voltage analysis from section 6.3.3) require a faster digitization. Generally voltages from the probes are passed through an integrating circuit before digitization, but the signal is also digitized before the integrator at an increased rate of $100kHz$. Since magnetic probes are installed internal to the vacuum vessel at DIII-D, they are not limited in time resolution except by their self inductance which gives them a $-6dB$ bandwidth of $\sim 250kHz$ [156]. By integrating these signals in software and matching the offset of the hardware integrated signals, a faster signal is reconstructed when necessary. Typically the normalized root mean square deviation between the software and hardware integrated signals is less than 10^{-11}, indicating a good agreement between the two techniques. A perspective view of most of the magnetic probes installed at DIII-D is shown in figure 3.13, and a poloidal plane view of only the poloidal

array is shown in figure 3.14.

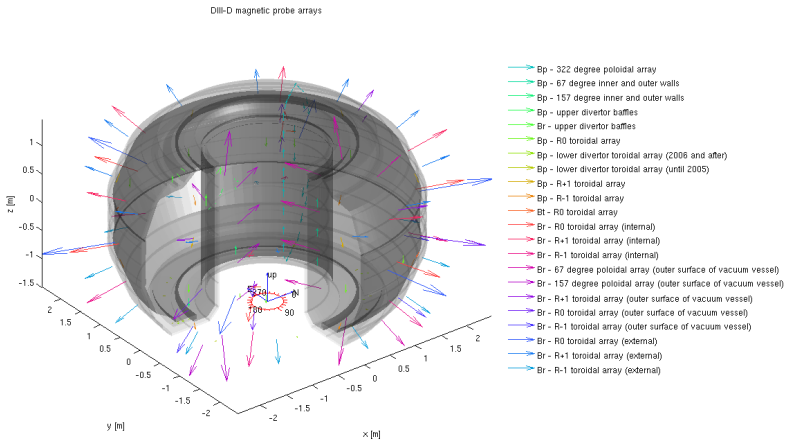

Figure 3.13: A 3D rendering of the various magnetic probe arrays installed at DIII-D.

The voltage induced across flux loops is directly digitized, and also integrated to measure the poloidal magnetic flux enclosed by the loop. Sometimes this voltages is interpreted as the plasma loop voltage, though on fast timescales this is innacurate. Because these loops are located outside the vessel, they are limited to an effective bandwidth of $\sim 200Hz$ by both low pass filtering from the conducting wall and the integrator circuit time constant. A perspective view of the flux loops is shown in figure 3.15, and a poloidal cross-section view is shown in figure 3.14.

Rogowski coils are installed at three different toroidal locations outside of the vacuum vessel to measure the sum of plasma and vessel current in the toroidal direction, however these are also limited in bandwidth by low pass filtering from the wall. A weighted sum of the poloidal array of magnetic probes constitutes a synthetic Rogowski coil which does not link the vessel current, and hence can be used for a higher bandwidth measurement of the plasma current without vessel current.

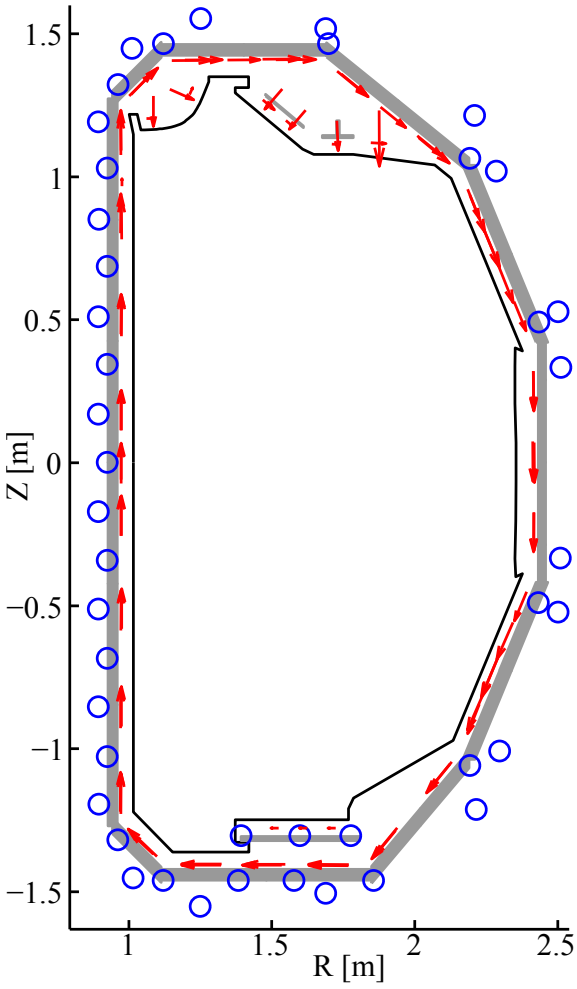

Figure 3.14: Flux loops (blue circles) and magnetic probes (red arrows) shown in a poloidal cross-section.

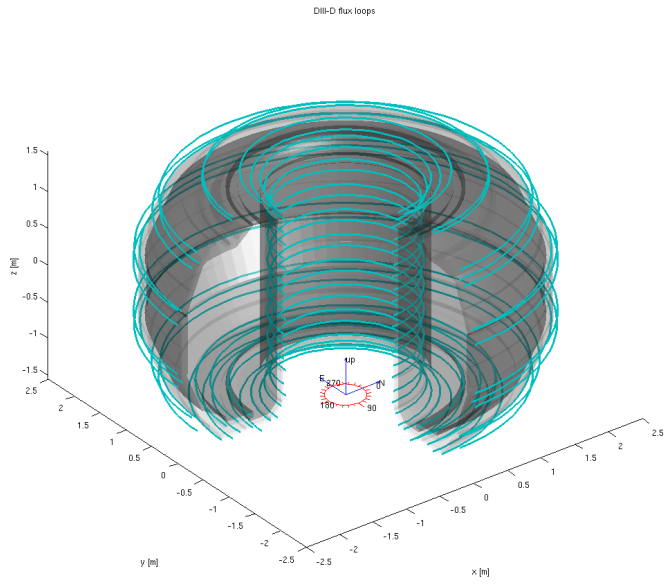

Figure 3.15: A 3D rendering of the various flux loops installed at DIII-D.

3.5 Bolometer and soft x-ray arrays

The detectors used in the soft x-ray arrays and bolometers are sensitive in the range of near-infrared to roughly 10keV, and can be filtered to select a specific spectral region of interest. Each detector views a narrow chord of the plasma region through a pinhole. A poloidal array of chords equipped with optional diamond filters is situated at 90 degrees both above and below the vessel [153], another poloidal array of chords views only unfiltered light at 210 degrees from above the vessel (referred to as DISRAD [53]), and three poloidal arrays of chords equipped with $125\mu m$ beryllium filters view $2-10keV$ soft x-rays from above the vessel at 45, 165, and 195 degrees [153]. All of these chord geometries are shown in perspective in figure 3.16, and in poloidal cross-sections in figure 3.17.

When RE are present, hard x-rays emitted from their impact with impurities and the walls can penetrate the pinhole, hence resulting in non-localized illumination of the detector. For RE currents in the range of hundreds of kiloamps, the detector signals are generally dominated by this non-localized emission,

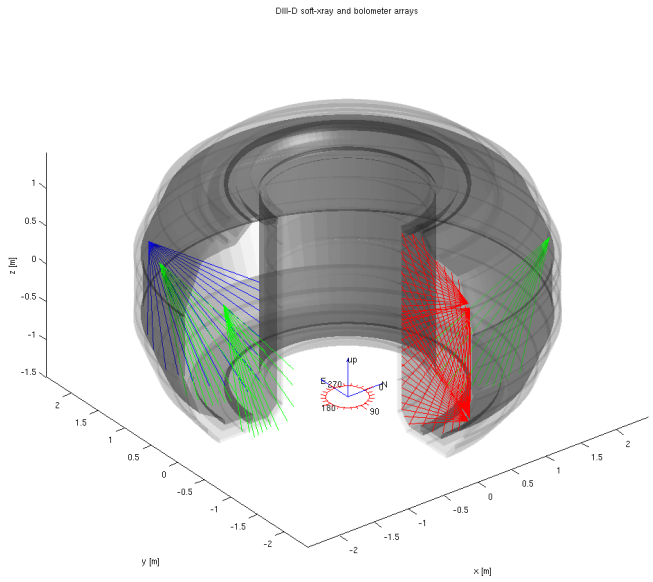

Figure 3.16: A 3D rendering of views for the various soft x-ray and bolometer arrays installed at DIII-D.

so localized interpretation of soft x-ray signals is not typically possible during these events.

3.6 Interferometers

Line integrated electron density is measured at DIII-D using a system of two-color interferometers. Three vertical chords view through the vessel at 240 toroidal degrees at $R_{V1} = 1.48m$, $R_{V2} = 1.94m$, $R_{V3} = 2.10m$; and one chord views horizontally along a major radius at the midplane and 225 toroidal degrees, as shown in figure 3.18. All four chords are reflected off of corner reflectors and return along the same path, hence they measure the double pass density. The vertical chords use the same wavelength pairs of $\lambda_1 = 10.59\mu m$, $\lambda_2 = 633nm$, and the horizontal chord uses $\lambda_1 = 10.59\mu m$, $\lambda_2 = 3.39\mu m$.

As explained elsewhere [174], in each chord the measured phase shift for each laser contains information about the plasma density and vibration of the mirrors

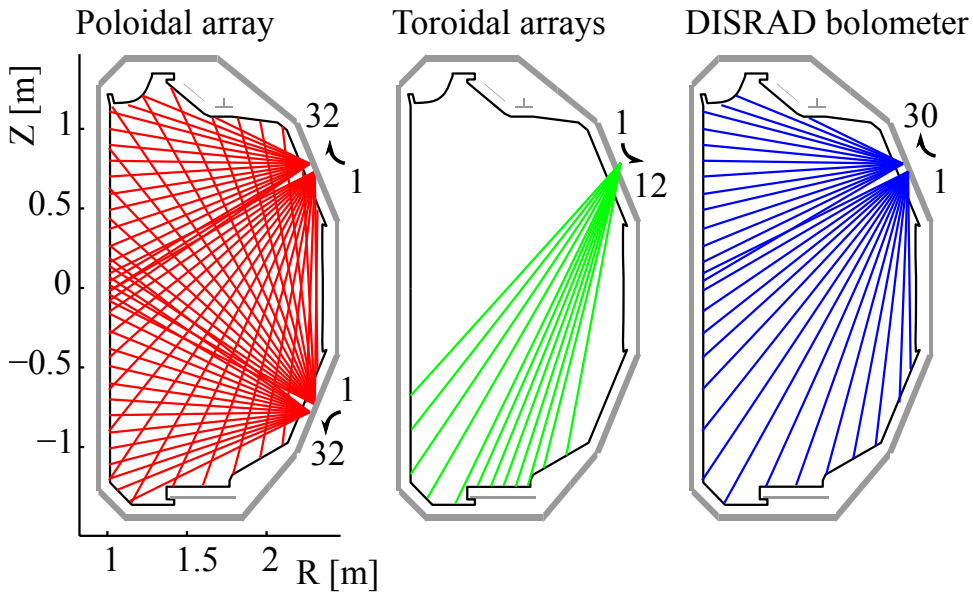

Figure 3.17: Poloidal cross-section views of the soft x-ray and bolometer arrays.

along the path length. Use of two colors allows separation of this information:

$$\begin{aligned} \phi &= A\lambda + B/\lambda, \\ A = 2.82 \times 10^{-15} \int n_e dl &= k n_{av} L, \\ B &= 2\pi V, \end{aligned}$$

where ϕ is the phase shift, L is the path length through the plasma, and V is the vibration. So the line averaged density and vibration can then be expressed as functions of the wavelengths used and the phase shifts:

$$\begin{aligned} n_{av} &= \frac{\lambda_1}{kL(\lambda_1^2 - \lambda_2^2)}(\phi_1 - \phi_2 \lambda_2/\lambda_1), \\ 2\pi V &= \frac{\lambda_2 \lambda_1^2}{(\lambda_1^2 - \lambda_2^2)}(\phi_2 - \phi_1 \lambda_2/\lambda_1). \end{aligned}$$

3.6.1 Fringe skips, and corrections

The heterodyne design of the interferometer system requires digitization of the intermediate frequency at a rate fast enough that the phase changes less than 90 degrees per digitization, roughly $2MHz$. Still, fringe skips where the phase changes

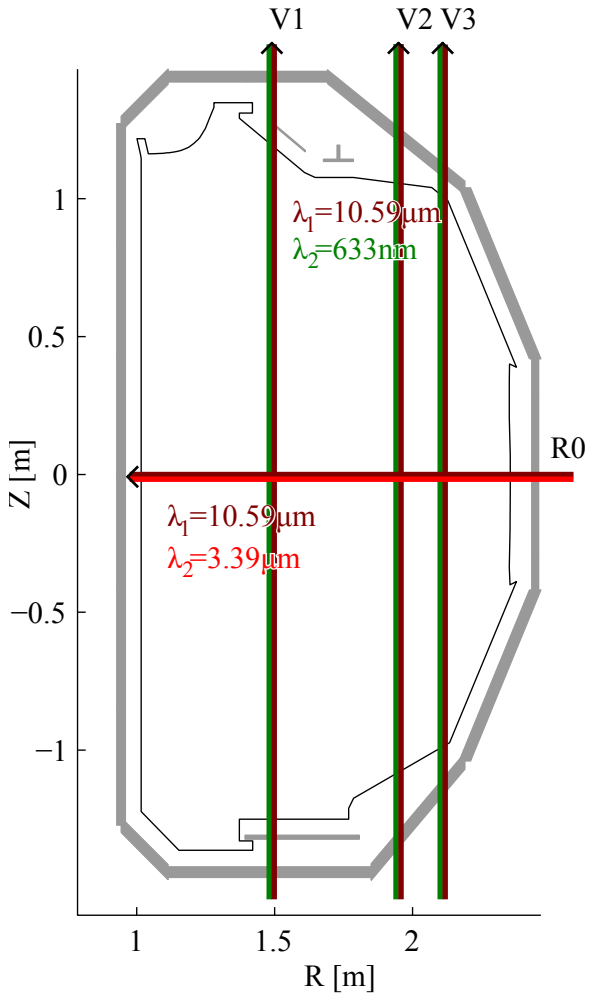

Figure 3.18: Geometry used for the interferometers, with corner reflectors shown.

more than 90 degrees occasionally occur during rapid shutdowns for two separate reasons. When the plasma density rises too rapidly, the phase changes faster than the system can track. When the density gradient is too great, wavelength dependent refraction of the lasers results in separation of the beams. Once the co-linearity is eliminated this way, the interferometric amplitude vanishes, resulting in a similar fringe skip. Refraction affects the longer wavelength laser more strongly, but shorter wavelength lasers require a faster system to measure the same rate of density change.

These interferometric fringe skips result in an offset of the density from its true value. Since the plasma density invariably returns to zero after a discharge, this can be used to correct the fringe skips. By distributing any offset between all the times at which fringe skipping occurs, the density time history can be forced to return to zero at the end, with uncertainty only between the first and last times of fringe skipping since the respective offsets within that range cannot be known. Fortunately, fringe skips only generally occur during a brief period just following impurity injection, so this technique works well during most disruptions. Such corrections are shown in figure 3.19.

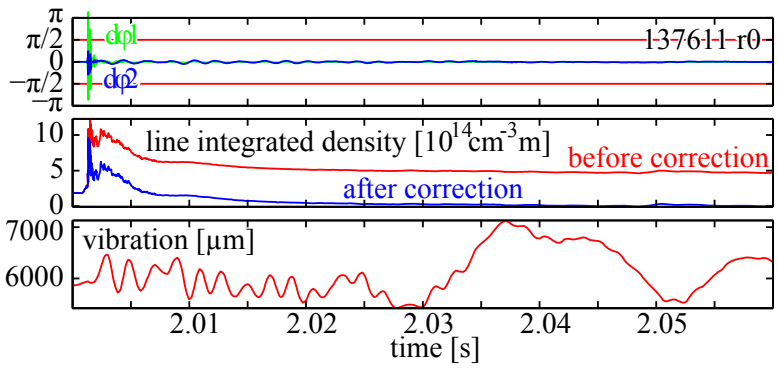

Figure 3.19: Interferometer data from a rapid-shutdown with corrections from fringe skips.

When an improved measurement of line averaged density is desired, the total interferometer path length through the region enclosed by the separatrix can be used. This technique tends to be quite robust against plasma motions, except at the extremities of vertical instability when the path length through the enclosed

region goes to zero and finite plasma density in the boundary region causes the measurement to diverge. Figure 3.20 illustrates this technique.

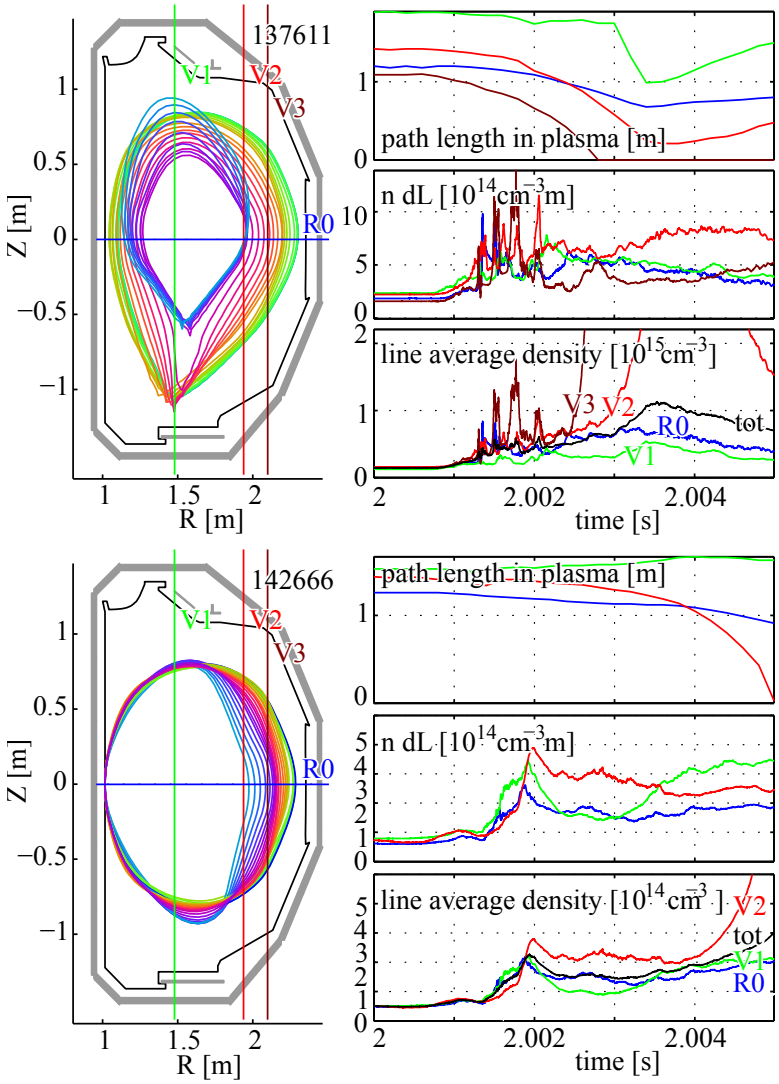

Figure 3.20: Processed interferometer data including effective path lengths through the last closed flux surface (LCFS) found using JFIT [68] reconstructions. The LCFS is plotted from green to blue along the time interval shown.

3.7 Electron cyclotron emission

Two electron cyclotron emission (ECE) diagnostics existed at DIII-D during these experiments: a channelized $110GHz$/2nd harmonic system, and a spectrally integrated $40-300GHz$ broadband system generally used for a Michaelson interferometer. Typically the ECE system is used for measuring plasma temperature, but it also measures emission associated with non-thermal electrons [93] and beam instabilities [89] when RE are present. Both the broadband and channelized systems occasionally observe cyclotron emission bursts associated with non-thermal electrons, and the broadband system observes a steady emission during runaway plateau, but the specific physical interpretation of these emissions remains unclear. These bursts complicate thermal interpretation of the broadband signal, but by fitting an error function to the portion through the end of the thermal quench, non-thermal artifacts can be excluded.

3.7.1 ECE cutoff

Right handed x-mode n-th harmonic thermal electron cyclotron emission (ECE) can be reflected by the plasma when the right hand cutoff frequency [114] exceeds the cyclotron frequency of interest: $f_r = (f_{ce}+(f_{ce}^2+4f_{pe}^2)^{1/2})/2 \geq nf_{ce}$ where the electron plasma frequency is $f_{pe} = \sqrt{n_e e^2/m_e\varepsilon_0}/2\pi = 28GHz\sqrt{n_e/10^{13}cm^{-3}}$ and the electron cyclotron frequency is $f_{ce} = eB/2\pi m_e = 56GHz(B/2T)$. This cutoff condition can be re-arranged to express a density limit for cutoff of the n-th harmonic ECE: $n_e \geq (n^2-n)\varepsilon_0 B^2/m_e = (n^2-n)3.9\times10^{13}cm^{-3}(B/2T)^2$. To avoid this cutoff, ECE systems are typically designed to use the second harmonic ECE which is more robust against such cutoff, but even the second harmonic $110GHz$ ECE can be cutoff where the density increases beyond $7.8\times10^{13}cm^{-3}$. A density of over $2.3\times10^{14}cm^{-3}$ is necessary for cutoff of the third harmonic ECE viewed by the broadband ECE diagnostic. As discussed in chapter 4, this may occur shortly after the TQ in rapid shutdowns.

3.8 Other diagnostics

DIII-D is equipped with several other diagnostics which are either invoked to a lesser degree in this thesis, or which are not used because they malfunction during disruptions. The diagnostics which were used are discussed in the following sections 3.8.1-3.8.3. The essential problems with malfunctioning diagnostics are also briefly described in section 3.8.4 to help future investigators avoid misinterpretation during rapid shutdown experiments, or other experiments with strongly radiating impurities.

3.8.1 Fast visible camera

A Phantom v7.1 fast camera system observes visible light emitted from the DIII-D plasma through a glass fiber optic bundle and associated optical lenses. The camera has a maximum framerate of roughly $25kHz$, and the exposure time can be adjusted down to $1\mu s$ to optimize for exposure. It is also equipped with an array of band-pass filters for selecting specific wavelengths such as C I, C II, D-α, Ar I, Ar II, and also a long wavelength passing filter for observing red to near-infrared light, all of which are remotely switchable. In addition to line emission from impurities and D-α, and bremsstrahlung emission, the fast camera also views synchrotron emission from high energy runaway electrons [85]. Through the observed intensity of synchrotron emission, runaway electron energy can be estimated using techniques described elsewhere [173].

3.8.2 Reflectometers

The profile reflectometer system at DIII-D is a relatively recent addition to the diagnostic suite [163] which is used to measure the electron density profile at high time resolution. Time resolution $\geq 10\mu s$ is sufficient even for TQ timescale studies, but the upper density limit of $\sim 6.43 \times 10^{19} m^{-3}$ means that reflectometry is only useful for probing the edge region when the electron density becomes large. When the electron density is large, the reflectometer still measures the radial location of the upper density limit which can be useful for comparing with the last

closed flux surface location predicted by magnetic diagnostics.

3.8.3 EUV Spectroscopy

Spectroscopy of extreme ultra-violet (EUV) emissions [38] is used to measure impurity content in plasmas. The $1ms$ maximum time resolution of the EUV spectrometer camera is a bit slow for TQ studies, but is sufficient for monitoring impurity content on CQ timescales. In addition to the presence of various impurities, the relative density, temperature, and effective charge state of various impurities could possibly be inferred from these spectra, however this analysis is not routinely done and requires that conditions of local thermodynamic equilibrium (LTE) and coronal equilibrium (CE) are satisfied. During impurity injection experiments, intense line radiation cools the plasma so rapidly that the conditions of LTE and CE are questionable so this analysis was not pursued further. The intensity of various impurity spectral lines can be difficult to measure in the presence of the numerous intense lines radiated by argon in impurity injection experiments, so the full spectrum must be inspected to insure that no nearby lines are interfering with desired measurements.

3.8.4 Other spectroscopy

Many other spectroscopic measurements at DIII-D do not operate properly when spectral lines radiated by injected impurities interfere with the observation, or because of impurities interfering with supporting systems. Such diagnostics include at least: visible bremsstrahlung, Thomson scattering, charge exchange recombination (CER), and the motional Stark effect (MSE).

The visible bremsstrahlung diagnostic [147] measures the effective charge state using an array of photo-multiplier tubes (PMTs) which view a chord through the plasma through a band-pass filter selected to pass a narrow spectral region (30Å $FWHM$ centered at 5230Å) in which only the visible bremsstrahlung continuum typically emits. During argon impurity injection, several argon lines overwhelm the bremsstrahlung and interfere with this measurement.

The Thomson scattering diagnostic [119] measures electron temperature and density by fitting the line shape of Thomson scattered laser light using a monochromator system. Stray light from argon line radiation overwhelms this Thomson scattered light during impurity injection experiments, rendering the Thomson system useless.

At least two diagnostics depend on emission from neutral beam particles: charge exchange recombination, and the motional stark effect. Argon line radiation also overwhelms these observations, since they rely on spectroscopic measurements. Injection of argon killer pellets does not cause any substantial problems with the neutral beams. In some killer pellet experiments, beams even continued heating the plasma up to $15ms$ into the shutdown with no observable effect on the dynamics, and no adverse effect on the beams. Experiments with massive gas injection, on the other hand, resulted in substantial damage of the high-voltage neutral beam source due to arcing caused by the enormous density increase.

3.9 Flux function reconstructions

Awareness of the plasma geometry during operation is important for plasma control and analysis, but re-construction of the flux function is a non-trivial inverse problem. The mathematics of inverse techniques are reviewed in a textbook by Robert L. Parker [131]. As described in section 3.8, many diagnostics either fail to function properly during disruptions or do not operate on timescales sufficient for observing the fast phenomena, so reconstructions during disruptions are typically constrained only by a subset of fast magnetic diagnostics. Two separate reconstruction codes were used in this thesis work to find inverse solutions of the plasma conditions using these magnetic diagnostics: the code EFIT described in section 3.9.1, and the code JFIT described in section 3.9.2.

3.9.1 EFIT

Solutions to the Grad-Shafranov equilibrium are returned by the code EFIT, which has been described thoroughly in a prior publication [105], so only a brief

synopsis is provided here. EFIT reconstructs magnetic flux surfaces satisfying a Grad-Shafranov equilibrium:

$$j_\phi = \frac{dp}{d\psi} - f\frac{df}{d\psi}/R \tag{3.4}$$
$$f = \frac{\mu_0 B_\phi}{R}$$

by fitting the quantities $\partial p/\partial\psi$ and $f\partial f/\partial\psi$ to available data. To achieve rapid reconstructions for use in plasma control system feedback, a reduced set of diagnostics is used which generally includes only magnetic probes and the motional stark effect (MSE) measurement of the plasma current profile. During disruptions, most of the other diagnostics used to constrain the equilibrium (including MSE) fail due to extreme conditions, so EFIT falls back on the magnetic probes and the system of equations it solves for becomes under-constrained so solutions become non-unique. Despite falling back on the magnetic probes, EFIT eventually fails towards the end of the TQ, after which it can no longer produce reliable solutions so other techniques are necessary.

3.9.2 JFIT

Another code which can reconstruct the flux function using only magnetic data is called JFIT [68]. JFIT solves for a current distribution in blocks of positively constrained uniform current density on a coarse grid regularized by singular value decomposition. The flux surface solutions obtained by JFIT are not constrained to Grad-Shafranov equilibria, because this equilibrium may not be appropriate for circumstances such as disruptions. In exchange for this physical constraint the code robustly produces solutions in almost any situation where enough plasma current exists to excite magnetic diagnostics. JFIT is hence generally used during plasma startup and shutdown studies, including disruption studies, due to this robustness.

The JFIT code has been briefly described previously in a publication by Humphreys et. al. [68]. It is based on principles similar to a filament fitting code (MFIT) which has also been previously described [158]. For the purposes of

clarifying the limits of analysis presented in section 6.3.3, this section describes the code in further detail.

In a sentence, JFIT finds a solution to magnetic measurements using a least squares technique with singular value decomosition regularization of current distributed on a coarse grid of arbitrarily shaped toroidal loops covering the vacuum region. The measurements consist of flux loops, magnetic probes (Mirnov coils), and Rogowski loops, [156] the geometries of which are shown in figure 3.21, along with an example coarse current grid.

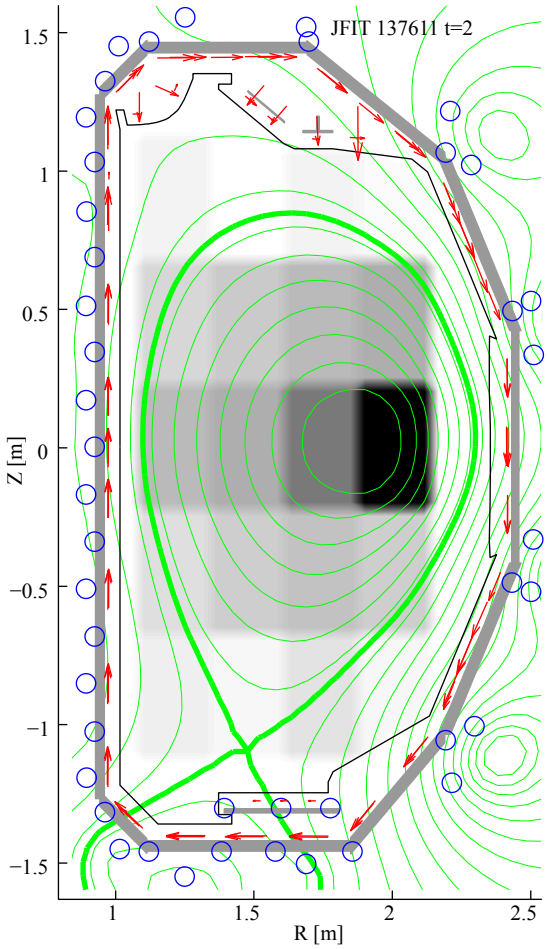

Figure 3.21: Geometry of magnetic diagnostics and coarse current grid used by JFIT. Flux loops are shown as blue circles, Mirnov coil magnetic probes are shown as red arrows in the direction of probe orientation, and the external Rogowski coil encloses the vacuum vessel shown in grey.

An element of constant current density j_i distributed in an area A_i containing total current $J_i = j_i A_i$ will result in a known measurement of flux enclosed by flux loops f_j, magnetic field $B_p \cdot \hat{b}_j$ along magnetic probes b_j, and current I enclosed by Rogowski coils R_j respectively:

$$\begin{aligned} f_j &= \int_{A_j} \left(\frac{1}{4\pi} \int_{V_p} \frac{\boldsymbol{j}(\boldsymbol{r_p}) \times (\boldsymbol{r} - \boldsymbol{r_p})}{|\boldsymbol{r} - \boldsymbol{r_p}|^3} d\boldsymbol{r_p} \right) \cdot \hat{\boldsymbol{z}} dA \\ &= M_{ij} J_i \qquad (3.5) \\ b_j &= \hat{\boldsymbol{b}}_j \cdot \boldsymbol{B_p} = \hat{\boldsymbol{b}}_j \cdot \frac{1}{4\pi} \int_{V_p} \frac{\boldsymbol{j}(\boldsymbol{r_p}) \times (\boldsymbol{r} - \boldsymbol{r_p})}{|\boldsymbol{r} - \boldsymbol{r_p}|^3} d\boldsymbol{r_p} \\ &= g_{ij} J_i \qquad (3.6) \\ R_{j,in} &= \sum_i J_i = I_p \qquad (3.7) \end{aligned}$$

where M_{ij} and g_{ij} are the mutual inductance and Green's function as discussed in section 6.3.1. In addition to the pseudo-Rogowski coil composed of magnetic probes mounted inside the vacuum vessel, another coil is mounted outside the vessel and hence measures the sum of both total plasma current and total vessel current:

$$R_{j,out} = I_p + I_v \qquad (3.8)$$

This system of measurements can be cast as a linear matrix problem, and then easily solved using least squares techniques:

$$\begin{bmatrix} M_{lc} & M_{lv} & M_{lp} \\ g_c & g_v & g_p \\ 1_c & 0 & 0 \\ 0 & 0 & 1_p \\ 0 & 1_v & 1_p \end{bmatrix} \times \begin{bmatrix} J_c \\ J_v \\ J_p \end{bmatrix} = \begin{bmatrix} f_j \\ b_j \\ J_c \\ R_{j,in} \\ R_{j,out} \end{bmatrix} \qquad (3.9)$$

As a result of non-uniqueness of the current density solutions and our somewhat arbitrary (and non-physical) choice of SVD for regularization, the current profile solved by JFIT can be non-physical. Despite this non-physicality, the reconstructed poloidal flux is surprisingly similar between the EFIT and JFIT codes,

suggesting that non-uniqueness is a greater problem for the current density than for the poloidal flux. The range of quantities which can be validly inferred using only magnetic diagnostics is limited [140], and some quantities (eg the loop voltage) can be inferred only by assuming certain aspects of the solution.

This chapter contains material published in Review of Scientific Instruments in 2010 [79]:

> A. N. James, E. M. Hollmann, and G. R. Tynan. "Spatially distributed scintillator arrays for diagnosing runaway electron transport and energy behavior in tokamaks", Rev. Sci. Instrum. 81, 10E306 (2010)

The dissertation author was the primary investigator and author of this paper.

Chapter 4

Hard x-ray emission from runaway electrons in DIII-D

In this chapter, experimental results from a new hard x-ray (HXR) sensing BGO scintillator array [79] and corresponding analysis exploring RE in shutdowns using argon killer pellets are discussed. The chapter is arranged as follows. Section 4.1 describes the experimental findings most directly apparent from the data. In section 4.2, experimental findings are explored further through discussion of limiting quantities, simulations, and other related analysis. A "prompt loss" phase is identified when hard x-rays from multi-MeV ($1 - 3MeV$) RE are first observed in the time between the TQ and CQ. The prompt hard x-ray emission arrives shortly ($< 0.5ms$) after argon pellet injection, so REs are clearly experiencing large loop voltages even before the global current decay begins, demonstrating that RE seed formation is not confined to the CQ phase. In diverted discharges, the prompt loss of REs is found to be localized to the divertor strike points, consistent with NIMROD modeling (discussed in section 4.2.5) which suggests loss due to magnetically stochastic regions from post-TQ MHD. In limited discharges, the prompt x-ray emission associated with RE deconfinement is reduced compared to the diverted configuration, also consistent with NIMROD modeling which indicates reduced post-TQ MHD in limited target plasmas. These prompt loss phenomena are further discussed in section 4.2.2. During the RE plateau after the CQ, a steady toroidally symmetric hard x-ray emission is observed which continues even after

the last closed flux surface separates from the wall. Also during the plateau in some shots, intermittent toroidally symmetric hard x-ray bursts coincident with bursts on magnetic probes suggest an unidentified instability. These plateau phenomena are discussed in section 4.2.3. All RE plateaus terminate abruptly with a clear toroidal peaking of hard x-ray emission. In some shots the final loss has a clear vertical displacement event (VDE) precursor, while in other shots there is no clear precursor and the plateau terminates on the center-post at the midplane. Termination phase phenomena are discussed in section 4.2.4.

4.1 Experimental findings

Figure 4.1 shows an example diverted discharge exhibiting a runaway plateau broken down chronologically from left to right into phases referenced throughout this paper: thermal quench and prompt generation, prompt loss, current quench and avalanche, runaway plateau, and final termination. Panels a-d illustrate long timescale quantities of the plateau, while panels e-g highlight observations of fast phenomena before the current quench, all of which are described below. Similarities and differences between shutdowns of the diverted and limited configurations will be discussed.

Once the current quench begins, the total measured plasma region current I_p decays, producing a loop voltage that induces wall currents I_w and accelerates runaway electron current I_r, examples of which are shown in figure 4.1a. When a runaway plateau does not occur, the thermal plasma current follows an exponential decay $I_{L/R} = I_0 exp(-t/\tau_{CQ})$ from the point of fastest current decay, where $\tau_{CQ} = L/R$ corresponds to the plasma inductive timescale. Following prior calculations [35], RE current I_r is calculated by subtracting this model for decaying thermal current from the total measured current. Previous work [145] suggests that this RE plateau current is formed by an avalanche phenomena that amplifies a small pre-existing RE seed current.

Figure 4.1b shows the average RE energy inferred from a set of scintillators equipped with incrementally thicker lead shielding, sensitive to RE energies in the

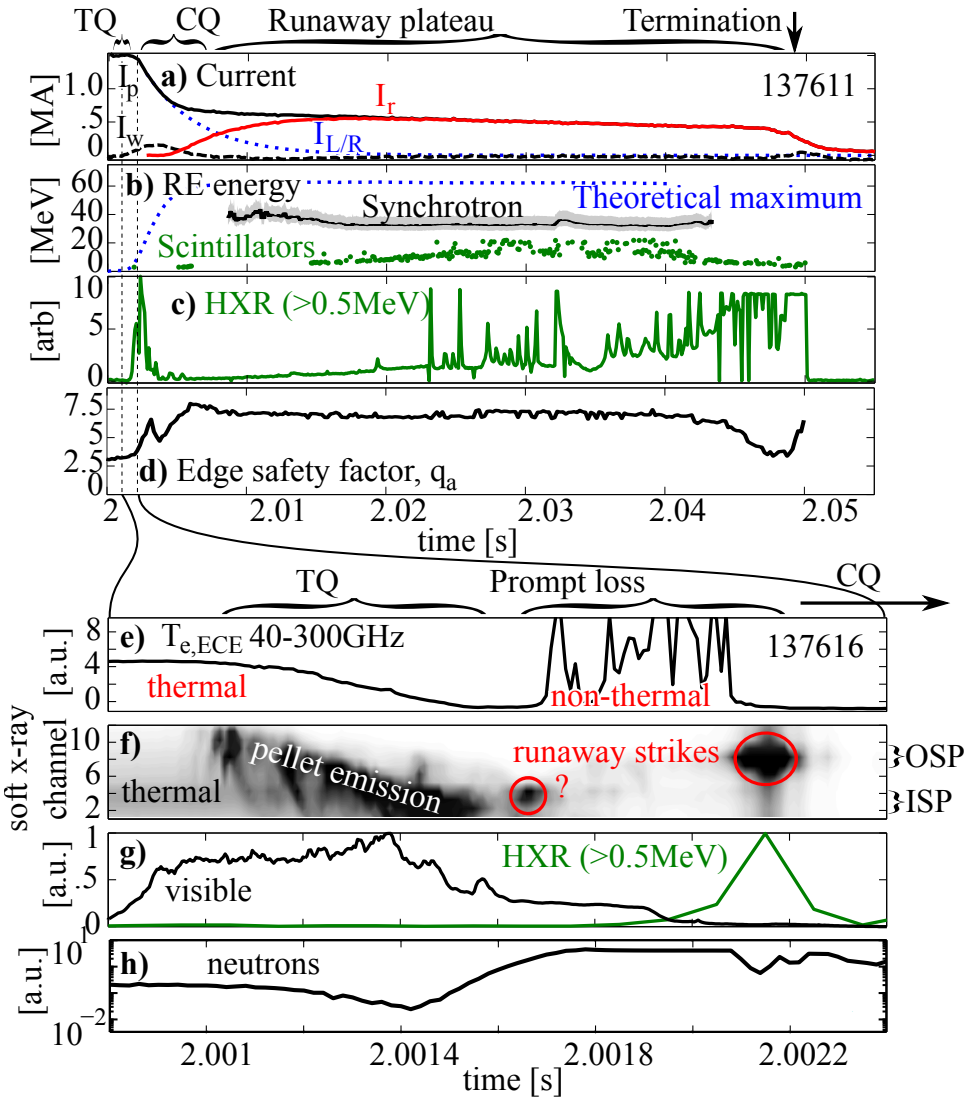

Figure 4.1: Overview data of typical observations during the thermal quench, current quench and runaway plateau phases including a) total measured plasma region current I_p, wall current I_w, inductive decay model current $I_{L/R}$, and plateau phase runaway current I_r, b) runaway energy measured with scintillators, visible synchrotron emission [83], and a theoretical maximum, c) hard x-ray emission measured by a mid-plane detector at 90 degrees toroidal, and d) the edge safety factor calculated [40] by JFIT. An expansion of the thermal quench is shown to detail fast response of the following: e) broadband cyclotron emission, f) soft x-ray emission with inner and outer divertor strike points labeled (ISP and OSP respectively), g) visible line radiation from the pellet and hard x-ray emission, and signals on a neutron counting plastic scintillator. Temporal phases including the thermal quench and current quench are indicated along the top of each section.

range $0.5MeV \lesssim W_r \lesssim 20MeV$ [79], and the RE energy inferred from visible synchrotron emission observed on a fast camera, sensitive only to runaways with energy sufficient to generate visible synchrotron emission $W_r \gtrsim 30MeV$ [83]. These energies are both below the theoretical maximum runaway energy which will be discussed in section 4.2.6.

Figure 4.1c shows a time history of the hard x-ray ($W_\gamma \gtrsim 0.5MeV$) intensity recorded in a scintillator shielded with $4mm$ of lead foil located near the mid-plane.The detector shows brief hard x-ray emission before and during the CQ (referred to as the 'prompt loss'), followed by a lower intensity continuous emission with intermittent bursts (referred to as the 'RE plateau'), and ends with another brief intense emission during the plateau termination (referred to as 'final loss'). These three phases will be described further in the discussion.

Figure 4.1d shows the edge safety factor, which features a drop that occurs over the last few milliseconds before final termination. The edge safety factor is calculated from the integral $q_e = \oint d\theta r B_T / R B_p$ [40] along the boundary from JFIT reconstructions [68].

High time-resolution observations of RE generation and de-confinement between the TQ and CQ are shown in figures 4.1e-g. During this period, total plasma current remains roughly constant (ie $dI/dt = d/dt(\int j(\psi) d\psi) \sim 0$) while it re-organizes (ie $d/dt(j(\psi)) \neq 0$) for a duration of about $1ms$ from the beginning of the TQ.

Initial signals until $2.001s$ on a broadband microwave radiometer shown in figure 4.1e correspond to thermal electron cyclotron radiation which decays during $2.001 - 2.0016s$ as the pellet radiates away thermal energy. Bursts of microwave emission during $2.0017 - 2.0021s$ occur after the TQ which could be either associated with broadband emission from non-thermal electrons [93], from x-band emission associated with filamentation of relativistic electron beams propagating in dense plasmas [89], or some other emission process. The broadband radiometer is used because it includes third harmonic thermal ECE which is robust against cutoff due to re-absorption by the plasma, a topic discussed further in section 4.2.1.

Observations from soft x-ray sensing photodiode arrays which view chords

through the plasma core and divertor are shown in figure 4.1f. These arrays observe emission associated with bremsstrahlung from the hot core thermal emission until $2.001s$, followed by line radiation as the pellet streaks through and cools the plasma during $2.001 - 2.0016s$. Brief emission from isolated chords occurs later at $2.00165s$ and $2.00215s$, and is associated with bremsstrahlung from RE impact at the divertor inner and outer strike points, referred to as 'prompt loss'. The soft x-ray data is ambiguous about where emission originates along the chord view, but the prompt loss emission always occurs brightest in chords viewing the divertor strike points. Also, the observed hard x-ray intensity at $2.00125s$ coincident with the outer strike point soft x-ray emission could only occur from RE striking a thick target, as discussed in appendix 4.2.7.

In figure 4.1g, a photo-diode sensitive to visible wavelengths of light from the plasma observes strong emission from argon pellet interaction with the cool boundary plasma beginning at $2.0005s$, before the pellet reaches the core and line radiation is first seen by the soft x-ray array. Also shown in figure 4.1g is a signal from a hard x-ray scintillator located outside the vessel near the divertor which observes emission coincident with the peak in outer strike point soft x-ray emission at roughly $2.00215s$, as noted above. No hard x-ray burst occurs coincident with the inner strike point soft x-ray emission. The time of the peak hard x-ray intensity measured by detectors below the divertor and peak outer strike point soft x-ray intensity are shown to coincide in figure 4.2, which is consistent with the broad energy spectrum of bremsstrahlung emission from RE striking the divertor [79]. Of the thirty successful shutdowns of the diverted configuration, this transiently peaked hard x-ray emission coincides with outer strike point soft x-ray emission in twenty-three shots (including all shots with RE plateaus), while no hard x-ray emission occurred in the remaining seven shutdowns. The energy sensing scintillators located at the mid-plane on opposite sides of the vessel infer an average RE kinetic energy of $W_k = 1 - 3MeV$ during these prompt loss events, which occur prior to the onset of the CQ phase.

Figure 4.1h shows signals from a neutron counting scintillator, which is also sensitive to hard x-rays. Observed hard x-rays must have an energy in the range of

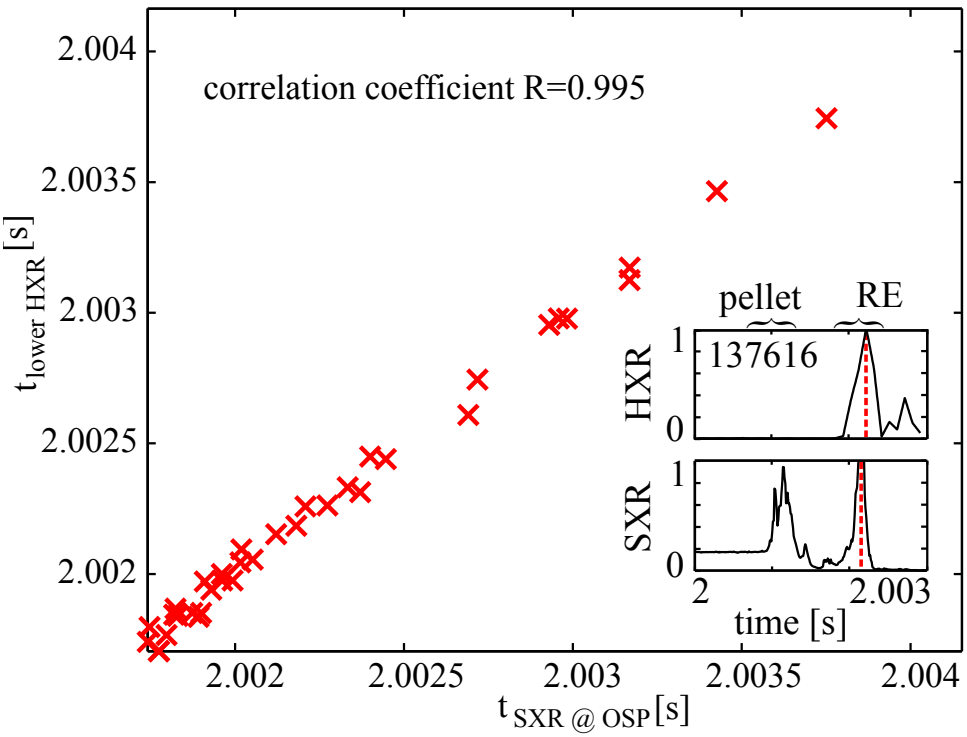

Figure 4.2: Correlation of times recorded for prompt hard x-ray bursts in detectors on the bottom of the machine and soft x-ray bursts in chords viewing the outer strike point. The inlay shows hard x-ray (HXR) and soft x-ray (SXR) time traces during prompt loss for one example shot.

$\gtrsim 0.5MeV$ to penetrate the vacuum vessel. During the TQ, the neutron production rate drops on the thermal quench timescale, roughly following the broadband electron cyclotron emission. Compared with the lower-gain photodiodes used on the BGO scintillators, the high gain photomultiplier on this scintillator can also see much lower intensity hard x-ray emission. As a result of this higher sensitivity, this signal rises beginning at $2.0014s$ before the TQ has completed, suggesting that some small amount of high energy RE may already exist even before the plasma has cooled completely, though this is not seen on any other diagnostics. In some shots, the signal abruptly drops after the prompt burst is completed and an exponential increase of the signal is observed for a few milliseconds until the detector saturates again. This suggests an exponential increase of RE-induced hard x-ray emission consistent with avalanche multiplication of the RE population.

4.2 Discussion and Analysis

4.2.1 Limitations of thermal quench measurements

As discussed previously in section 3.7, ECE cutoff occurs when the electron density crosses a threshold value. The line-averaged electron density can be measured by a two-color interferometer, but there are some complications during disruptions which must be corrected including: variation of the effective path length as the plasma moves, and correction of fringe skips when the lasers refract too much in the strong density gradients. Dividing the sum of line integrated density along the four interferometer paths by the total path length inside the last closed flux surface then provides a density measurement that is more nearly a volume averaged quantity: $n_{avg} = \Sigma n_e dl / \Sigma dl$. In the diverted configuration, the line averaged density measured this way is near the cutoff value before shutdown, and crosses the cutoff value roughly $400\mu s$ after the TQ begins. In the limited configuration, the initial line averaged density is lower, and crosses the cutoff value roughly $1ms$ after the TQ begins. Data illustrating this cutoff are shown in figure 4.3.

As seen in figure 4.3c, the second harmonic ECE is abruptly cutoff at $2.0007s$, which occurs roughly $300\mu s$ before the line average density exceeds the right handed cutoff, suggesting that a localized peaking of the density occurs during the TQ. No cutoff is apparent in limited shutdowns, where a cooling wave is seen advancing on the TQ timescale, though similar localized peaking of density is likely. Again, in both plasma configurations, the plasma appears to remain mostly transparent to third harmonic ECE which is viewed by the broadband ECE diagnostic. The neutron production rate is also roughly proportional to temperature in a hot plasma, and the TQ timescale inferred from the drop in neutron production roughly matches that inferred from the broadband ECE diagnostic.

It is important to remember that if the local density anywhere exceeds the cutoff threshold, partial cutoff will occur, resulting in an apparent local cooling rate which is faster than reality. For example, a high density annulus surrounding a hot core could emit much less cyclotron radiation than an equivalently hot plasma

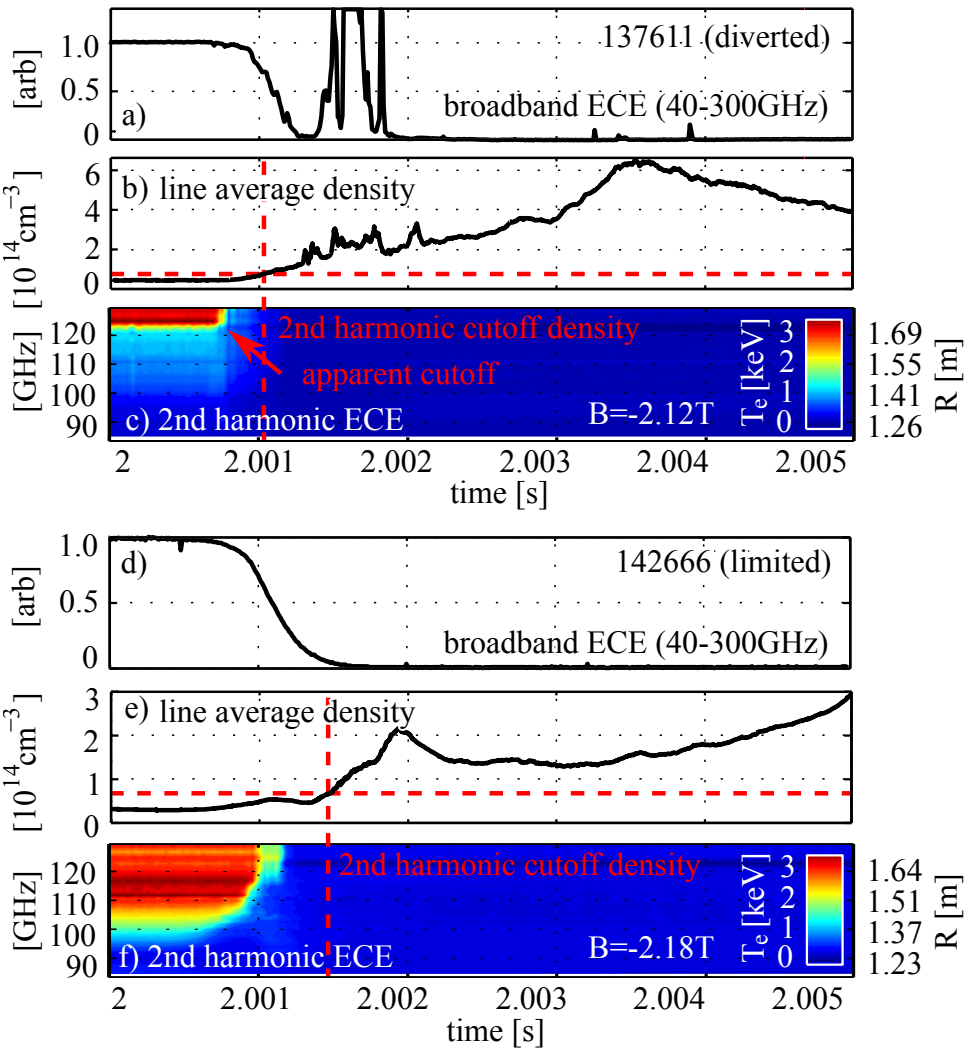

Figure 4.3: Total line averaged density shown with both broadband and channelized ECE systems for a-c) diverted and d-f) limited configurations.

with no high density annulus. Our fast interferometer based density measurements are not spatially resolved so such a scenario cannot be ruled out. Despite these considerations, the ECE and neutron production data are consistent with a rapid ($\leq 500\mu s$) collapse of the plasma electron temperature due to the injected argon impurities.

4.2.2 Prompt-loss phenomena

The above evidence of RE generation occurring *before* the CQ (hence referred to as 'prompt' runaway generation) implies that some voltage source must exist before the CQ which then accelerates REs up to the apparent MeV energies. This section focuses primarily on x-ray emission during the prompt-loss phase, but the range of possible accelerating voltages is further discussed in section 4.2.6.

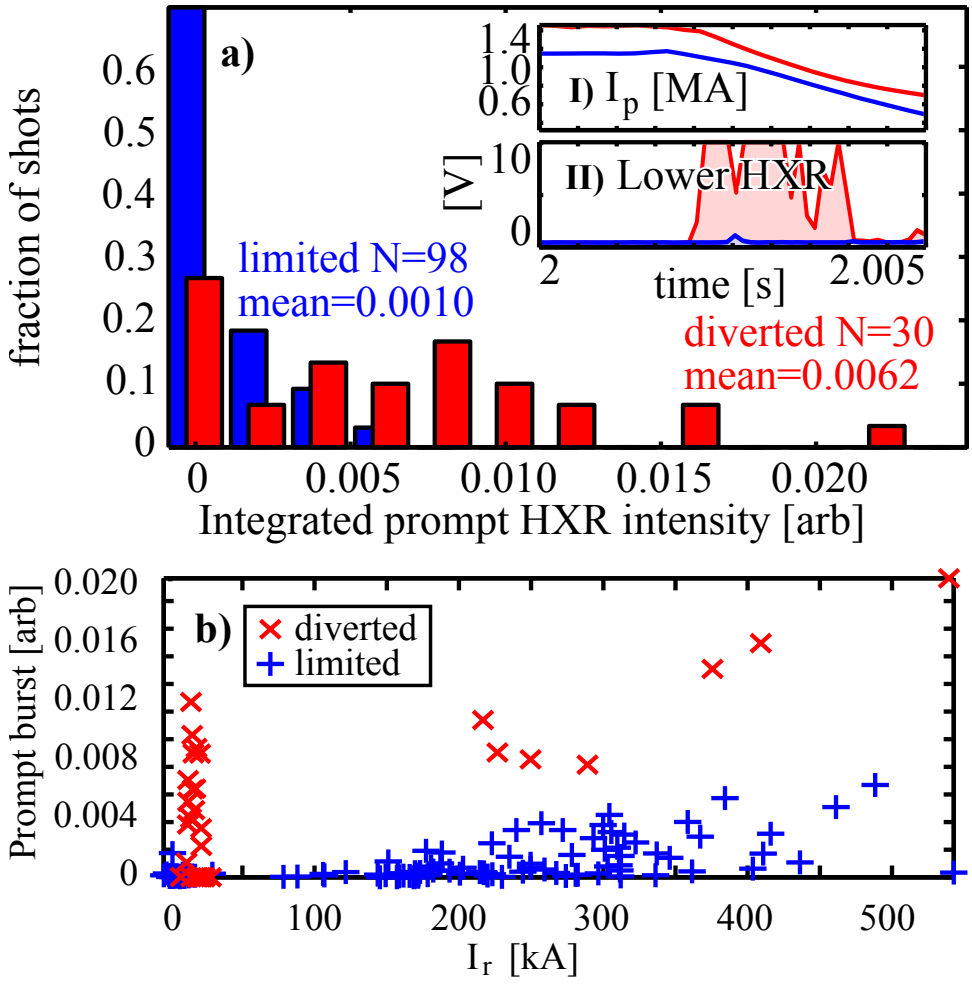

Figure 4.4: a) A histogram illustrating that the average intensity of the time integrated prompt loss hard x-ray burst is greater in diverted experiments compared to limited experiments. An inlay shows the respective time histories of I) current and II) hard x-ray emission in lower detectors in two example discharges. Also shown are b) the time integrated prompt bursts plotted against the RE plateau current magnitude.

When RE seed current is de-confined and strikes the vessel walls during the prompt loss, it generates bremsstrahlung x-rays. Since the de-confined runaway seed current is linearly proportional to x-ray emission [104] as discussed in section 4.2.7, the x-ray emission integrated over the prompt loss phase can be used as a qualitative proxy for the amount of de-confined REs during the prompt loss phase. In figure 4.4a, a histogram of the integrated prompt hard x-ray burst from REs as observed by the lower detectors is shown for both the diverted and limited configurations separately. This x-ray emission is nearly an order of magnitude larger on average in the diverted configuration than in the limited configuration, suggesting that a greater quantity of RE are lost during prompt loss in diverted shutdowns than in limited shutdowns. In the diverted configuration, substantial prompt loss bursts are seen even when no RE plateau occurs, as shown in figure 4.4b; for diverted discharges where a RE plateau does occur, the prompt loss intensity is roughly proportional to the plateau RE current. In the limited discharge configuration by comparison, the prompt loss burst is often small even when a large RE plateau occurs, consistent with improved RE confinement during the prompt loss phase. It is important to note that the present experiments do not separate the effects of elongation and the location or existence of a divertor x-point or limiter contact point on these transport phenomena, any of which on their own might cause the observed changes in confinement. Differences in confinement between the two configurations are further discussed in section 4.2.5.

4.2.3 Plateau phenomena

Beginning with the RE plateau, there is a steady x-ray emission which is observed on both the external hard x-ray scintillators, and all soft x-ray arrays. This emission is believed to result from a combination of bremsstrahlung from RE scattering off of in-plasma impurities and a small number of RE steadily striking the wall due to a scrapeoff on the limiter or a slow diffusive transport of RE out to the wall. Bremsstrahlung from both in-plasma impurities and wall losses appear to have comparable intensity, as discussed in appendix 4.2.7. This long duration steady hard x-ray emission is toroidally symmetric and illuminates only

the mid-plane detectors, as shown in figure 4.5b. The illumination of only mid-plane detectors is consistent with forward beaming of x-ray emission at a narrow angle of $1/\gamma \sim 10^{\circ}$ for $W_r = 10MeV$ RE moving primarily in the toroidal direction, since mid-plane detectors lie at roughly zero angle with respect to the toroidal direction but upper and lower detectors would lie at an angle of roughly 90 degrees.

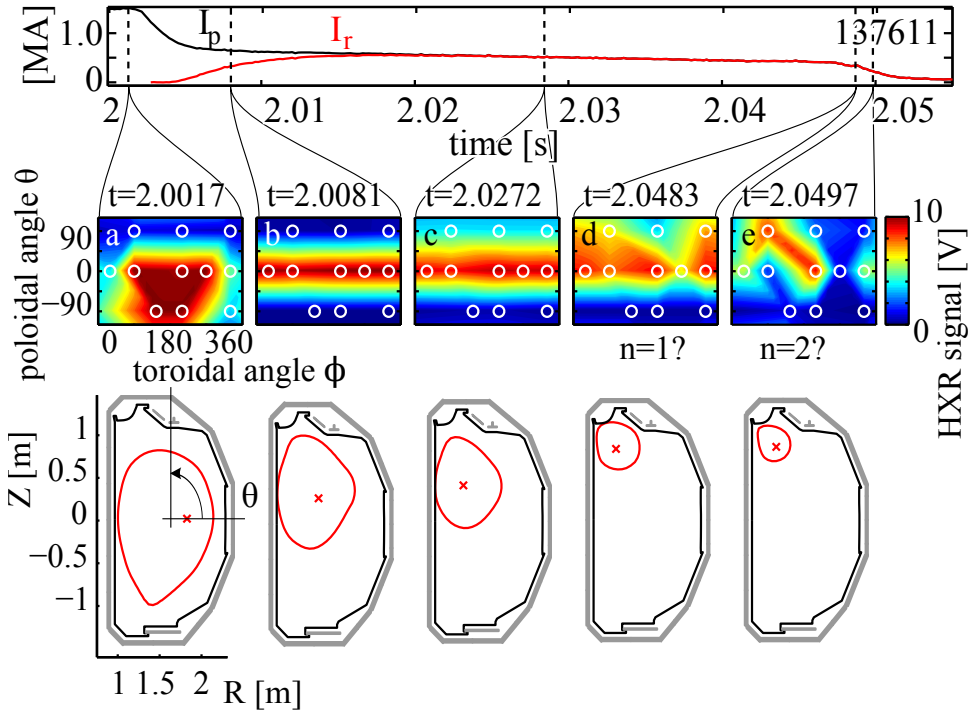

Figure 4.5: Spatial hard x-ray emission profiles with detector locations circled and JFIT magnetic reconstructions of last closed flux surface location and shape. Panels are shown for the prompt loss phase (a), the steady and bursty emission during the plateau phase (b & c), and the kink-like termination phase with apparent toroidal mode numbers labeled (d & e). Amplifiers are saturated at 10V.

Efforts in some shots to move the RE current away from the center stack limiting point resulted in no abrupt decrease of hard x-ray emission when the last closed flux surface (LCFS) separated from the limiter as shown in figure 4.6. After the Shafranov shift vanishes following the TQ, every RE plateau contracts in major radius as seen during the time period $2 - 2.015s$ and becomes limited on the center stack near the midplane. Efforts to move RE away from the center stack actually begin moving the current centroid out again around $2.03s$, and

the inner gap between the LCFS and center stack becomes finite at around $2.1s$. The absence of a drop in hard x-ray emission when the LCFS separates from the wall suggests either that scrapeoff of RE at the limiting point does not produce substantial hard x-ray emission at any of the observation points, or that there may be some inaccuracy of the LCFS location. As discussed in section 4.2.4, there are indications that RE exist outside of the LCFS. If the LCFS position can be believed, then the hard x-ray emission remaining after the inner gap becomes finite must not be sensitive to the LCFS location, suggesting that hard x-ray emission occurs due to some process other than RE scrapeoff at the limiting point. In particular, hard x-rays may still result from a combination of bremsstrahlung from gradual loss (ie diffusion or other transport) of RE to the wall and RE scattering off of argon impurities within the plasma, as discussed in appendix 4.2.7.

Gamma spectroscopy was performed after these experiments on the three outer midplane graphite limiters at toroidal locations of 95, 230, and 310 degrees [160]. This analysis identified the presence of beryllium-7 in the limiter tiles, similar to analysis performed at the C-Mod tokamak [19]. Beryllium-7 can be produced through photoactivation of carbon-12 by photons with energy of at least $26MeV$, which would be generated by bremsstrahlung from RE impacting the limiters. The finding that beryllium-7 is only found near the outer midplane limiters (circled in blue in figure 4.6) and not at other locations, suggests that REs primarily impact the outer midplane limiters, consistent with drift orbit losses [34].

At least one substantial hard x-ray burst occurs during most runaway plateaus, sometimes several are observed, as shown in figure 4.7b. These x-ray bursts are toroidally symmetric as shown in unsaturated upper detectors in figure 4.5c, and are believed to result from a small amount of RE being de-confined and striking the wall. Since no drop in I_r is observed coincident with the bursts, the amount of lost RE current must be below the $\sim 1kA$ noise level of the current measurement. Poloidally localized spikes of change in the poloidal magnetic field occur simultaneous with the larger hard x-ray bursts, as shown in figure 4.7dii. Similar x-ray and magnetic bursts were seen in prior JT-60U experiments [172, 159]. The bursts likely occur as a result of some yet unidentified instability of the RE equi-

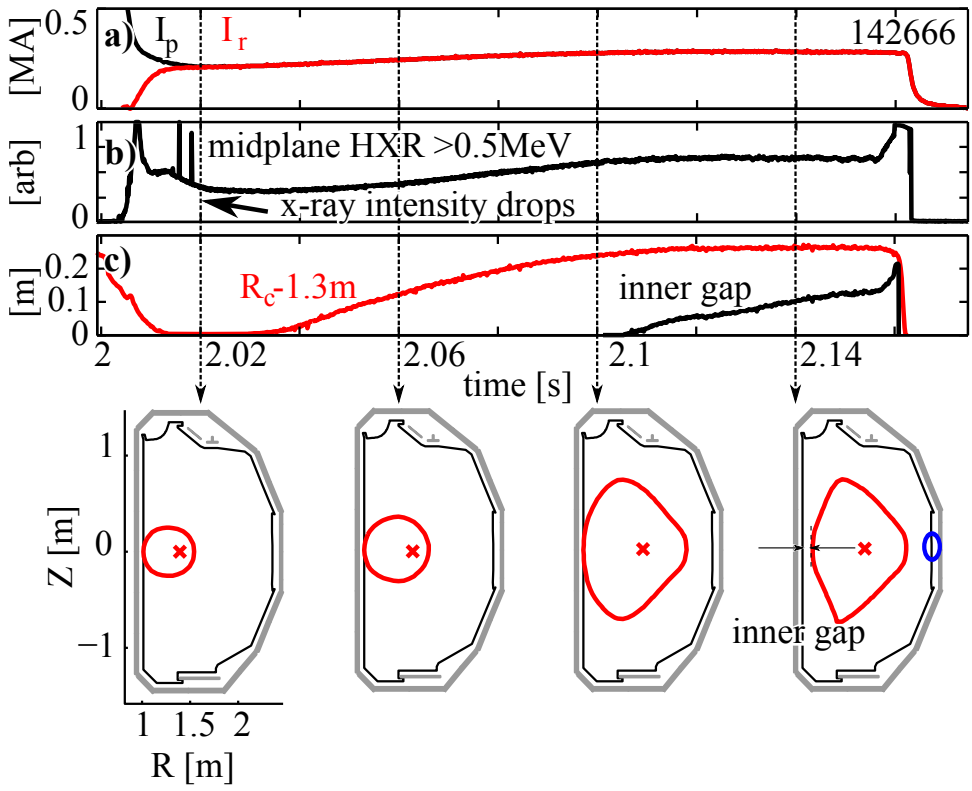

Figure 4.6: Plasma motion in a shot where a) RE current was moved off of the limiter, showing b) hard x-ray emission. The current centroid major radius R_c is shown with the gap size between the LCFS and limiter in (c). In the cross-section plots, the current centroid is marked by an 'X'. The blue circle in the bottom right panel marks the location of peak limiter activation.

librium; several possible non-terminating instability mechanisms which can result in rapid loss of RE are examined and ruled out below.

These runaway plateau discharges appear to be stable against filamentation. In a relativistic ($\beta = v/c \sim 1$) electron beam with small return current I_{return} and hence incomplete current neutralization $f_M = I_{return}/I_r \ll 1$, and low density n_r propagating in plasma of relatively high density such that $n_e \gg n_r$, filamentation instability occurs when [28]

$$\frac{\omega_{pb}^2}{\omega_{cb}^2} \Big/ \left(1 + 2\frac{\omega_{pb}^2}{\omega_{cb}^2}(1 - f_M)\right) > 1 \tag{4.1}$$

where the beam plasma frequency is $\omega_{pb} = (e^2 n_b/\epsilon_0 m_e \gamma)^{1/2}$ and the beam cyclotron frequency is $\omega_{cb} = eB_0/m_e\gamma$. The return current can be any neutralizing current

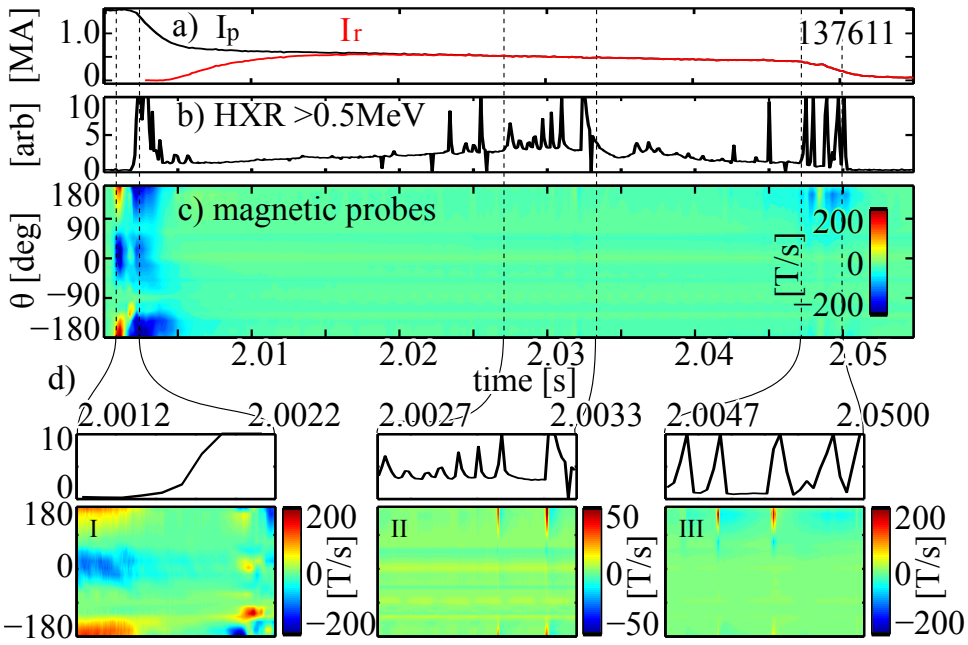

Figure 4.7: Signals on differential magnetic probes which occur coincident with hard x-ray bursts at different phases. Expanded views of the I) prompt loss phase, II) plateau phase, and III) final termination phase are also shown.

flowing against the main RE current channel. For a top-hat (step function) profile runaway beam, the runaway density n_r or runaway current density j_r as a function of runaway current I_r and minor radius a is $n_r = j_r/ec = I_r/ec\pi a^2 = 3.3 \times 10^{11} cm^{-3}(I_r/500kA)(10cm/a)^2$. The ratio of the beam plasma and beam cyclotron frequency then becomes

$$\begin{aligned} \frac{\omega_{pb}}{\omega_{cb}} &= \sqrt{\frac{I_r W_r}{\epsilon_0 e c^3 \pi a^2 B_0^2}} \\ &= 0.41 \sqrt{\frac{I_r}{500kA}\frac{W_r}{10MeV}}\frac{10cm}{a}\frac{2T}{B_0} \end{aligned} \tag{4.2}$$

where typical runaway plateau phase values of have been substituted as shown above. Hence even a current neutralized top-hat runaway beam should be marginally stable against filamentation. While peaking of the current profile (i.e. increase of ℓ_i) associated with ramp-down [74] or runaway energies higher than assumed could slightly destabilize filamentation, the low degree of current neutralization f_M in real RE beams strongly stabilizes filamentation.

RE plateaus are stable against growth of magneto-sonic whistler waves [42] as long as $n_r/n_e < Z^2 B_T/20T_{ev}^{3/2}$. In the post-TQ RE plateau where $Z_{eff} \sim 1$, $B = 2T$, $T \sim 1.5eV$, and $n_e \sim 5 \times 10^{14} cm^{-3}$, these waves are then stable because $n_r/n_e \sim 0.0007 < Z^2 B_T/20T_{ev}^{3/2} = 0.05$.

RE plateaus are also stable against the fan instability whenever the ratio of the Dreicer field to the toroidal field E_D/E is large, as during RE plateaus. The low temperature during RE plateau makes the condition for the fan instability [130]: $E_D/4E + \sqrt{(Z_{eff}+1)E_D/E} \leq ln\Lambda$ unsatisfiable.

Further investigation of MHD stability [39] of the RE equilibrium [170] is necessary to identify the causative instability associated with the burst of HXR emission.

Scintillation bursts coincident with these hard x-ray bursts occur in the fiber bundle of a fast camera sensitive to visible light. This camera also observes internal instabilities appearing as rapid rearrangement of RE synchrotron emission inside the last closed flux surface; however these internal dynamics do not appear to coincide with hard x-ray scintillations. Taken together, these observations suggest that these plateau phase hard x-ray bursts may result from instabilities localized to the edge region.

An important parameter for future machines is the degree of localization for energy deposited by REs onto vessel surfaces. We have quantified this issue by defining a toroidal peaking factor (TPF) for the mid-plane toroidal array of scintillators, which is defined as the ratio of the maximum hard x-ray signal P_{hxr} to the mean value $\bar{P}_{hxr}$: $TPF = max(P_{hxr})/\bar{P}_{hxr}$. Due to high intensity hard x-ray emission during the plateau phase, only a reduced set of three scintillators in the midplane toroidal array equipped with attenuating neutral density filters was unsaturated in most discharges. This reduced set of detectors reveals that hard x-ray emission during the plateau phase is typically quite toroidally symmetric during the brief bursts discussed above and during continuous emission, except for some oscillations, as shown in figures 4.5c and 4.8. Occasionally, out of phase fluctuations are observed, as seen in figure 4.8c until $2.015s$, which suggest the

presence of a slowly rotating toroidally asymmetric mode during the growth of the RE current, consistent with an early n=1 mode discussed elsewhere [71]. In phase fluctuations sometimes occur up to $20ms$ before termination, suggesting the presence of a toroidally symmetric mode, as shown beginning around $2.1s$ in figure 4.8b. These observations of hard x-ray toroidal symmetry and asymmetry during the plateau phase are shown in figure 4.8c.

In several shots, the suppression of existing RE current by additional impurity injection was studied [63]. This impurity injection resulted in an increase of plateau phase toroidal peaking to roughly two for a brief period after the impurity injection, which caused the six anomalously high plateau TPFs in figure 4.8d. After this brief transient increase, hard x-ray emission decreased by more than a factor of ten and toroidal symmetry resumed.

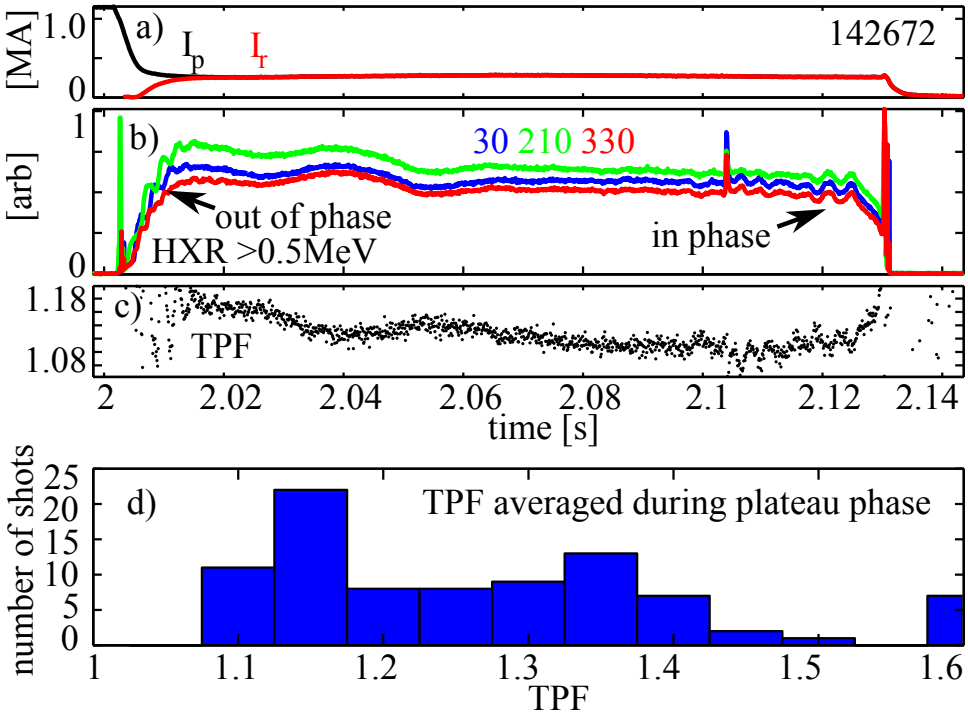

Figure 4.8: a) Total measured current, b) hard x-ray signals on midplane scintillators at three toroidal locations, c) the toroidal peaking factor for these scintillators, and d) a histogram of the plateau phase toroidal peaking factor for all plateaus.

4.2.4 Termination phenomena

After remaining confined for up to several hundred milliseconds, all RE plateaus terminate abruptly due to either vertical instability or another instability, similar to reported termination behavior in JT-60U [171, 159]. A histogram of the apparent final plateau instability types is shown in figure 4.9, with columns for each of four termination modes: downward vertical displacement event (VDE), centered radial instability, upward VDE, and control system error which resulted in slow vertical drift. The RE plateau VDE's occur on a timescale similar to that predicted previously [142]: $\tau_{VDE} = \tau_{CQ}\tau_w/(\tau_{CQ} + \tau_w) \sim 1.3ms$ where in DIII-D $\tau_{CQ} \sim 3.7ms$ and the wall time is $\tau_w \sim 2ms$ calculated as the inductive time of the mode driven in the wall by changes in current at the vessel center. All diverted configuration experiments and some early limited configuration experiments drifted slowly upwards due to issues with the control system which were solved before the majority of limited configuration experiments were performed [25, 67].

Many plateaus terminate immediately following a considerable drop in the edge safety factor, as shown in figure 4.1d, suggesting that the corresponding destabilization of various kink instabilities may ultimately cause the termination. The edge safety factor is calculated from reconstructions constrained only by external magnetic diagnostics, which other authors have reported [140] to be a valid inference. There is evidence that a substantial number of RE are present roughly $16cm$ outside of the LCFS [80], while synchrotron emission from the highest energy RE is only visible well inside of the LCFS. These observations suggest that while the LCFS remains a well defined magnetic surface, it may not define a good boundary for RE confinement as assumed for thermal plasmas and the edge safety factor may lose meaning in this case.

Toroidally asymmetric hard x-ray emission occurs during the final termination as shown in figure 4.5d and e. These toroidal asymmetries are consistent with the occurrence of kink modes being destabilized as q drops. With the poloidal arrangement of only three scintillation detectors, poloidal mode numbers are not resolvable, while the mid-plane toroidal arrangement of five detectors cannot resolve modes higher than n=2.

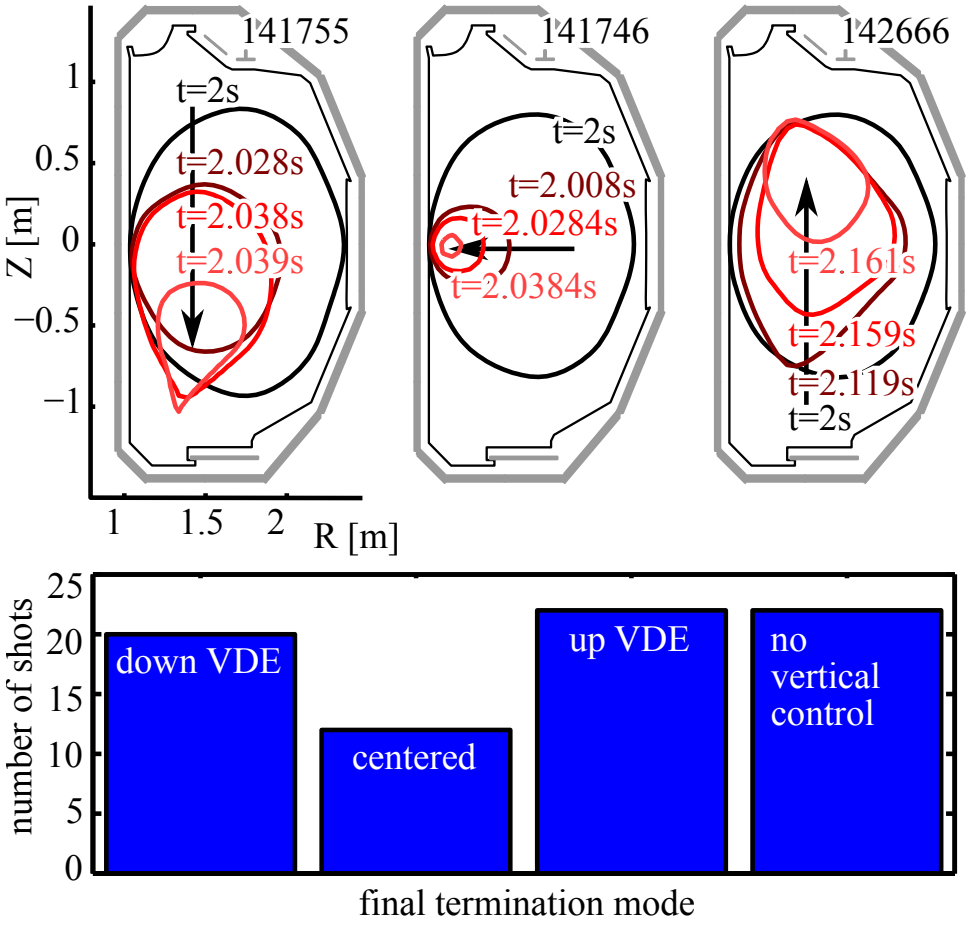

Figure 4.9: Final termination mode for RE plateaus.

The time integrated hard x-ray emission during the final termination is used to verify that hard x-ray intensity is proportional to the de-confined RE current. For this check, only shots which terminated at the top of the machine and only hard x-ray emission measured by the lower detectors are used to avoid detector saturation from the strong forward beaming of emitted x-rays. Hard x-ray signals selected and integrated in this way correlate roughly with I_r measured just before termination in both diverted and limited shutdowns as shown in figure 4.10, with correlation coefficients of $R = 0.87$ and $R = 0.83$ respectively.

For discharges with only a small amount of RE generated, a repeatable temporal sequence of hard x-ray signals during the final loss occurs in the midplane toroidal array of detectors. This sequence was observed in seventeen of twenty-five

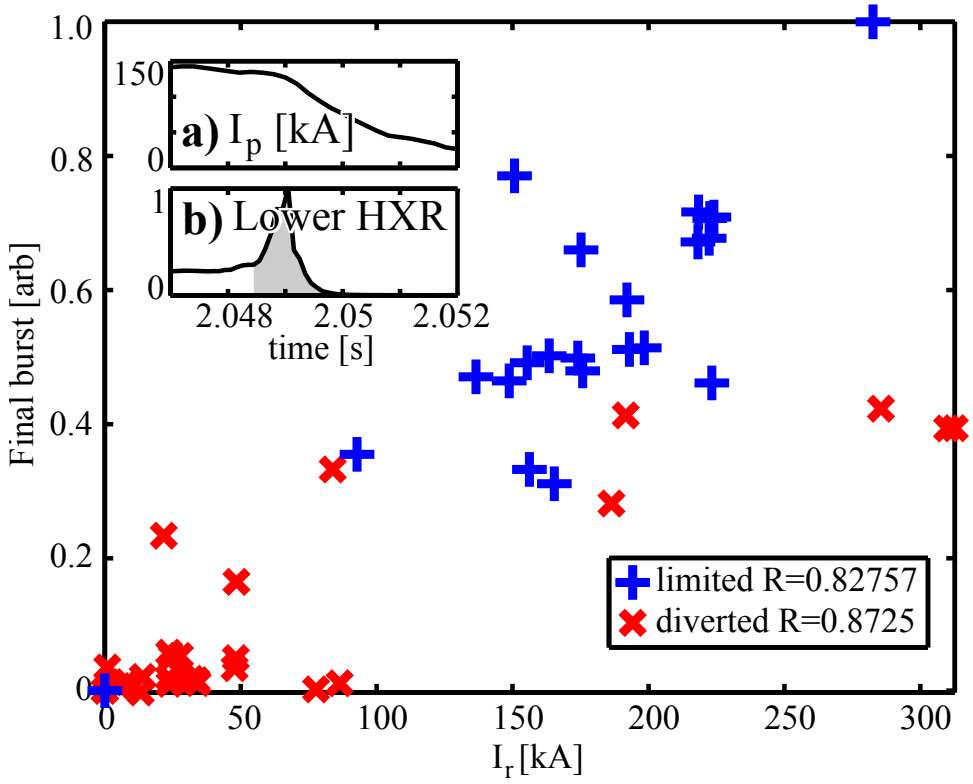

Figure 4.10: Integrated final hard x-ray bursts in lower detectors plotted against final measured RE current for terminations at the top of the vessel, as discussed in the text.

shutdowns before neutral density filters were installed to reduce detector saturation. In such shutdowns, a low intensity signal slowly increases for roughly $1ms$ on opposite sides of the machine (always detectors at 90 and 270 degrees), followed by $2-10ms$ of abrupt increase to intense hard x-ray emission which saturates the entire toroidal array, followed by roughly $0.5ms$ of low intensity decaying emission in only the detector located at 210 degrees. One example shot exhibiting this sequence is shown in figure 4.11.

The TPF and variability of location, duration, and intensity of hard x-ray emission during the final loss are all presented in histograms in figure 4.12.

To establish a TPF without saturated detectors during the final loss phase of plateau discharges, the TPF is calculated as described earlier, and is then averaged

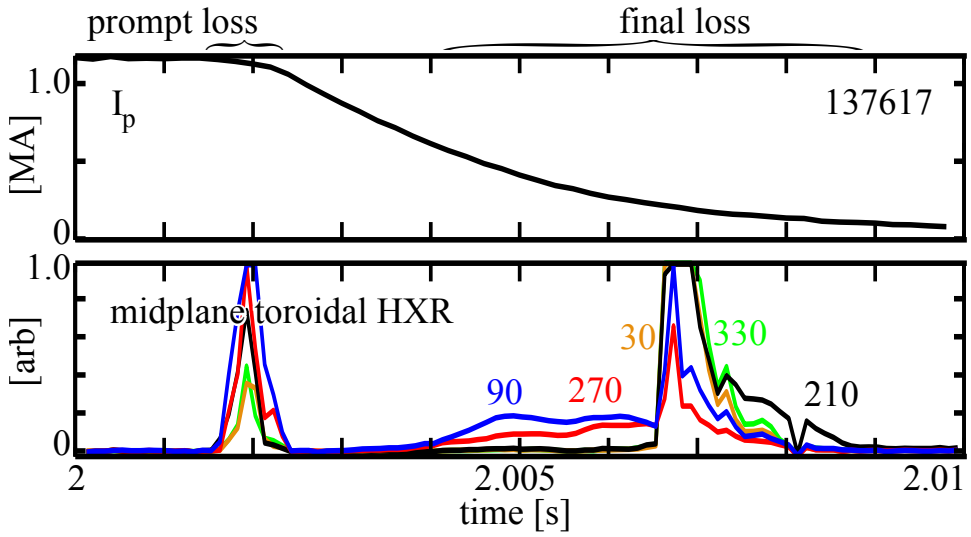

Figure 4.11: Midplane toroidal array of hard x-ray scintillators showing a consistent final loss sequence of toroidal asymmetry, with detector toroidal locations marked in degrees.

during periods of the termination phase hard x-ray emission when no detector in the array is saturated. The resulting TPF most often has a value of roughly two, though in some shots it can reach values of four, larger in either case than in the TPF during the plateau phase shown earlier in figure 4.8. While this hard x-ray TPF is the best measure available on DIII-D of localization of deposited RE energy, it is again important to recall that any x-ray scattering in the vessel walls can broaden the x-ray footprint so that even a point impact of runaways might produce a spatially broad excitation of x-ray detectors, and also that the toroidal arrangement of only five scintillators could entirely miss a narrow x-ray footprint. Thus, the peaking factor shown here represents a lower limit due to these effects, and RE energy deposition in DIII-D may actually be localized to several small strike points as occurs in other experiments [7, 117, 113].

The phase of the maximum observed x-ray intensity during the same period the TPF is calculated is roughly 120 degrees, with a small spread. This apparent existence of a persistent toroidal peaking location is consistent with infrared camera observations at JET [7], which reveal persistent localized RE strike points from shot to shot. The persistent peaking location may result from error fields which

could cause a repeatable mode locking location in the machine.

The time duration of final loss hard x-ray emission (shown in figure 4.12c) varied from $2ms - 14ms$ for VDEs, which is a much longer time period than the VDE timescale $\tau_{VDE} \sim 1.3ms$ discussed earlier. This suggests that even though the VDE occurs rapidly, hard x-ray emission persists because RE do not all immediately strike the vessel wall, or new RE may be generated by the rapid current drop at the end of plateau. By comparison, the duration of final loss x-ray emission in centered radial instabilities and discharges with poor vertical control was shorter than the duration for emission in VDE terminations, though still longer than the VDE timescale.

Considered only in arbitrary units, the time integrated final loss hard x-ray intensity (shown in figure 4.12d) varied by only a factor of two for most discharges with either centered radial instability or poor vertical control, while it varies by up to a factor of six for VDE terminations. The increased variation of intensity for VDE terminations could result from RE avalanche during the final rapid current drop, consistent with the longer duration x-ray emission in these discharges as discussed above.

4.2.5 NIMROD modeling

Recent results [72, 71] from the 3D MHD code NIMROD are consistent with several of the experimental findings discussed above. An increased overlap of magnetic islands from tearing modes is predicted following the thermal quench in the diverted case compared with the limited case, with isolated islands in each case. This results in an increased cross-sectional area of stochastic magnetic fields in the diverted case, as compared to the limited case, as shown in figure 4.13. Confinement of RE in these islands is consistent with the twisted RE snakes observed in TEXTOR [84]. Runaways generated in stochastic regions are rapidly transported outside of the plasma boundary to impact the divertor or limiting surface, and this results in decreased RE confinement in the diverted case.

The strike points obtained by following test particle drift orbits in the NIMROD simulations, shown as a green 'X' in figure 4.13, are consistent with the

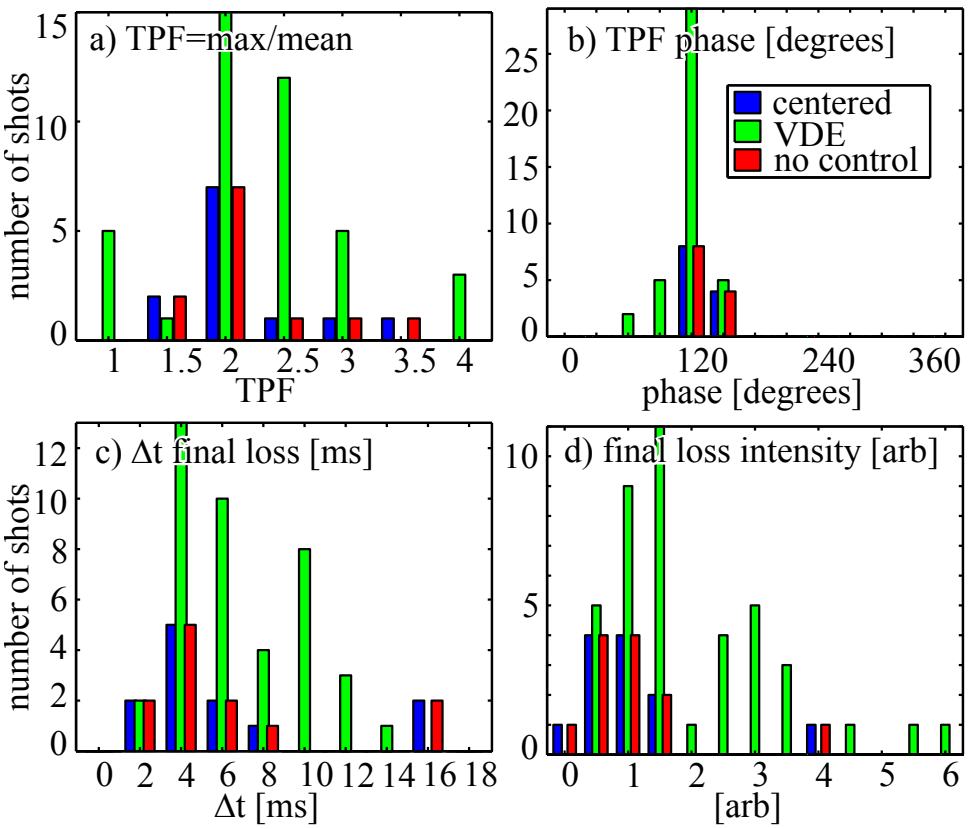

Figure 4.12: A histogram of a) the toroidal peaking factor (TPF) averaged during late loss hard x-ray emission, b) the phase of the peak, c) the duration of final loss, and d) the integrated intensity of final loss.

localized soft x-ray emission observed after the TQ along the floor for diverted shutdowns (figure 4.1f), and the observed absence of soft x-ray emission along the floor for limited shutdowns. The prompt strike is predicted by NIMROD to be toroidally symmetric for the diverted configuration, but there appears to be some asymmetry in experimental hard x-ray emissions, as shown in figure 4.5a. Loop voltages predicted by NIMROD would accelerate negatively charged particles (ie electrons) to the outer strike point in diverted configurations, and no RE are predicted to impact the inner strike point. However there is often a soft x-ray burst seen localized to the inner strike point as shown in figure 4.1f. For the limited configuration, NIMROD predicts that a rotating n=1 mode causes most prompt losses [71] at the limiting point, consistent with the apparent rotating mode seen

in figure 4.8 until 2.015s.

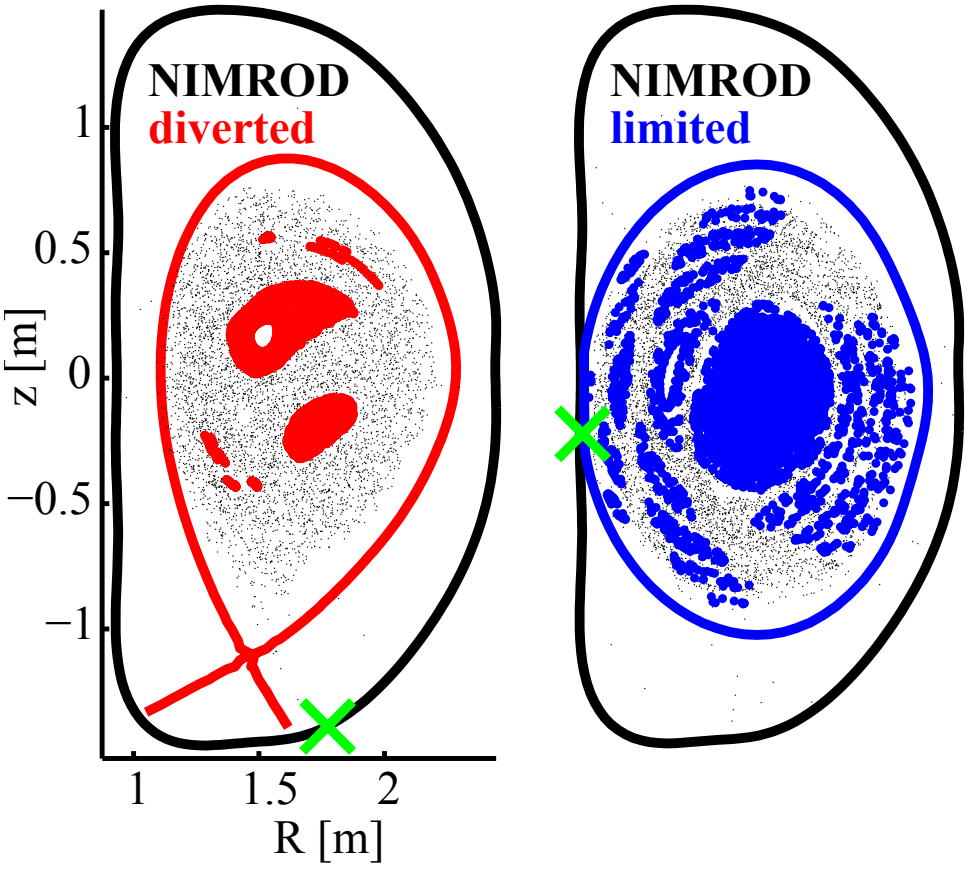

Figure 4.13: Experimental shapes with Poincaré plots generated by NIMROD showing closed surfaces (red and blue) and stochastic field regions (black) at the peak of stochasticity during a disruption. Green X's on the limiting boundary mark strike points for RE de-confined through stochastic regions.

4.2.6 RE energy and loop voltages

As described elsewhere [10], RE kinetic energy is limited primarily by synchrotron radiation except when high density high Z impurity content results in bremsstrahlung emission limiting the power balance. In the analysis below, bremsstrahlung and RE perpendicular energy are therefore neglected to calculate the synchrotron energy limit, since only a small amount of high Z impurities are injected for the shutdown. This limit is the solution to an ordinary differential

equation balancing radiated synchrotron power with kinetic energy gain from the loop voltage: $dW_k/dt = e(V_{loop}/2\pi R)\beta c - P_{syn}$, with the initial kinetic energy defined by Dreicer's critical energy for runaway $W_{Dr} = n_e e^3 ln\Lambda/4\pi\epsilon_0^2 E$, which has the value of a few hundred eV before the CQ begins. The radiated synchrotron power is $P_{syn} = 2/3 a_0 \alpha^2 \gamma^4 (1 - 1/\gamma^2)^2 m_e c^3/R^2$, where a_0 is the classical electron radius, α is the fine structure constant, γ and β are the relativistic parameters, and R is the gyro-averaged radius of curvature. To calculate an upper bound for the energy limit, gyromotion is neglected and the radius of curvature is here assumed the largest it could be: the tokamak major radius. Once generated, runaways rapidly accelerate toward this energy limit W_k, shown in figure 4.1b, calculated with the loop voltage $V_{loop} = -LdI/dt$ where the inductance $L = 2\mu H$ is assumed constant.

Conversely, the average RE energy of $\sim 3MeV$ measured roughly $1ms$ after the first x-ray line emission from the pellet can be used to calculate a minimum bound for the accelerating voltage between the beginning of TQ and this measurement $1ms$ later. Neglecting synchrotron emission and assuming a stationary position at the machine center $R = 1.67m$ and a constant rate of energy gain $dW_k/dt = 3MeV/1ms = eV_{loop}c/2\pi R$, the effective loop voltage must be at least $V_{loop} = 2\pi R dW_k/dt/ec \sim 100V$. The actual voltage must be larger since RE start at a velocity $v \ll c$, and synchrotron emission and other drag forces will reduce the energy gain. If any RE have energies larger than the measured average, as would occur from the broad RE energy distribution predicted by avalanche theory [87]), then again the actual voltage must be even larger. Transient loop voltage spikes in the range of 1000V which last for roughly $1ms$ following the TQ are suggested to exist by taking the time derivative of poloidal flux at the magnetic axis using reconstructions constrained only by fast magnetic diagnostics, though the validity of such techniques has not been verified. Modeling done by other groups [59] predicted loop voltages of $V \sim 500V$ which resulted in substantial RE generation via the Dreicer mechanism [30], though more recent work [36] also includes the hot-tail mechanism with similar results [152]. The origins of the seed REs formed during the TQ phase are important since they may form the precursor to the large

amplitude RE current in the plateau phase. Additional work is necessary to reduce uncertainties and narrow the range of possible loop voltage magnitudes described above.

4.2.7 Bremsstrahlung from runaways

RE are diagnosed in part by the x-ray continuum emitted when they impact plasma ions and impurities, and first wall materials. This bremsstrahlung emission from scattering of high energy electrons off of atomic nuclei and electrons has been thoroughly investigated by several authors [96, 18, 124, 95, 103], and is the topic of at least one textbook [33].

For a simple comparison of the total x-ray energy radiated by a single electron with kinetic energy W_r through collisions with a target thin compared to the stopping distance $\Delta z \ll W/dW/dz$ such as the background plasma, and an electron-opaque thick target $\Delta z > W/dW/dz$ such as the solid vessel walls, use of the following suffices

$$E_{thin} = (dW/dz)_{rad}\Delta z \tag{4.3}$$

$$E_{thick} = \frac{(dW/dz)_{rad}}{(dW/dz)_{tot}} W_r \tag{4.4}$$

The radiative and total stopping powers normalized to mass density are shown for argon and carbon in figure 4.14 for reference.

Since the number of RE in a current I_r is $N_r = 2\pi R I_r/ec$, the corresponding power emitted by a confined RE current of $I_r = 100kA$ with assumed mono-energetic energy $W_k = 10MeV$ in an argon background of density $n_{Ar} = 10^{14}cm^{-3}$, and by a RE current of $\Delta I_r = 10kA$ lost in a time interval $\tau_{loss} = 1ms$ to the graphite wall tiles are respectively

$$P_{thin} = (dW/dz)_{rad} c\beta N_r \tag{4.5}$$

$$\sim 250kW \frac{n_{Ar}}{10^{14}cm^{-3}} \frac{I_r}{100kA} \tag{4.6}$$

$$P_{thick} = \frac{(dW/dz)_{rad}}{(dW/dz)_{tot}} W_r \Delta N_r/\tau_{loss} \tag{4.7}$$

$$\sim 280kW \frac{W_r}{10MeV} \frac{\Delta I_r}{10kA} \frac{1ms}{\tau_{loss}} \tag{4.8}$$

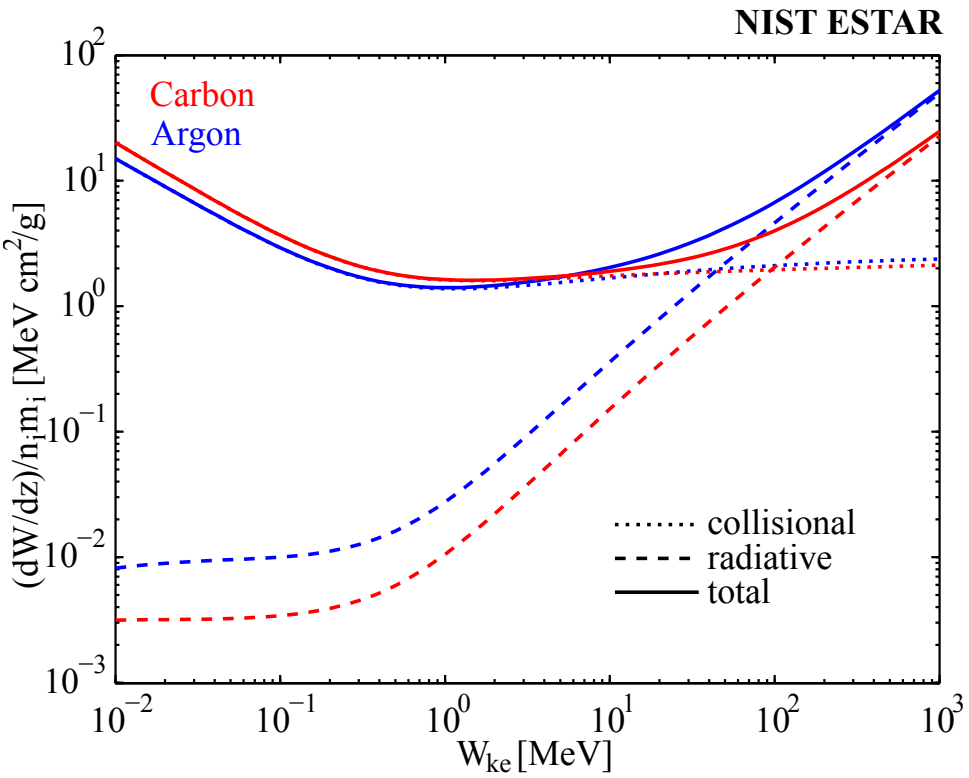

Figure 4.14: A comparison of electron stopping powers (ie drag forces $F_d = dW/dz$) normalized by mass density for carbon and argon as tabulated in the NIST ESTAR database [15].

Such x-ray radiation is not emitted isotropically, but is preferentially beamed along the direction of the RE momentum with a characteristic angle of $1/\gamma = m_e c^2/(m_e c^2 + W_k) \sim 1/5 \sim 10°$.

While these analyses are a bit oversimplified, they can still be used for several simple interpretations of x-ray observations. Even a slow RE loss to vessel surfaces of order seen during RE plateau decay $dI_r/dt \sim 1kA/ms$ will produce roughly $260kW$, more x-ray power than $I_r = 100kA$ of confined RE current in a thin argon plasma. Also, de-confinement of only $\Delta I_r = 1kA$ can easily overwhelm thin target emission if it is lost on short enough timescales. Since emitted x-ray power is a linear function of RE current, it should be possible to infer the amount of RE current from x-ray emissions if the other quantities are known.

4.3 Conclusions

Hard x-ray measurements of runaway electrons (RE) and related analysis during the various phases of argon pellet induced rapid shutdowns of DIII-D have been reported. Energetic (MeV level) seed REs were observed between the thermal quench (TQ) and current quench (CQ) phases indicating the existence of a RE forming mechanism between the TQ and CQ phases. Predictions of loop voltages during this phase were shown to range over a factor of ten. Seed REs were seen to be at least partially de-confined during the TQ into the divertor strike points in diverted discharges. De-confinement was found to be reduced in low elongation limited L-mode shapes, suggesting improved TQ confinement of REs in these discharges, consistent with NIMROD simulations. Limited discharges also showed a higher probability of forming a plateau current than diverted discharges. During RE plateaus, several brief hard x-ray bursts were often observed, coincident with spikes on magnetic probes which indicate a small level of RE wall losses due to the action of an unidentified instability during this phase of the discharge. RE plateaus remained confined for up to several hundred milliseconds but always terminated in an abrupt final loss. Hard x-ray bursts during this final loss often showed a strong toroidal peaking which occurs following a drop in the edge safety factor, suggesting that a kink type instability terminates the plateau discharge.

This chapter contains material to be submitted for publication to Nuclear Fusion in 2011 [78]:

> A. N. James, E. M. Hollmann, G. R. Tynan, M. E. Austin, N. Commaux, N. Eidietis, T. Evans, D. A. Humphreys, A. Hyatt, V. A. Izzo, T. C. Jernigan, R. J. La Haye, P. B. Parks, E. J. Strait, J. C. Wesley, and J. H. Yu. "Measurements of hard x-ray emission from runaway electrons in DIII-D", Nucl. Fus., to be submitted (2011)

The dissertation author was the primary investigator and author of this paper.

Chapter 5

Interaction between runaways and injected pellets

This chapter describes results from experiments studying the interaction of solid polystyrene pellets with a runaway electron current channel generated after cryogenic argon pellet rapid shutdown of DIII-D. The experimental procedure is described in section 5.2. In section 5.3, imaging data from a fast camera is shown detailing the pellet trajectory and continuum emission from the subsequent explosion, with a geometric camera calibration enabling detailed analysis of the pellet explosion and runaway energy. Discussed in section 5.4 is electron cyclotron emission believed to result from knock-on electrons broken free from the pellet which then accelerate and runaway, and also from a short lived hot plasma blown off the pellet surface. In addition, heating and explosion times from observations and a model of pellet heating and breakdown by runaway interaction are compared in section 5.6.

5.1 Motivation

The previously described techniques for diagnosing runaway electron properties in tokamak disruptions were all passive, relying on distant observations of radiation emitted by runaways. The pellet injection experiments described in this section venture into a realm of actively probing and interacting with runaways

which has rarely been attempted previously. These experiments attempted to study x-ray emission anticipated from interaction between injected pellets and runaway current, hence probing the spatial profile of runaway current density and energy distribution. While the expected x-ray emission was not observed, new clues were still revealed about these runaway properties.

5.2 Impurity pellet injection

These experiments used the DIII-D lithium pellet injector which uses $3.4MPa$ helium gas to inject pellets at $700m/s$ into runaway current plateaus. Up to three $2mm \times 2mm$ pellets can be injected at different times. The pellet volume $V = 2mm \times \pi(1mm)^2 = 6.28mm^3$ with density $\rho = 1060kg/m^3$ contains $N_{CH} = \rho V/m_{CH} = 3.1 \times 10^{20}$ simple hydrocarbons. After testing various materials, polystyrene was selected due to its improved properties for all of the above except a lower vaporization temperature which results in decreased penetration into the runaway current channel. The higher vaporization temperature for carbon makes it a more desireable pellet media, but brittle carbon pellets shatter in the curved guide tube which delivers pellets to the tokamak, and abrasive grinding of carbon against the guide tube walls in a vacuum environment increases variation in pellet delivery velocities. Other details of the pellet injector hardware are presented in appendix C.

As discussed previously, EGSnrc Monte-Carlo modelling [91] indicates a shower of x-rays emitted from runaways scattering off the solid pellets, however no such emission was observed in these experiments. This could occur due to peaking of the runaway current density, so that the pellet is destroyed in an edge region of reduced runaway current density, hence producing reduced x-ray emission below the detection threshold.

Diagnostic polystyrene pellets are injected in the middle of runaway plateau, after the argon killer pellet has already caused thermal quench and current quench, and generated runaways. In addition to the numerous diagnostics and other hardware which was discussed in section 3.2 and shown in figure 3.3, a spectrometer

and impurity pellet injector were used here as depicted in figure 5.1. This combined experimental hardware was used to observe the interaction of the pellet with runaways.

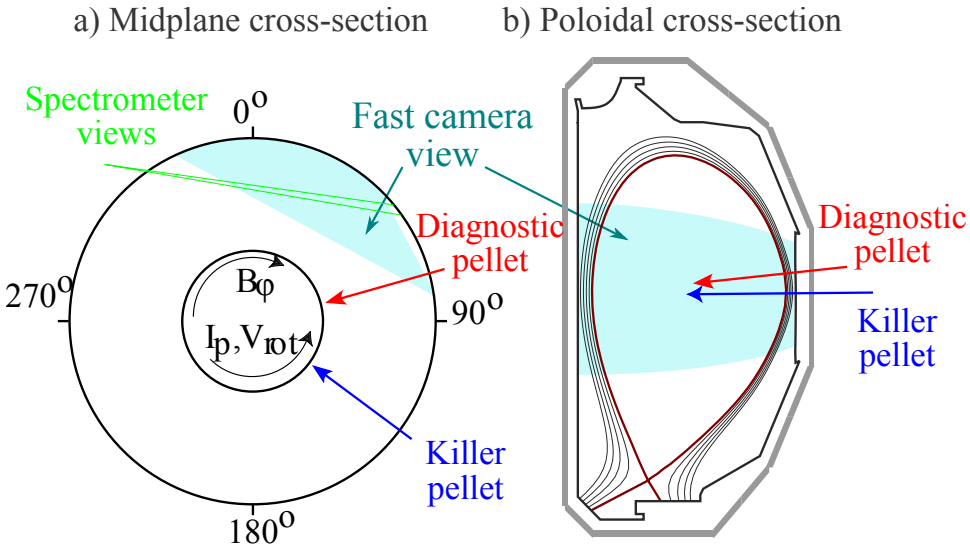

Figure 5.1: Layout of diagnostics and experimental hardware used in pellet injection experiments studying runaways, with a) a top down midplane cross-section, and b) a poloidal cross-section. Note that not all diagnostics lie in the same poloidal plane.

Diagnostics observing signatures of the pellet interacting with runaways include a fast visible imaging camera, an ECE radiometer, and a spectrometer used usually for observing charge exchange recombination, but x-ray diagnostics show no expected emission from runaways scattering off the pellet, all shown in figure 5.2. Fast visible imaging observations, shown in figure 5.4, suggest the presence of a steep runaway energy and/or current gradient, since the visible synchrotron radiation occurs proportional to runaway density and the synchrotron wavelength depends strongly on runaway energy. Analysis of cyclotron emission indicates a loop voltage present which exceeds external measurements, indicating the need for a better in-situ measurement and understanding. Runaway current appears relatively unaffected by the pellets compared to impurity injection experiments at JT-60U [90] and Tore-Supra [146], perhaps due to the smaller amount ($10 torr \cdot L$) and lower atomic number of injected impurities in the present experiments.

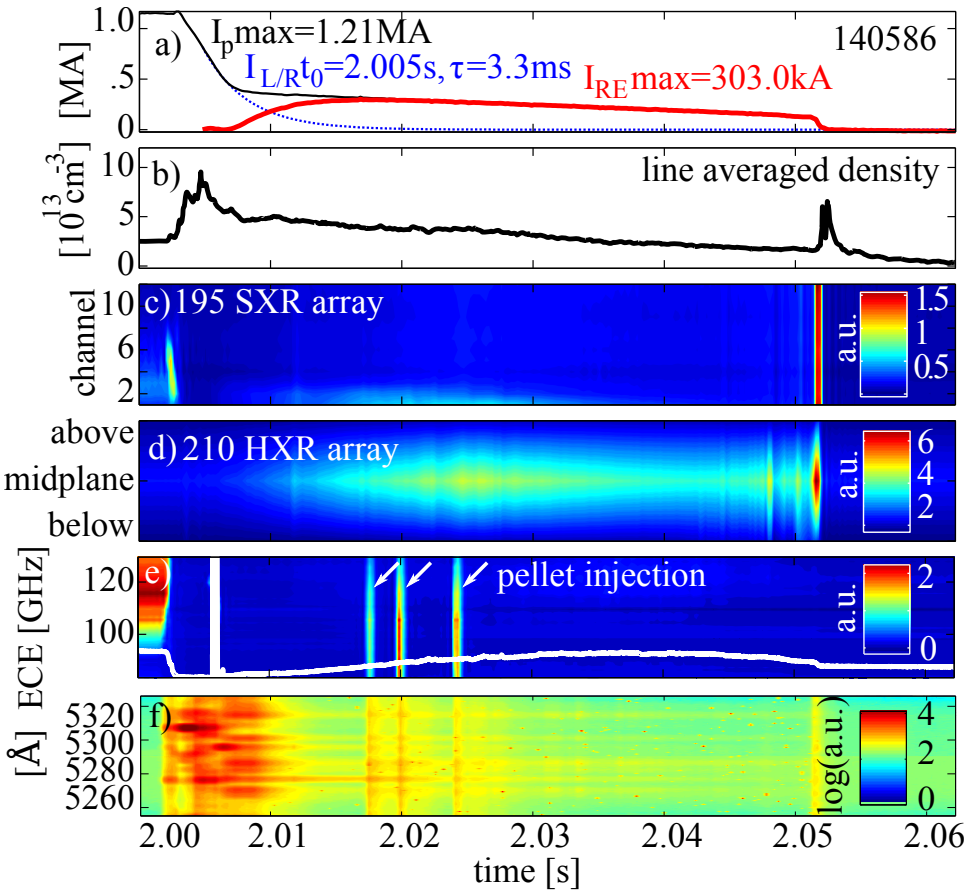

Figure 5.2: Data observed during the experiment including a) plasma current I_p, fit to L/R current decay time, I_{LR}, subtraction of the two for runaway current I_r, b) density, c) soft x-ray data shown by chord number (see fig 3.3), d) a poloidal array of three hard x-ray scintillators [79], e) cyclotron emission power spectrum, and f) a portion of the visible emission spectrum.

5.3 Visible Imaging

As shown in figure 5.4, the Phantom v7.1 visible imaging camera records 12μs exposures of the pellet traversing the vacuum vessel illuminated either by cold background plasma or by a low runaway current density until it comes within a few centimeters of the last closed flux surface (LCFS), where it abruptly explodes from runaway impact.

The LCFS curves through the camera view, which complicates interpretation somewhat. Synchrotron emission from RE observed by the camera is brightest

in pixels viewing tangent to the magnetic field due to forward beaming of the radiation. The points where pixels are tangent to the magnetic field all lie roughly in one plane, referred to as the plane of tangency, which is in the background compared with the injected pellet plane. In this plane of tangency, the LCFS is much farther to the right of the image (blue outlines in figure 5.4b) compared to the plane of pellet injection, where the LCFS appears in the bottom-left of the image (red outline in figure 5.4b).

The camera sees no $\lambda_c \lesssim 700nm$ runaway synchrotron emission outside the LCFS, but sees light inside the LCFS corresponding to $W_r > (\frac{2\rho}{3\lambda_c})^{1/3} m_e c^2 = 60MeV$ [76] for radius of curvature ρ, accurate to a factor of 2-3 due to slow cutoff of the synchrotron spectrum and spectral sensitivity of the camera. This indicates the presence of a strong runaway energy and density gradient around the LCFS. In other fast-shutdowns, reflectometer measurements of the cold plasma maintained by runaway collisions with background gas reveal substantial plasma density many centimeters beyond the LCFS at the midplane, as shown in figure 5.3. This suggests that RE may not be well confined inside of the LCFS.

The pellets explode outside the LCFS, the position of which is determined by JFIT magnetic reconstructions [68], from interaction with runaways confined there due to a relativistic drift orbit displacement effect [123] which also yields an estimate of runaway energy. We measured a pellet velocity of $725m/s$ and located the pellet explosions to roughly $d = 16cm$ outside of the last closed flux surface (see fig 5.4a annotation). Passive spectroscopy of ion emission in the cold background plasma indicates a temperature of roughly $1.5eV$ and single ionization, too cold to cause a pellet explosion, so the only remaining heating source is RE interaction with the pellet. From the observed displacement and a JFIT calculation of $q_a = 6$, we calculate a rough measure of runaway energy [34, 12, 177] of $W_r = decB/q = 17MeV$ for runaways which destroy the pellet. Visible synchrotron emission in the core suggests high energy runaways there, so lower energy runaways which synchrotron emit invisible infrared radiation must exist outside the LCFS which destroy the pellet. Continuum emission (figure 5.2f) from the explosion front (figure 5.4b) expands at a velocity of $v = 1200m/s$, corresponding to a temperature

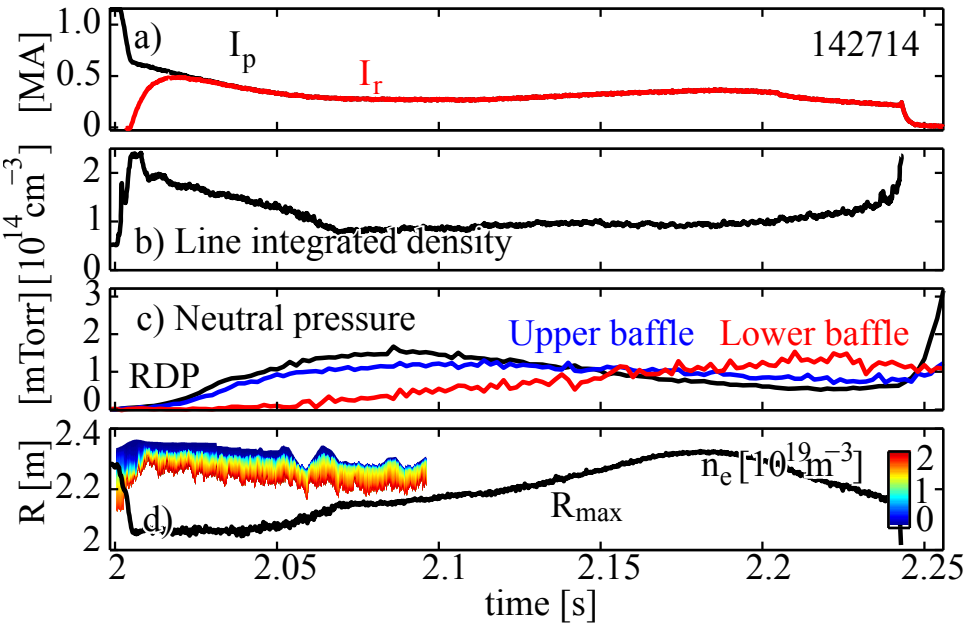

Figure 5.3: Measurements of plasma current, line integrated electron density, neutral pressure at the wall, reflectometer measured electron density profile, and the maximum radius of the last closed flux surface.

of $750K$ for an assumed CH, $m = 13amu$ gas.

5.4 Observed cyclotron emission

Just after the pellet explosion, a burst of ECE occurs in the $80 - 130GHz$ (2nd harmonic) band with a fast $\sim 10\mu s$ component and a slow $\sim 100\mu s$ component, shown in figure 5.5 for each of the three injected pellets. The physical mechanisms of these ECE band bursts are not entirely understood, however they are believed to result from a combination of hot plasma ablated from the pellet, and emission from non-thermal electrons scattered in the perpendicular direction by the pellet. Other than this burst, cyclotron emission is generally non-existent at this phase due to the low post-TQ plasma temperature. While these emissions cannot be plainly interpreted as temperature due to uncertainties in plasma conditions and thermal equilibrium, the emitted powers are compared with power emitted by a thermal plasma with equivalent temperature for reference. The fast component

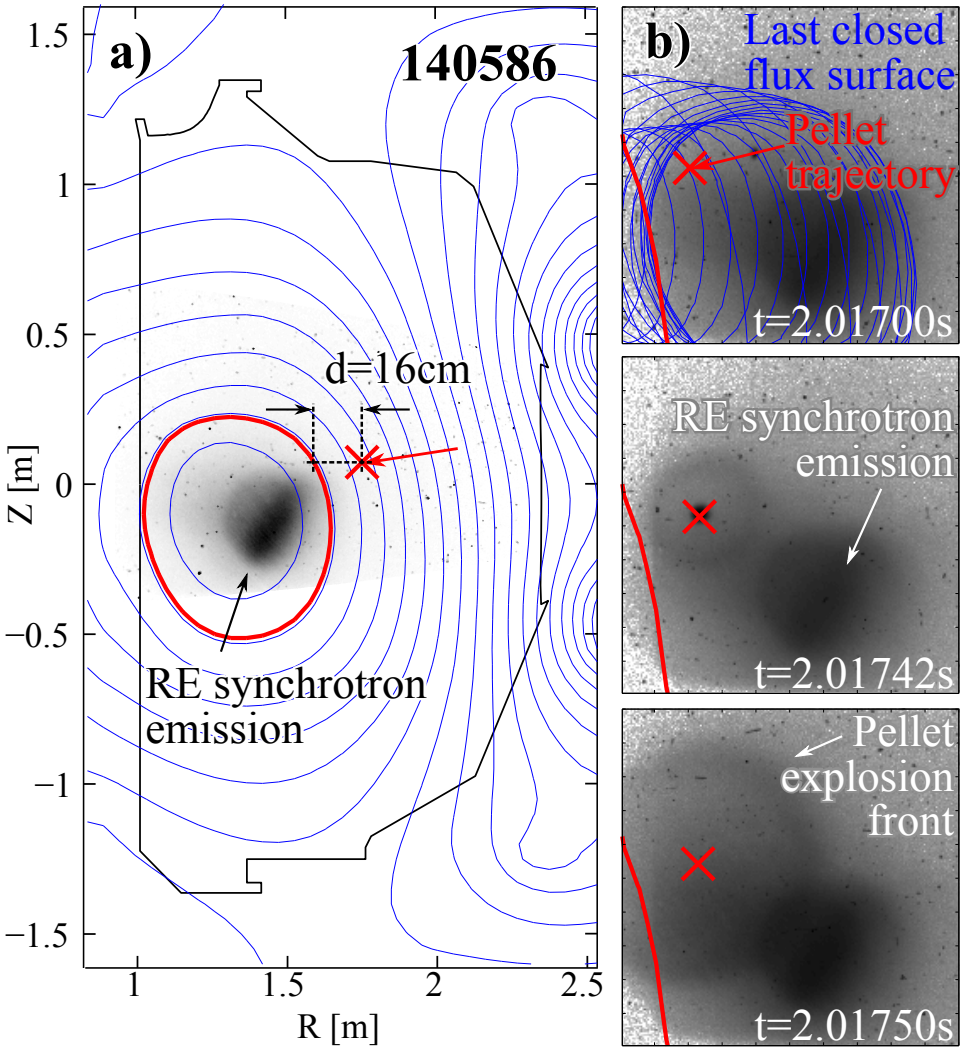

Figure 5.4: On the left, a) a visible camera frame mapped into the poloidal R,Z plane from just before injecting the first pellet. The last closed flux surface, pellet trajectory, and pellet explosion location are marked in red. On the right, b) a sequence of three images for the first pellet injected, with the pellet trajectory in red, and the LCFS in the poloidal plane of pellet injection in red in the foreground, and the background LCFS marked at various toroidal locations in blue. The view spans a curving plasma geometry which is mapped to the R,z plane with the tangency points between magnetic field lines and pixel lines of sight, accurate to a few millimeters.

intensity varies per pellet in equivalent temperature from below $1keV$ to above $5keV$ and may represent emission from non-thermal knock-on electrons from the pellet with the emitted spectrum determined by the knock-on energy spectrum

described previously [87]. The slow component seems to remain more constant pellet to pellet at around $1keV$ between the three pellets and may correspond to hot plasma blown off of the pellet or thermal electrons heated by collisions with low energy non-thermals.

The fast emission frequency drops at a rate of $d\omega_c/dt = -183GHz/ms$ which suggests a relativistic increase in mass as knock-on electrons from the pellet accelerate. The corresponding rate of acceleration would be

$$dW/dt = -\gamma^2 m_e c^2 (m_e/eB) d\omega_c/dt = 1MeV/ms \tag{5.1}$$

which corresponds to an effective local loop voltage of at least $35V$ assuming zero drag and electrons moving at the speed of light. Non-thermal electrons at subluminal velocities would experience a greater drag and hence would correspond to an even greater voltage, but without an accurate measure of these electrons' starting energy we cannot estimate that voltage. In either case however, this loop voltage significantly exceeds the zero dimensional loop voltage measured by external coils at this time, suggesting that large internally localized loop voltages may exist which are screened from surrounding magnetic diagnostics.

5.5 Discussion of cyclotron emission in the relativistic limit

In the non-relativistic limit for an electron moving perpendicular to the magnetic field in a thermal plasma, it will gyro-orbit at the cyclotron frequency $\omega_c = eB/m_e$ in circular paths with an acceleration $a = v_{Th}\omega_c$, and the total radiated power is determined by Larmor's formula [77]

$$P = \frac{e^2 a^2}{6\pi\epsilon_0 c^3} = \frac{kT_e m_e}{6\pi\epsilon_0 B^2 c^3} \tag{5.2}$$

This makes electron cyclotron emission a nice diagnostic of electron temperature, since the magnetic field has a well known dependence on major radius $B(R) \propto 1/R$ which translates the cyclotron power spectrum $P(\omega_c) \propto T_e$ into a spatially resolved electron temperature $T_e(R)$.

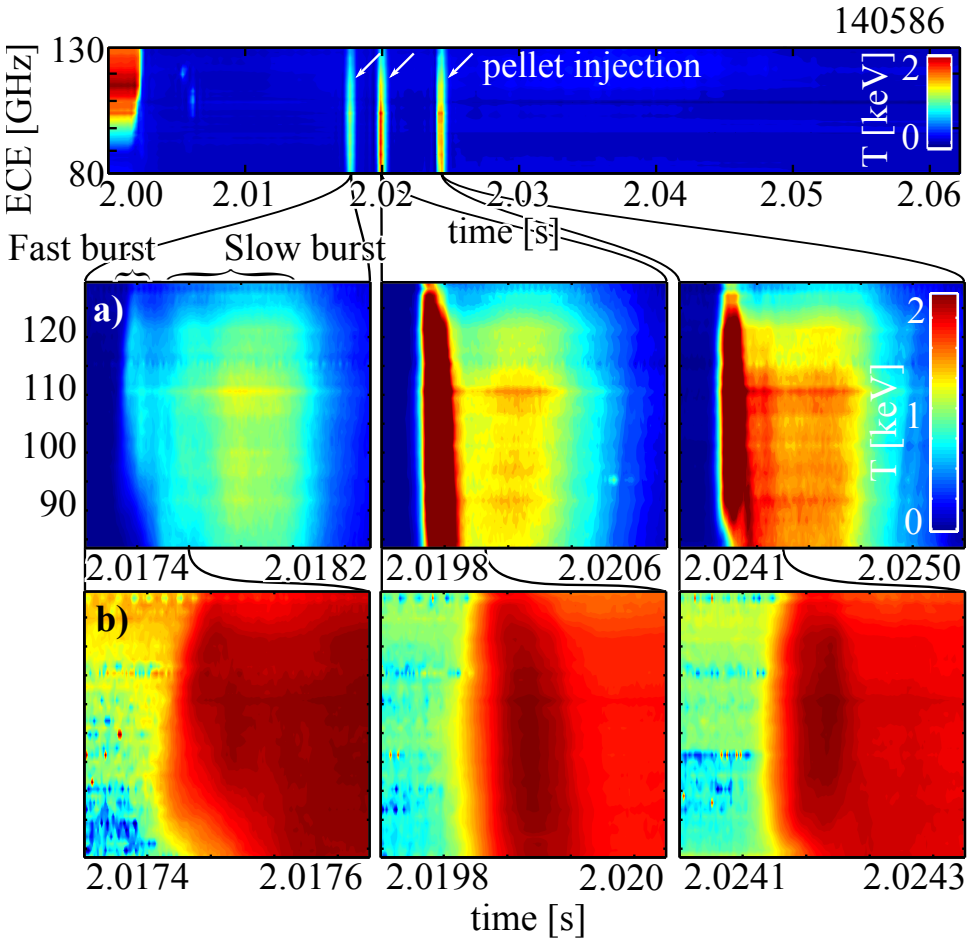

Figure 5.5: a) Cyclotron emission bursts featuring a fast and slow component, and b) a zoom on the fast component in arbitrary log scale, with possible frequency drift annotated.

Electron cyclotron emission occurs quite differently in the relativistic limit compared with the above typical thermal emission. As the relativistic parameter increases $\gamma > 1$, the cyclotron frequency reduces as if the electron were gaining mass $\omega_c = eB/\gamma m_e$. The total radiated power for a relativistic particle is determined by Liénard's result [77]: $P = \frac{e^2\gamma^6}{6\pi\epsilon_0 c}[(\dot{\beta}^2) - (\beta \times \dot{\beta})^2]$, with the normalized velocity $\beta = v/c$. This result for the power radiated due to electron gyromotion was

simplified for runaway electron relevant conditions in a tokamak by Bakhtiari [9, 10]

$$P = F\beta c = \frac{dq}{d\tau} m_e c\nu = F_{gy}\frac{q_\perp^2}{q^4}\gamma^4\beta^4 m_e c^2 \nu \qquad (5.3)$$
$$= \frac{B^2 e^4}{6\pi\epsilon_0 m_e^2 c}\frac{q_\perp^2}{q^4}\gamma^4\beta^4$$

where $q = \frac{p}{m_e c} = \gamma\beta$, $\tau = \nu t$, $\nu = \frac{n_e e^4 ln\Lambda}{4\pi\epsilon_0^2 m_e^2 c^3}$, and $F_{gy} = \frac{2\epsilon_0 B^2}{3n_e m_e ln\Lambda}$. The strong dependence on the relativistic parameter γ results in strong emission from even a small number of runaways, hence why non-thermal emission occasionally overwhelms cyclotron emission diagnostics.

5.6 Pellet heating and breakdown by runaways

An important topic for future tokamaks is the interaction between runaway electrons and vessel materials, since this interaction may result in damage to the vessel. This section contains a discussion of runaway electron energy deposition in pellets, the subsequent breakdown of the pellet material, and modelling of how these interactions might scale to other materials.

For a brief consideration of pellet heating and breakdown by runaways, consider a runaway energy of $W_r = 17MeV$ corresponding to the observed displacement away from the LCFS, and a flattop runaway current profile spread uniformly throughout the cross sectional area $A_r = .36m^2$ giving current density of $j_r = 512kA/m^2$. At this energy the stopping power of RE in polystyrene $s \sim 2.5MeVcm^2/g$ [15] corresponds to a mean free path of about 7cm which exceeds the pellet size, resulting in volumetric heating instead of a slower ablation type pellet burn up observed and thoroughly modelled for pellets injected into hot plasmas [135, 14, 148] In polystyrene with a density of $\rho = 1060kg/m^3$, the volumetric heating power

$$Q = (j_r/e)(dW/dx) = \rho s j_r/e \sim 125MW/cm^3 \qquad (5.4)$$

results in a temperature rise rate of $dT/dt = Q/C\rho = 100K/\mu s$ at this power density which takes only a few microseconds to melt and vaporize the pellet.

The pellet temperature continues to grow after melting until power loss from evaporation at the surface and thermal radiation balance runaway heating and clamp the temperature, as described in detail elsewhere [141]. Where core temperature exceeds the boiling point in vacuum, the liquid will break up by vapor bubbles into smaller and smaller fragments until surface tension balances evaporation at the smallest sizes, when droplet core temperature may increase again. Since runaway energy exceeds the enthalpy for evaporation $E_{ev} \sim .73eV/molecule$ by orders of magnitude, it is also possible for direct sublimation to occur before bulk heating causes melting and evaporation. Camera observations have neither the spatial or temporal resolution to discriminate between these processes.

The above simple model does not describe the deposition of energy from RE within larger pellets or different materials, which are studied here briefly with the EGSnrc Monte-Carlo model [91]. A slab geometry of $d = 45mm$ depth and $r = 45mm$ radius was set up in EGSnrc and a thin $r = 0.1mm$ pencil beam of $W_k = 20MeV$ electrons was impacted normal to the surface. Energy deposited per unit volume of the slab per unit incident electron fluence is then recorded as a function of radius and depth as shown in figure 5.6. This reveals a shallower and narrower penetration for higher atomic number (Z) materials, indicating a more lathe-like ablation of these pellets instead of volumetric heating and disintegration. Conversely, runaways may penetrate multiple centimeters of low-Z materials; hence even large pellets will explode. The more volumetric energy deposition in low-Z materials also helps to explain how tokamaks with graphite first walls rarely show signs of damage from RE impact, while higher-Z materials such as molybdenum and tungsten are substantially melted and damaged by RE impact.

5.7 Conclusions

We observed explosion of injected pellets upon contact with RE, suggesting a volumetric heating by penetrating RE. The cyclotron emission frequency drift observed indicates a local loop voltage of greater magnitude than externally measured, suggesting the need for improved in-situ loop voltage measurements and

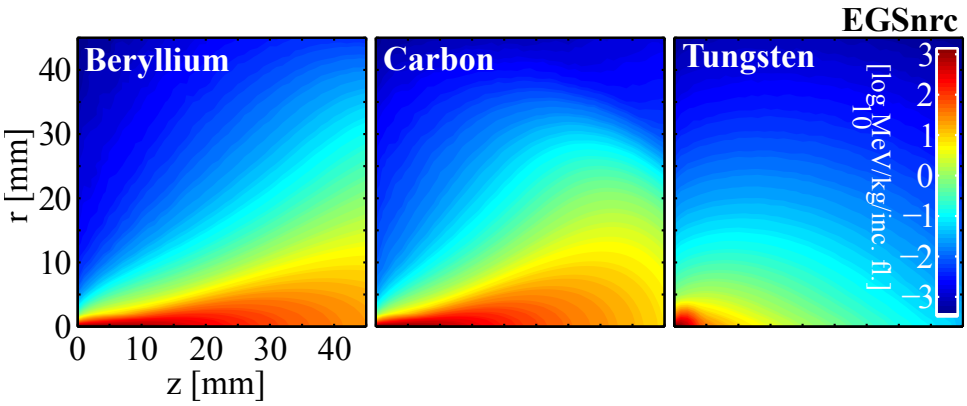

Figure 5.6: Energy deposition simulation using EGSnrc for a pencil beam of 20MeV RE impacting various materials from the left at $r = 0$, $z = 0$.

understanding. Comparison of the pellet heating and explosion rate agrees with modelling and a theory for pellet breakdown by RE impact within an order of magnitude.

This chapter contains material published in the Journal of Nuclear Materials in 2011 [80]:

> A. N. James, E. M. Hollmann, J. H. Yu, M. E. Austin, N. Commaux, T. Evans, D. A. Humphreys, T. C. Jernigan, P. B. Parks, S. Putvinski, E. J. Strait, G. R. Tynan, and J. Wesley. "Pellet interaction with runaway electrons", J. Nuc. Mater., In press (2011)

The dissertation author was the primary investigator and author of this paper.

Chapter 6

Determining loop voltages during tokamak rapid shutdowns

In this chapter, techniques are described for inferring loop voltages with high time resolution in killer pellet rapid shutdowns of tokamak plasmas. Bolometer tomography is used to inspect the cooling rate localized near the killer pellet, which is shown to occur much faster than volume averaged cooling. This rapid cooling corresponds to a rapid increase of plasma resistivity, which results in a transient spike of loop voltages in the plasma. Instead of calculating loop voltages by the current decay, loop voltages are inferred using inverse techniques with arrays of magnetic diagnostics situated around the vessel wall external to the plasma boundary. Inferred voltages peak $1ms$ before the main current quench (CQ) begins, are over $1kV$ in magnitude, and are believed to originate a small 'seed' current of runaway electrons (REs) by the Dreicer or hot-tail mechanism.

Since loop voltages during rapid shutdowns are driven primarily by rising resistivity associated with the thermal quench (TQ), it is important to confirm that the cooling time is short enough to cause inferred loop voltages. Due to cutoff of broadband electron cyclotron emission (ECE) discussed in section 3.7.1, the volume averaged cooling time inferred using broadband ECE $\tau_{TQ} \geq 500\mu s$ may be shorter than the actual cooling time. Since the Thompson scattering diagnostic is also disabled by stray light from the radiating plasma during the TQ, bolometer tomography is pursued to inspect the cooling time during the TQ.

Evidence was shown in section 4.1 for loop voltages accelerating RE to high energy before the CQ, including hard x-ray emission observed outside of the vacuum vessel simultaneous with soft x-ray emission localized to the divertor outer strike point, and non-thermal electron cyclotron emission associated with RE. During the CQ, the loop voltage was estimated in section 1.4.3 to be $V_{loop} = -LdI/dt = 400V$, however this voltage occurs only after REs are first observed and is otherwise too small to generate REs, which motivates a search for earlier and larger loop voltages. A simple lower bound estimate for the loop voltage before the CQ of $V_{loop} \geq 2\pi RdW_k/dt/ec \sim 100V$ was reported in section 4.2.6 using another technique based on roughly inferred RE energy of $W_k \sim 3MeV$ and the time since beginning of the thermal quench (TQ) until RE strike the wall $\Delta t \sim 1ms$. Since this estimate is not time resolved and the RE energy is only roughly known within a factor of ten, inverse techniques with magnetic diagnostics are pursued to study the fast voltage dynamics.

The rest of this chapter describes these techniques and their ramifications as follows. Brief reviews of the theory of transient increases in loop voltages due to rising resistivity, radiative cooling, and killer pellet ablation models are presented in section 6.1. A cooling time faster than that inferred from ECE is inferred using bolometer tomography to reveal the local radiated power around the injected killer pellet and the associated local cooling time in section 6.2. Loop voltages with spatial and high temporal resolution are inferred from fast magnetic diagnostics using inverse techniques in section 6.3.

6.1 Review of voltage sources in a cooling plasma

One probable cause for voltage spikes during disruptions is the resistivity spike which results from rapid cooling in the TQ. During typical tokamak operation, the hot plasma has a low resistivity which enables current of roughly $I = 1.5MA$ to be driven by applying only a small toroidal loop voltage. The resistivity and the corresponding loop voltage both spike by many orders of magnitude in response to rapid cooling during the TQ, as discussed further in section 6.1.1.

Such large voltage spikes and rapid cooling are the two primary causes of runaway electron generation as described in sections 2.1.1.1 and 2.1.1.2 respectively.

6.1.1 Spitzer resistivity and hyper-resistivity

During normal operation, $T_e = 3keV$, $n_e = 10^{13}cm^{-3}$, and $Z_{eff} \sim 1$, corresponding to a Spitzer resistivity [155] of:

$$\eta = 1.66 \times 10^{-9} Z_{eff} T_{e,[keV]}^{-3/2} ln\Lambda = 5.4 \times 10^{-9} \Omega m \tag{6.1}$$

For a top-hat distribution of current $I_p = 1.5MA$ over an area of $A = \pi a^2 = 1.4m^2$ the corresponding current density is $j = 1.1MA/m^2$. The resulting small electric field during normal operation is $E = \eta j = 0.006V/m$.

The causative factor in toroidal E-field spikes during disruptions is a combination of the rapidly rising resistivity η as the plasma cools, and changes in the current profile j. During the TQ phase, the plasma temperature drops from an initial peak of about $T_{ei} = 3keV$ to a final volume averaged $T_{ef} = 10eV$ in roughly $200\mu s$. Assuming density and effective charge state stay the same, the corresponding resistivity change is a factor of $\eta_f/\eta_i = (T_{ef}/T_{ei})^{-3/2} = 5000$, and the Coulomb logarithm $ln\Lambda$ also drops slightly. If the current density also remains the same, the corresponding electric field after TQ hence increases to $E = 20V/m$.

During the TQ, the plasma parameters relevant to resistivity: density n_e, temperature T_e, and effective charge state Z_{eff}, are expected to vary strongly in space in addition to time. Two- and three-dimensional localization could result in an even higher resistivity: with a lower localized temperature and a higher localized effective charge state and density than zero-dimensionally inferred. Any peaking of the current density will also contribute to a higher electric field. Unfortunately, these plasma parameters are poorly diagnosed during the TQ, so some other approach is necessary to infer the electric field, such as simulations or direct magnetic measurements.

In magnetically stochastic regions, the resistivity is predicted to be enhanced [17] beyond the classical Spitzer resistivity proportional to the square of

the radial magnetic fluctuation. As discussed previously in section 4.2.5, the 3D MHD code NIMROD predicts [71] that large regions of the plasma are magnetically stochastic as a result of large amplitude MHD during the TQ until well into the CQ. NIMROD does not model the penetration and diffusion of killer pellet impurity transport throughout the plasma, but it instead assumes an initial condition of evenly distributed impurity content, though this approach remains the most sophisticated MHD modeling of stochasticity in a shutdown to date. Large loop voltages are also predicted to occur in regions of magnetic reconnection, as described elsewhere [162]. While a detailed calculation of the resistivity increase due to hyper-resistivity is beyond the scope of this thesis, it is worth noting that the Spitzer resistivity may not capture all the physics of resistivity spikes during the TQ, and that the actual resistivity and corresponding loop voltages may be larger than predicted by Spitzer theory.

6.1.2 Models of radiative cooling and killer pellet ablation

Several models have been developed in prior work to simulate radiative cooling and ablation of pellets injected into hot plasmas. These models and some key projections are briefly recounted here. Experimental measurements and inference are used wherever possible, but key projections will be cited and used later where experimental measurements are lacking.

6.1.2.1 Radiative cooling modelled by KPRAD

Prior work on zero-dimensional modeling of the TQ [65] resulting from radiating impurities such as argon can be used to infer how plasma parameters may evolve through a TQ in absence of experimental measurements. This prior work used the code KPRAD, originally developed [166] to model disruption evolution due to injection of radiating impurities. Such modeling results are critical for estimation of the effective charge state, since the visible bremsstrahlung diagnostic usually used to measure the effective charge state fails during disruptions, as discussed in section 3.8.4. KPRAD uses an energy balance between thermal and magnetic energy and radiation rates for uniformly distributed injected impurities

to calculate the plasma parameter evolution, including the effective charge state, throughout a shutdown.

Given an initial condition for the plasma current, density, and temperature, and the number and type of injected impurities, KPRAD calculates the evolution of these quantities similar to volume averaged experimental observations for temperature, density, current, and radiated power. As shown in figure 6.1, KPRAD predicts a spike of the effective charge state to $Z_{eff} \sim 8$ at the end of the TQ, which then decays roughly exponentially on a timescale of $\sim 4ms$, similar to the CQ timescale. Combining this predicted spike of the effective charge state with the above calculation results in a resistivity spike of over four orders of magnitude from the normal operating value. Since KPRAD assumes uniform impurity distribution, the actual effective charge state may differ substantially from this value on small spatial scales, but it remains the best available estimate and a larger effective charge state is unlikely [134].

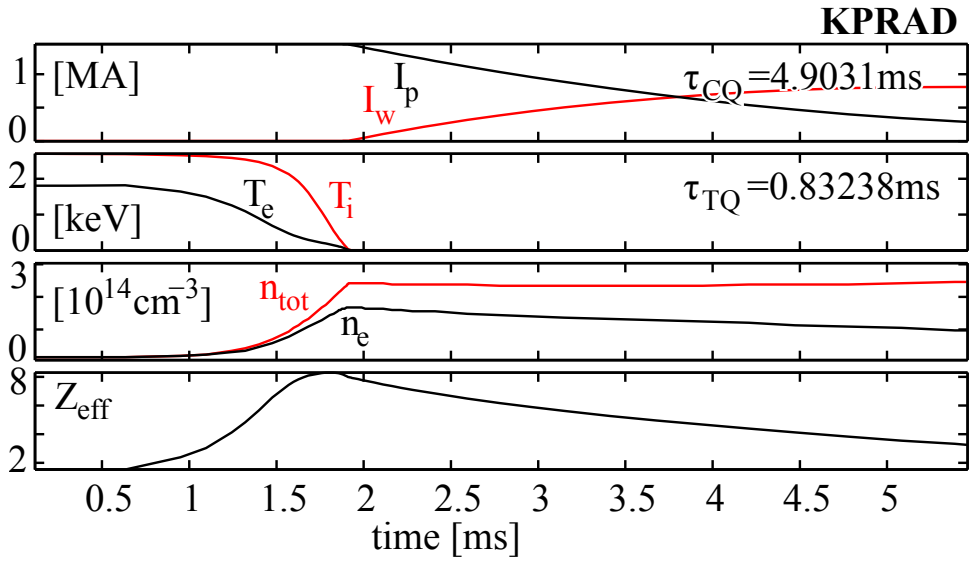

Figure 6.1: Time histories of various quantities of relevance during a disruption calculated with the KPRAD code, and runaway production corresponding to the generation mechanisms described by equations 2.4, 2.7, and 2.8.

6.1.2.2 Killer pellet models

In some of the earliest killer pellet modeling work [35], the zero dimensional code KPRAD was used on a 1D grid to simulate plasma parameters resulting from the pellet advancing through the hot plasma, with no diffusion assumed between grid points. More recent work [45] developed a one dimensional code which assumes symmetry in the toroidal direction and along flux surfaces, and self consistently models plasma parameters based on predictions from the neutral gas shielding (NGS) model [135]. Another model [110] predicts an ablation cloud expanding to a toroidal tube with a radius of roughly $r_{tube} = 10mm$ for cryogenic neon pellets with a radius of $r_{pel} = 0.12mm$ and a peak localized density as high as roughly $n = 10^{20}cm^{-3}$. The argon pellets used at DIII-D have a larger radius $r_{pel} = 1.35mm$, and the width of emission will be shown to be roughly $r_{tube} = 10cm$ in section 6.2, while the peak localized density is assumed to be the same $n = 10^{20}cm^{-3}$. Ablation rates in the range of $\dot{N} \sim 10^{21} - 10^{22}atoms/s$ are estimated using NGS [101, 148].

6.2 Thermal quench timing with bolometer tomography

This section describes measurements suggesting that the local TQ time may be substantially faster than the volume averaged TQ time. In section 3.7.1, the notion was raised that the TQ time may actually be larger than the apparent volume averaged TQ time inferred from broadband ECE because of a cutoff phenomenon. A longer TQ time would imply a more gradual increase of resistivity corresponding to a reduced loop voltage, but a shorter TQ time is one reason to believe that loop voltages may be even larger, and occur earlier, than previously believed. The TQ could occur much faster than the volume averaged rate on smaller spatial scales due to rapid local cooling near the argon killer pellet. Using bolometer tomography and a simple power balance model, this faster TQ time is estimated below.

The tomography routines used at DIII-D were previously developed based

on significant advances over early reconstruction techniques like the Cormack method [27, 50], optimizing the reconstruction to the tokamak viewing and physical geometries [41, 69]. The algorithm maps data from four 16 channel cameras arranged as crossed fans onto a flux function like grid covering the emission region, both shown in figure 6.2.

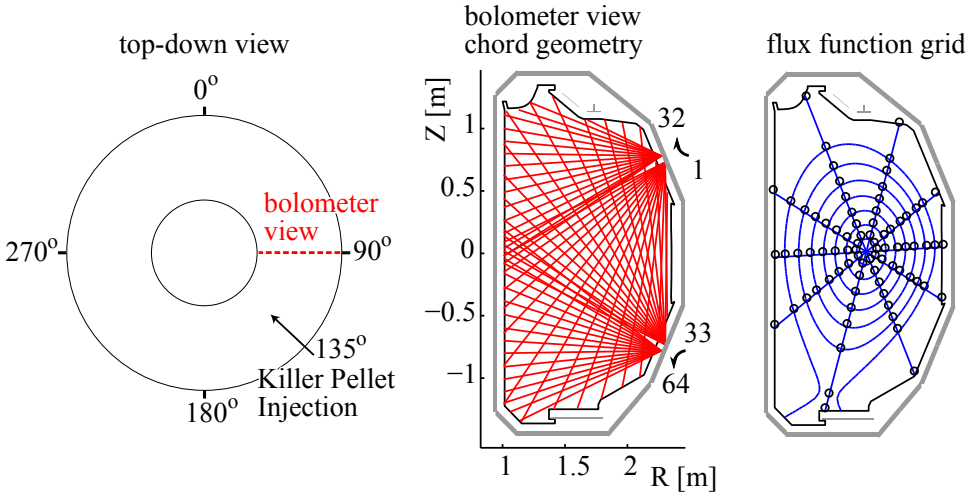

Figure 6.2: A view from the top of the torus showing toroidal spacing between the bolometer view and killer pellet injection locations, and poloidal views showing the emission region covered by the numbered bolometer chords and the flux function grid used for tomographic inversion.

Using these algorithms and grid, the tomographic reconstruction finds a solution which both matches the original data closely and also matches the physical situation of a small pellet radiating strongly, as shown in figure 6.3. The reconstruction shows a strongly peaked point emission with a spatial extent of roughly $10cm$ which is believed to result from radiating argon ablated from the pellet by hot plasma, with a peak radiated power of roughly $P_{rad} = 10GW/m^3$. Since the bolometer array is spaced roughly 45 degrees toroidally from the pellet injection point as shown in figure 6.2, the observed peak radiated power may be lower than occurs at the pellet. This peak tracks the killer-pellet trajectory at an average velocity of $850m/s$, consistent with the velocity measured at the launcher. Fast poloidal transport of ablated impurities is also observed, corresponding to a plume drift velocity of $50km/s$, or poloidal rotation frequency of $100kHz$.

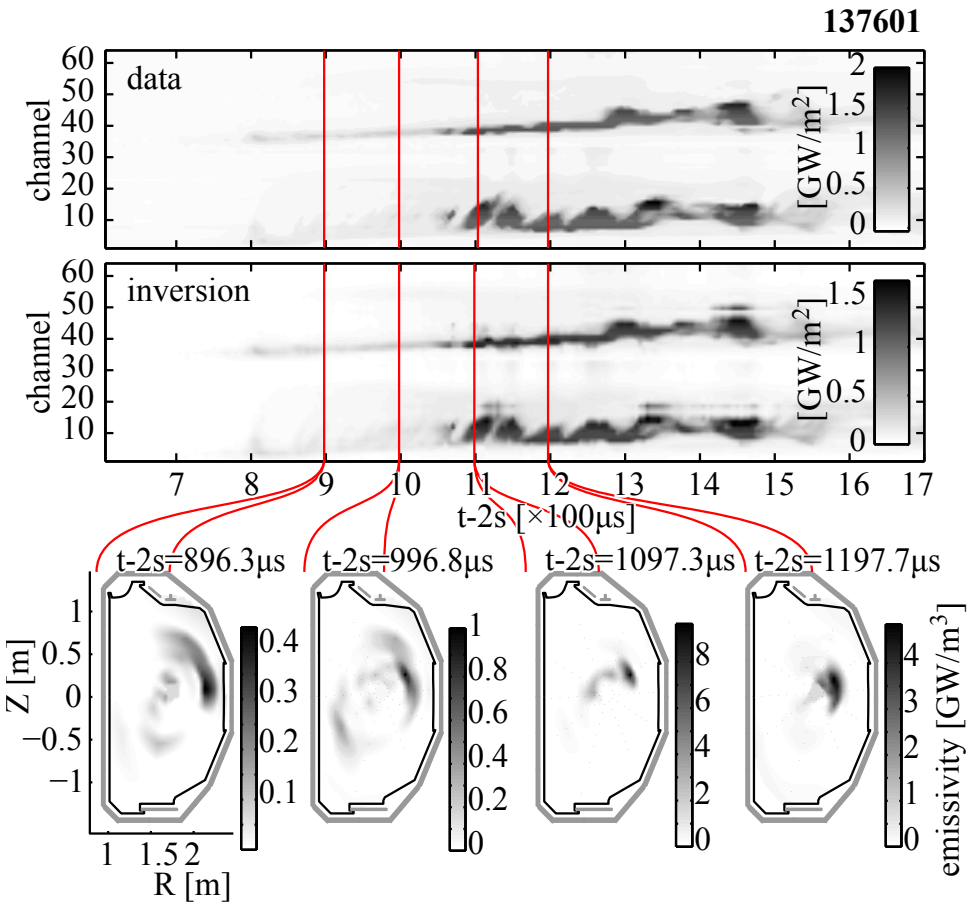

Figure 6.3: Tomographic inversion of an argon killer pellet shutdown at various times. Overview time histories are also shown of the data as prepared for inversion and the data reconstructed after the inversion, both of which look similar.

From this reconstruction, the thermal quench time dT/dt can be inferred from radiated power per unit volume P_{rad} by isolating it in equation 6.2:

$$P_{rad} = \frac{d}{dt}(nkT) = \frac{dn}{dt}kT + n\frac{d(kT)}{dt} \tag{6.2}$$

where n is the local density, and κ is the thermal conductivity. Neglecting the increase in density due to absence of fast 2D measurements and heat flow from nearby plasma, it is important to keep in mind that the result is an upper bound for the TQ time, which would be decreased by either of these. The resulting apparent TQ time is therefore quite fast considering the peak radiated power of

$P_{rad} \sim 10GW/m^3$ measured in the reconstruction shown in figure 6.3:

$$\frac{d(kT)}{dt} \leq \frac{1}{n} P_{rad} = 10GW/m^3/4 \times 10^{19} m^{-3} = 1.5keV/\mu s \tag{6.3}$$

$$\tau_{TQ} = kT/\frac{dkT}{dt} = 3keV/1.5keV/\mu s = 2\mu s \tag{6.4}$$

Dilution cooling can be included using interferometer measurements which show a line integrated density increase of $dn/dt = 10^{23} m^{-3}/s$. Using the NGS ablation rate of $\dot{N} \sim 10^{22} atoms/s$ into a spherical pellet cloud with radius of $\sim 10cm$, the local density increase is predicted to be roughly ten times larger $dn/dt = \dot{N}/\frac{4}{3}\pi r^3 \sim 10^{24} m^{-3}/s$. Using the larger of these density rises, the local density increase is predicted to dissipate thermal energy at a rate of:

$$\frac{1}{n}(\frac{dn}{dt}kT) \sim \frac{1}{4 \times 10^{19} m^{-3}}(10^{24} m^{-3}/s \cdot 3keV) = .075keV/\mu s \tag{6.5}$$

This additional thermal dissipation only slightly modifies the much larger radiative dissipation rate.

Assuming that parallel heat flow is large, the radiating flux tube volume effectively cools an entire annular region. This effectively extends the cooling time by the ratio of the annular shell volume V_{sh} to the radiating cloud volume V_{cld}. The radiating cloud is modeled as a cylinder of radius $r_{cld} \sim 10cm$ and length $L_{cld} < 2\pi R$ with a volume of

$$V_{cld} = \pi r_{cld}^2 L_{cld} \tag{6.6}$$

The cooled surface is modeled as an annular shell of minor radius r_{sh} and annular width of r_{cld}, so the volume is

$$V_{surf} = \pi((r_{sh} + r_{cld})^2 - (r_{sh} - r_{cld})^2) 2\pi R \tag{6.7}$$

The cloud length is here assumed to be half a circumference since the radiated power is measured an eigth of a circumference from the actual pellet (see figure 6.2), and the peak radiated power at the pellet is assumed a factor of two larger than measured. For $R = 1.67m$, and assuming $r_{cld} = 10cm$, $L_{cld} = \pi R = 5.2m$, and $r_{sh} = 0.67m$, the ratio of the radiating volume to the cooled volume is then:

$$V_{cld}/V_{surf} = \frac{r_{cld}}{4r_{sh}} \frac{L_{cld}}{2\pi R} \sim 0.02 \tag{6.8}$$

So assuming that the cooling processes don't change as the TQ proceeds, the predicted annular volume cooling time should be roughly fifty times slower than it would be if only the radiating volume was cooled, resulting in a thermal quench time of $\tau_{TQ} \sim 150\mu s$. This predicted time is a factor of 2-3 shorter than the measured volume averaged cooling time, suggesting that even with this oversimplified analysis, the annular cooling time is faster than the volume averaged cooling time. In localized regions where the plasma is cold the associated high resistivity could then cause voltages on faster timescales than a zero dimensional analysis would predict.

6.3 Inferring the loop voltage using magnetic diagnostics

This section discusses efforts to explore in-plasma loop voltages using magnetic measurements and inverse techniques. In section 6.3.1, loop voltages corresponding to changes in current and plasma motion are explored through Faraday's law, and estimated from simple measurements. Section 6.3.2 describes a class of observations which can be inferred using inverse techniques with magnetic diagnostics, and types of observations which are not possible due to non-uniqueness of the solutions. Results from codes using inverse techniques with magnetic diagnostics are presented and discussed in section 6.3.3.

6.3.1 Derivation of loop voltage for changing current from Faraday's equation

"In all fields, ... few know the theoretical aspect of things."

–The Kāma Sūtra

When current flowing in a loop changes in time either in magnitude or in position, a voltage is associated with that change in current through Faraday's induction equation. To derive this voltage, we begin with Faraday's equation, and

substitute the vector potential expression for the magnetic field: $\boldsymbol{B} = \boldsymbol{\nabla} \times \boldsymbol{A}$:

$$-\frac{\partial \boldsymbol{B}}{\partial t} = \boldsymbol{\nabla} \times \boldsymbol{E} = -\boldsymbol{\nabla} \times \dot{\boldsymbol{A}} \tag{6.9}$$

We then integrate over the surface enclosed by a toroidal loop:

$$\int dA \boldsymbol{\nabla} \times \boldsymbol{E} = -\int dA \boldsymbol{\nabla} \times \dot{\boldsymbol{A}}. \tag{6.10}$$

By invoking Stoke's theorem, this then becomes:

$$\int \boldsymbol{E} \cdot d\boldsymbol{l} = -\int \dot{\boldsymbol{A}} \cdot d\boldsymbol{l}. \tag{6.11}$$

Then integrating around the loop, and substituting the flux definition of the vector potential $A_\phi = \Psi/R$, we arrive at the loop voltage associated with a change in magnetic flux in the lab frame:

$$\begin{aligned} V_{loop} &= \int_0^{2\pi} R d\phi \hat{\boldsymbol{\phi}} \cdot \boldsymbol{E} \\ &= -2\pi R \dot{A}_\phi \\ &= -2\pi \dot{\Psi} \end{aligned} \tag{6.12}$$

By invoking the Green's function for the vector potential $\boldsymbol{A} = \int \mu_0 \boldsymbol{j}/4\pi|\boldsymbol{x} - \boldsymbol{x}'|d\boldsymbol{x}'$ the loop voltage can then be found directly from the current density following a similar derivation as in Jackson's 3rd edition [77], pg182, equation 5.37:

$$V_{loop} = 2\pi R \frac{\mu_0}{4\pi} \int \frac{\hat{\boldsymbol{\phi}} \cdot \dot{\boldsymbol{j}}_\phi}{|\boldsymbol{x} - \boldsymbol{x}'|} d^3x' \tag{6.13}$$

$$= -\int_0^\infty dR' \int_{-\infty}^\infty dz' M(R, z; R', z') \langle \dot{j}_\phi(R', z', t) \rangle, \tag{6.14}$$

where $\langle \dot{j}_\phi \rangle$ is the toroidal current density averaged along the toroidal loop, and $M(R, z; R', z')$ is the mutual inductance between two loops at (R, z) and (R', z'), defined as:

$$M(R, z; R', z') \equiv \mu_0 \sqrt{(R + R')^2 + (z - z')^2} \left[\left(1 - \frac{k^2}{2} \right) K(k) - E(k) \right] \tag{6.15}$$

with the simplifying definitions and elliptic integrals:

$$k^2 \equiv \frac{4RR'}{(R+R')^2+(z-z')^2}, \tag{6.16}$$

$$K(k) \equiv \int_0^{2\pi} \frac{d\theta}{\sqrt{1-k^2\sin^2\theta}}, \tag{6.17}$$

$$E(k) \equiv \int_0^{2\pi} \sqrt{1-k^2\sin^2\theta}. \tag{6.18}$$

Other authors [128], have shown that both positive and negative loop voltages occur around a constant current filament in motion.

This analysis does not describe what should *cause* such a voltage, only that some voltage V_{loop} (or equivalently an electric field) must be associated with an observed change in current $\langle \dot{j}_\phi \rangle$. Several causes for loop voltage spikes during rapid-shutdowns were discussed previously in section 6.1.

The above analysis describes the loop voltage associated with a stationary 'lab frame' point in space, but since the plasma is free to move in the vacuum region, the actual voltage in the plasma must be calculated by a convective derivative.

$$\hat{\phi} \cdot (\boldsymbol{E} + \boldsymbol{v} \times \boldsymbol{B}) = \eta j_\phi, \tag{6.19}$$

$$E_\phi = -\dot{\psi}/R, \quad \boldsymbol{B}_p = \boldsymbol{\nabla}\psi \times \boldsymbol{\nabla}\phi, \tag{6.20}$$

$$-(\dot{\psi} + \boldsymbol{v} \cdot \boldsymbol{\nabla}\psi)/R = -D\psi/Dt/R = \eta j_\phi, \tag{6.21}$$

In the limit that the resistivity goes to zero, this result describes the freezing of magnetic field lines into fluid elements of plasma (ie flux freezing). For finite resistivity (possibly including the effects of hyper-resistivity), this result describes the rate of dissipation of magnetic flux in the plasma, otherwise known as the loop voltage.

6.3.2 Limitations of magnetic diagnostics

Some plasma parameters cannot be directly measured, and must be inferred using inverse techniques. As described in section 3.4, the total plasma current can be measured directly using Rogowski coils:

$$I = \int \boldsymbol{j} \cdot \boldsymbol{dA}. \tag{6.22}$$

The plasma position, motion, and internal loop voltage cannot be directly measured however, but by making certain assumptions they can still be inferred using inverse techniques with arrays of external magnetic measurements including magnetic probes and flux loops. Magnetic (Mirnov) probes directly measure the magnetic field along the direction of the probe $\boldsymbol{a}_j$:

$$\boldsymbol{a}_j \cdot \boldsymbol{B_p}(\boldsymbol{r}_j) = \boldsymbol{a}_j \cdot \frac{1}{4\pi} \int_{V_p} \frac{\boldsymbol{j}(\boldsymbol{r_p}) \times (\boldsymbol{r} - \boldsymbol{r_p})}{|\boldsymbol{r} - \boldsymbol{r_p}|^3} d\boldsymbol{r_p}. \tag{6.23}$$

This is equivalently the gradient of magnetic flux. Flux loops enclosing an area A_j directly measure the enclosed magnetic flux from all current sources:

$$\psi_j = \int_{A_j} \boldsymbol{B_p} \cdot \boldsymbol{dA} \tag{6.24}$$

$$= \int_{A_j} \left(\frac{1}{4\pi} \int_{V_p} \frac{\boldsymbol{j}(\boldsymbol{r_p}) \times (\boldsymbol{r} - \boldsymbol{r_p})}{|\boldsymbol{r} - \boldsymbol{r_p}|^3} d\boldsymbol{r_p} \right) \cdot \hat{\boldsymbol{z}} dA. \tag{6.25}$$

The poloidal flux ψ can be inferred at all points in space by an inverse solution to this limited set of measurements. The poloidal magnetic field $\boldsymbol{B}_p = \boldsymbol{B}_R + \boldsymbol{B}_z$ and toroidal current j_ϕ can then be calculated at all points in space from the flux according to [165]:

$$B_R = -\frac{1}{R}\frac{\partial \psi}{\partial z}, \tag{6.26}$$

$$B_z = \frac{1}{R}\frac{\partial \psi}{\partial R}, \tag{6.27}$$

$$-\mu_0 R j_\phi = R\frac{\partial}{\partial R}\frac{1}{R}\frac{\partial \psi}{\partial R} + \frac{\partial^2 \psi}{\partial z^2}. \tag{6.28}$$

Unfortunately, the solution for the current density is non-unique without further constraining data [140, 106], so some form of constraining assumption is necessary. Inferences from these codes will be referred to as 'apparent' observations, since the observations appear as such but are not necessarily so; this is an important caveat of non-uniqueness. Two codes with different sets of constraining assumptions are used in these studies. One code, called JFIT [68], assumes that current runs in blocks of constant current density, that current is positively constrained, and further assumes spatial smoothness of the solution by regularizing the solution with singular value decomposition (SVD). The other code, called

EFIT [105], assumes that the current density must obey the Grad-Shafranov equation which can allow some regions of negative current, and further assumes spatial smoothness of the solution by fitting the current to a spline with a prescribed number of knots. Magnetic data fed into both codes is temporally smoothed by only $0.1ms$ so that high time resolution features can be extracted. These two codes are described further in appendix 3.9.

Since these assumptions are taken for granted in the following sections, it is important to keep in mind that if the assumptions become invalid at any point, solutions may still be found, but they could be non-physical. For example, solutions returned by JFIT do not necessarily satisfy a force balanced equilibrium, but solutions returned by EFIT always satisfy a force balanced equilibrium, even if the plasma is not actually in equilibrium. For another example, any currents with strong gradients in space cannot be inferred because of the spatial smoothness assumed; one hypothetical example of this scenario is the spatially localized thin annular region of high current density referred to as a 'shark-fin', which is predicted to occur during rapid-shutdowns [168].

Using these two codes, several inferred quantities differ substantially. The current profile solutions typically differ, however the magnetic field and poloidal flux solutions tend to be quite similar. The location of the point of minimum magnetic flux located near the geometric center of the plasma, called the magnetic axis, also can vary by over $10cm$ between the two codes. Additionally, the effective plasma inductance appears to differ. Despite these differences, certain phenomena consistently appear in both codes, and it is these phenomena which are discussed in the next section. For a brief comparison between the solutions returned by JFIT and EFIT, the flux function, poloidal magnetic field, and current density from both codes are shown in figure 6.4.

6.3.3 Inverse techniques for inspecting loop voltages before the current quench

Using the previously described inverse techniques, a loop voltage in the range of $1-2kV$ is inferred in the time between the end of the thermal quench (TQ)

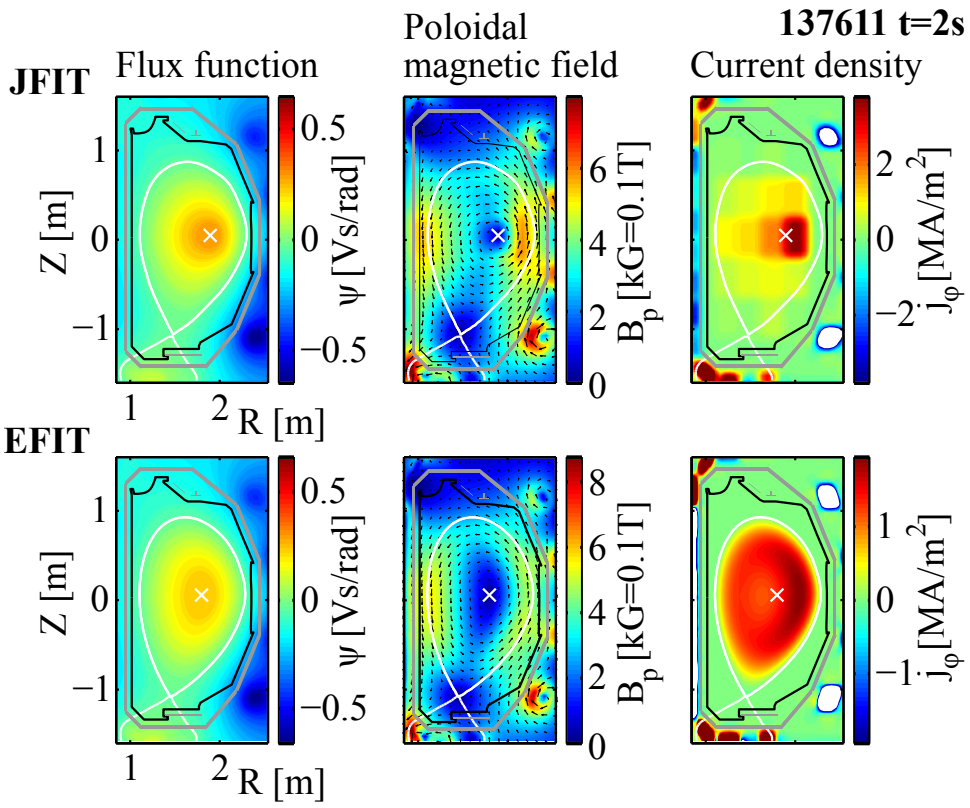

Figure 6.4: The flux function, poloidal magnetic field, and current density inferred using the codes JFIT and EFIT at a time just before a killer pellet shutdown.

and the beginning of the current quench (CQ). The peak of this voltage occurs near the end of the TQ, and the voltage remains above $1kV$ for roughly $0.5ms$ after which it returns near zero before the CQ begins. As discussed previously in section 6.1, these voltages are caused by increasing resistivity resulting from the pellet injection.

This loop voltage does not correspond to any observable significant current decay for a brief period before the CQ, but instead corresponds to an apparent current reorganization internal to the last closed flux surface (LCFS). The apparent reorganization can be described in terms of two primary changes: a current profile broadening, and a contraction in major radius of the current centroid. Current profile broadening corresponds to a drop in the normalized inductance ℓ_i, and is believed to result from overlapping of MHD modes. Contraction in major radius

of the current centroid is expected from the drop in normalized plasma pressure β_p during the TQ, which corresponds to a drop in the Shafranov shift [149].

The two codes JFIT and EFIT both predict a similar amplitude and timing of this apparent loop voltage, but there are also important differences between results from the two codes. The apparent inductance before shutdown inferred from the integral $L = 1/\mu_0 I^2 \int B_p^2 dV$, is roughly 25% larger from EFIT: $\sim 2.5\mu H$, compared with $\sim 2\mu H$ from JFIT, as shown in figure 6.5c. While the apparent voltage is roughly $500V$ larger as predicted by EFIT than by JFIT as shown in figure 6.5d, the noise level of the apparent voltage from EFIT is roughly $500V$, compared to roughly $50V$ for JFIT, so apparent voltage from both codes is equivalent within the noise. The duration of the apparent voltage appears to last almost $1ms$ based on the EFIT result, while it is only $0.5ms$ based on the JFIT result.

For some readers, the inductive voltage in terms of changing current and inductance will be easier to understand than changes in flux. The voltage can be equivalently expressed as $V = -LdI/dt - IdL/dt$, where the second term is less familiar since most inductors do not change substantially in time. As seen by comparison of figures 6.5c and 6.5d, the apparent voltage inferred in this way is roughly equivalent to the apparent voltage inferred from the convective derivative of flux on the magnetic axis $-D\psi_0/Dt$.

A notable feature of the apparent loop voltage in two dimensions is that it is only positive on the low field side of the vessel, and on the high field side the apparent voltage is negative, shown as blue regions for $t = 2.0012s$ and $t = 2.0015s$ in figure 6.5d and e. The sign of the apparent voltage in these two regions can be understood using the principle of induction. When the current moves inward in major radius, the high field side current effectively increases, while the low field side current effectively decreases. Voltage is induced to oppose this change in current, resulting in the respective sign of apparent voltage on the high and low field sides of the machine. The voltage measured on a flux loop outside of the vacuum vessel on the inboard side, shown in figure 6.6b, confirms that a reversed voltage occurs on the inboard side shortly after the TQ. This spatially localized reversed apparent voltage only occurs between the TQ and the CQ, during the

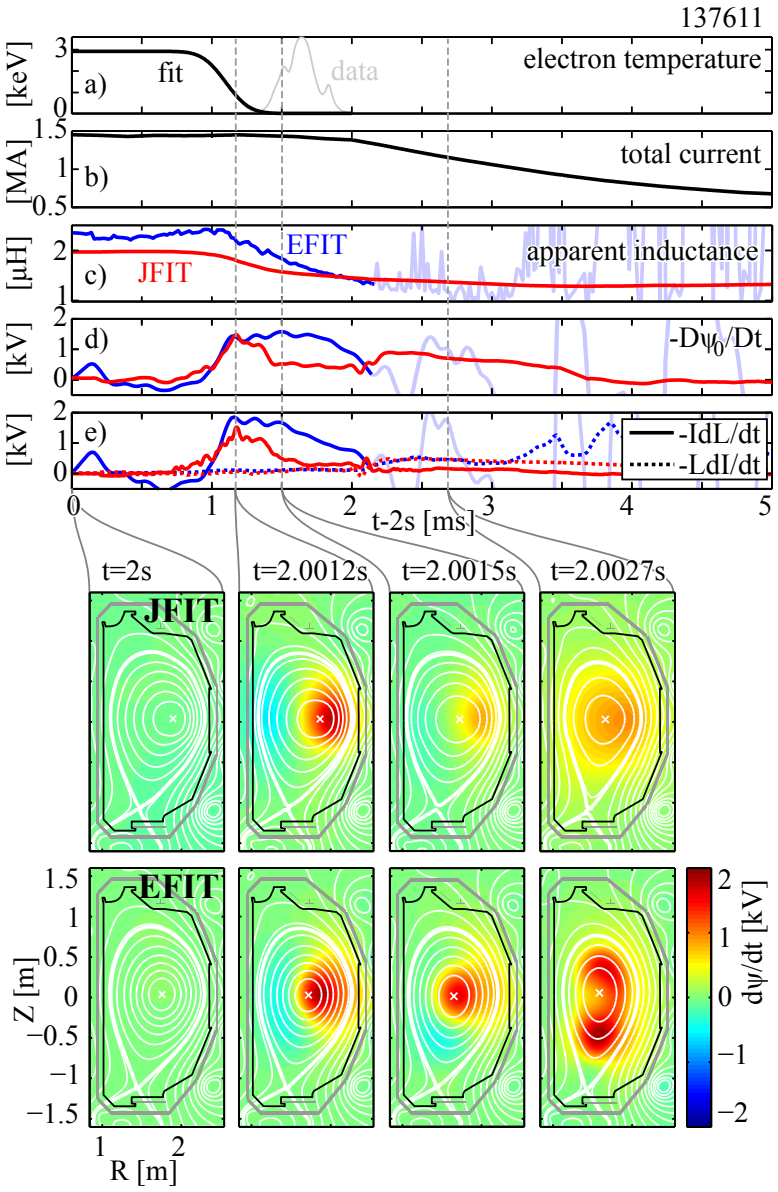

Figure 6.5: Results from analysis of loop voltages during a shutdown using the codes JFIT and EFIT. a) Electron temperature and b) total current are shown for timing reference, along with the c) apparent inductance and (d, e and lower panels) the apparent voltages inferred from either code using several techniques. Quantities inferred from EFIT are lightened where convergence failed.

CQ the apparent voltage is positive at all locations as shown at $t = 2.0027s$ in the bottom of figure 6.5. The physical mechanism for the current moving inward in major radius is believed to be a combined reduction of the Shafranov shift as

the plasma cools, and also an excess vertical field as the plasma current begins to resistively decrease.

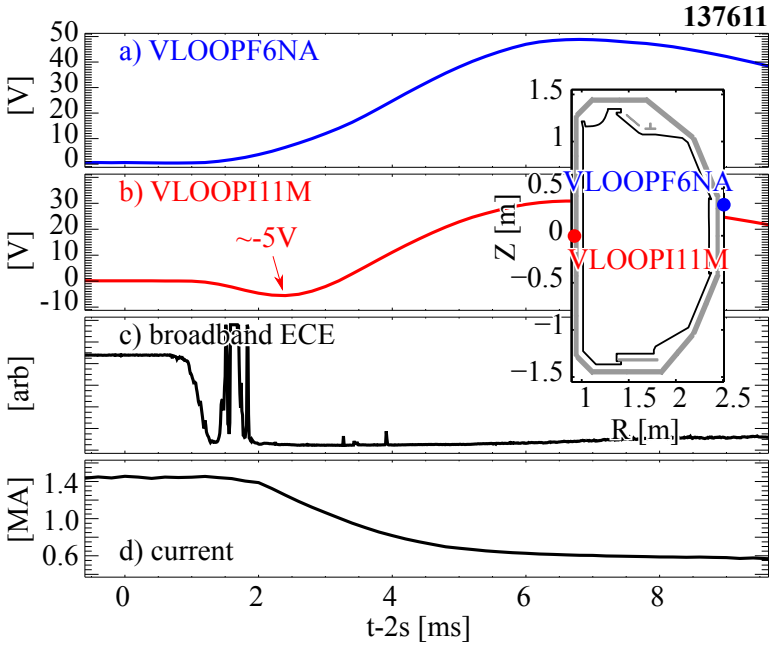

Figure 6.6: Voltages measured directly on flux loops located on the a) outboard and b) inboard sides of the vacuum vessel near the midplane, with c) broadband ECE shown for a TQ timing reference and d) plasma current shown for a CQ timing reference.

The misfit χ^2 for both codes rises during CQ. It is important to note that EFIT suffers from problems with numerical convergence $2ms$ after the shutdown is triggered, so results from EFIT after $2ms$ are non-physical. The convergence error in EFIT remains similar to pre-shutdown-trigger levels before $2ms$, indicating that the Grad-Shafranov equilibrium model still reasonably matches the plasma conditions until this time, as shown in figure 6.7. Around $2ms$ after the shutdown is triggered, the fitting error increases by roughly two orders of magnitude in EFIT, and not quite one in JFIT. This increase of fitting error suggests that the Grad-Shafranov equilibrium model may no longer represent the plasma conditions at that time.

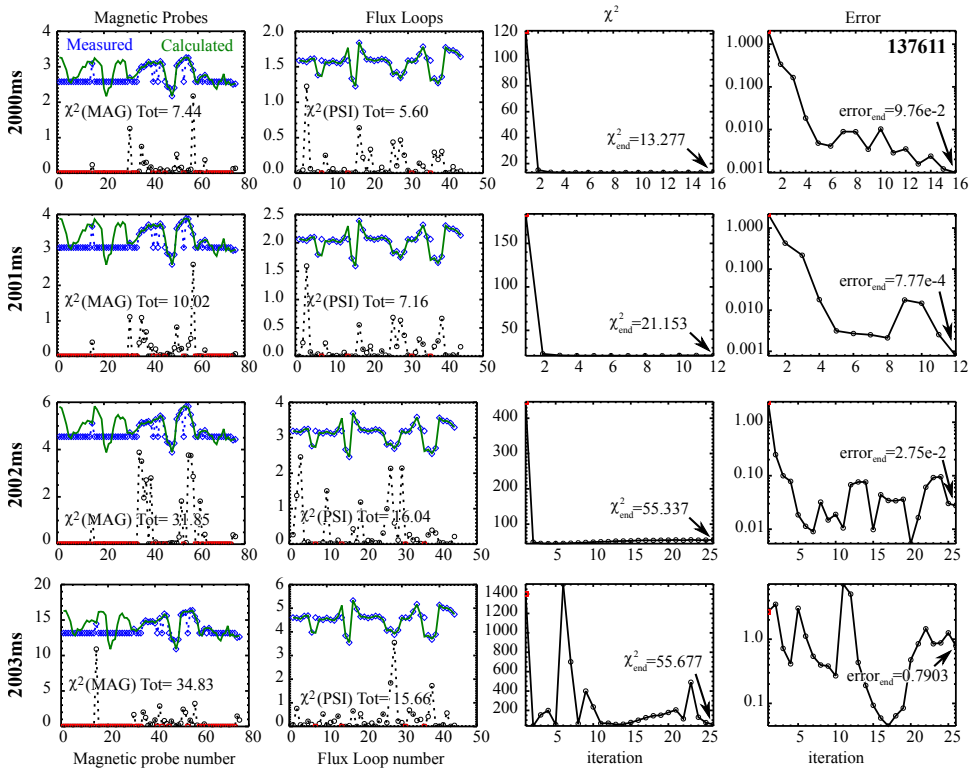

Figure 6.7: Fitting quality and convergence results from EFIT showing error increasing after $2ms$ after a shutdown.

6.4 Conclusions

Fast diagnostics and inverse techniques for considering the apparent loop voltages in the time between the thermal quench and current quench were discussed. The Spitzer resistivity and hyper-resistivity were briefly reviewed, along with some prior zero-dimensional modelling to establish context for resistivity spikes during rapid-shutdowns and associated loop voltage spikes. Tomographic reconstruction of radiated power during a killer pellet injection was presented, featuring a peak spatially localized radiated power of $10GW/m^3$, and suggesting a localized thermal quench rate faster than the global average. Apparent loop voltages were presented and discussed from the codes EFIT and JFIT, featuring peak voltages in the range of $1-2kV$ which occurred before the global current quench commenced. This apparent voltage has not been previously invoked in the con-

sideration of runaway electron generation, and so may contribute to an increased generation of runaways during rapid thermal quenches.

Chapter 7

Conclusions and outlook

"Nobody ever finishes their PhD thesis, they just stop working on it."

–Graduate student proverb

Runaway electrons (RE) remain one of the largest hazards and obstacles to the future of producing energy via nuclear fusion in tokamaks. With larger test tokamaks such as ITER on the horizon, it is critical that these issues be resolved before they interfere with operation of these machines.

The scintillator array described in chapter 3, represents only a small advance in the types of measurements necessary to fully understand RE phenomena. Measurement of the average de-confined RE energy enabled by the array is an improvement, but an in-situ diagnostic of the RE energy distribution function with high energy resolution near the thermal range and perhaps reduced energy resolution up to the synchrotron limit would help to understand RE kinetics during rapid shutdowns. Coarse measurement of the spatial distribution of RE de-confinement revealed new clues about how and when RE are lost throughout the shutdown, but higher spatial resolution will be necessary to identify specific hazard zones within the tokamak. X-ray cameras may be more useful than external scintillator arrays for such high resolution imaging.

Results from the new scintillator array diagnostic were described in chapter 4. These results agree with simulations of plasma shutdowns in certain respects including: the strike points of RE during the prompt loss phase and the presence of a rotating mode causing some RE deconfinement. Experimentally observed toroidal

asymmetries in the de-confinement predicted during the prompt loss appear to contradict the toroidally symmetric de-confinement predicted by NIMROD simulations. While apparent instabilities were observed during the RE plateau and the final abrupt termination of the plateau, further work is required to identify the physical mechanisms behind these instabilities, perhaps including runaway (Yoshida) equilibrium stability analysis.

Diagnostic pellet injection experiments were discussed in chapter 5. These revealed that enough RE flux exists well beyond the last closed flux surface during RE plateaus to disintegrate the injected pellets. While sufficient RE flux existed to disintegrate the pellet, the RE flux was too small to generate a detectable amount of x-ray emission. Brief bursts of electron cyclotron emission (ECE) and visible range continuum emission were observed when the pellet disintegrated. Further study of RE transport and RE/material interactions will be critical for understanding the design requirements for armored wall tiles in future experiments and reactors, and future studies of the ECE bursts from the pellet may also improve our understanding of the RE/pellet interaction.

The localized peak radiated power and apparent loop voltages during rapid shutdowns were inferred using inverse techniques in chapter 6. Peak radiated powers in the range of $10GW/m^3$ were reported in the vicinity of the injected pellet. Apparent loop voltages of $1-2kV$ were larger than previously predicted during rapid-shutdowns, and occurred earlier than the simplest source of voltage during a rapid shutdown: the inductive current decay. Inverse techniques are not used frequently for the analysis of apparent loop voltages during rapid-shutdowns, so future work is necessary to confirm the validity of these techniques. The results of these analyses may also be useful for comparison with models of rapid-shutdowns to confirm predictive capabilities for future experiments.

Appendix A

Table of symbols

Numerous symbols are used throughout the thesis, and are listed here for reference.

Symbol	Description
A	Atomic number or vector potential
a	Toroidal minor radius
$\alpha \sim 1/137$	Fine structure constant
B_p, B_T	Poloidal magnetic field and toroidal magnetic field
$\beta \equiv v/c$	Normalized relativistic velocity
β_p	Normalized plasma pressure
c	Speed of light
C_f	Feedback capacitance
δ	Electromagnetic shielding thickness
dW/dz	Stopping power
$\epsilon_A \equiv E/E_A$	Avalanche normalized electric field
$\epsilon_D \equiv E/E_D$	Dreicer normalized electric field
ε_0	Vacuum permittivity, aka electric constant
E, E_A, E_D	Electric field, Avalanche electric field, and Dreicer's electric field
f_r, f_{pe}, f_{ce}	Right-handed cyclotron cutoff frequency, electron plasma frequency, and electron cyclotron frequency

Continued on next page...

Continued from previous page.

Symbol	Description
F_{syn}	Synchrotron drag force
$\gamma \equiv m/m_0$	Normalized relativistic mass
γ_A, γ_D, γ_H	Runaway electron growth rates due to avalanche, Dreicer, and hot-tail mechanisms
$h = 2\pi\hbar$	Planck's constant and Dirac's constant respectively
I_m, I_t, I_r, I_v	Total measured, thermal, runaway, and vessel currents
j	Current density
κ	Elongation
L_t, L_r, L_v	Thermal, runaway, and vessel inductance
λ	Wavelength
λ_{De}, λ_B	Debye length and de Broglie length
m, m_e	Mass and electron rest mass
M	Mutual inductance
μ	Total attenuation cross-section
μ_0	Vacuum permeability, aka magnetic constant
μ_r	Relative permeability
n, n_e	Number density and electron density
N_A	Avogadro's number
ϕ	Toroidal angle or phase
ψ	Poloidal magnetic flux
ψ_0, ψ_l	Poloidal magnetic flux at the magnetic axis and at the last closed flux surface
q_{95}	Safety factor at 95% of poloidal flux
R	Toroidal major radius
R_f	Feedback resistance
R_t, R_v	Thermal and vessel resistance
ρ	Mass density
σ	Electrical conductivity

Continued on next page...

Continued from previous page.

Symbol	Description
t	time or thickness
T_e, T_i	Electron and Ion temperature
τ_{CQ}, τ_{TQ}	Current quench and thermal quench timescales
τ_{RC}	Decay time of an RC filter
θ	Poloidal angle
V	Volume or voltage
V_{loop}	Loop voltage
v	velocity
W_k	Runaway electron kinetic energy
W_γ	Photon energy
W_m	Magnetic energy
W_t	Plasma thermal energy
Z	Atomic charge
Z_{eff}	Effective charge state

Table A.1: A listing of the numerous symbols used throughout this thesis.

Appendix B

History of runaway electron observation in DIII-D

The table in this chapter was produced by scouring the DIII-D database for shots exhibiting a hard x-ray burst in a neutron counting scintillator after a current quench begins. These x-ray bursts are associated with runaways striking the wall since thermal neutron production ceases before the current quench begins.

Run	Shots	Experiment title
19951201, 4, 5, 7	87834, 52, 7, 78, 91, 3, 944, 54	Investigation of Beta Limits and Extension of the Duration of High Performance, Negative Central Shear Plasmas
19960322	88983, 95	Confinement and stability in single null discharges with NCS, Day 3
19960621	90210, 13, 5-7	Argon "Killer" Pellet and DiMES Experiments for ITER
19970515	91979	Steady-state discharges in square shapes, day 2
19980226	95172, 4-6, 80, 2, 3, 7, 8, 91, 2	Runaway Electron Experiment
19980302	95240	Kink mode stabilization by resistive wall

Continued on next page...

Continued from previous page.

Run	Shots	Experiment title
19980618	96770,1	Disruption mitigation studies (Ar KP)
19990111	97794	Physics of Rotational Stabilization of the Resistive Wall Mode
20000608	103161	Error field correction optimization at qmin>1
20010207	105288, 91	Performance at Higher qmin
20010618	107621, 7	RWM stabilization at twice the no-wall limit
20010626A	107844(Ar), 51(Ne)	Disruption mitigation with gas puff (argon & neon)
20020130	109167, 9	Critical rotation for RWM stabilization
20020308	109873, 87, 93	Shafranov stabilitiy in ITB plasmas
20020313	109969, 70	Test and expand wall stabilization limits
20020322	110215	Disruption mitigation with triggers (neon)
20030203	112447	Day 1 - Plasma Startup and Systems Checkout
20030213	112679, 83	Startup - Vessel conditioning, plasmas in reverse BT
20030404	113522	Plasma Starup & Cleanup Day 3
20030407A	113548, 50, 2	I-coil frequency scan (MHD spectroscopy)
20030430	114012	QH-mode in co-injected discharges
20030602	114361, 5	Improved error field correction using new I-coil
20030616	114702, 8	100% non-inductive operation at high beta using off-axis ECCD
20030617	114719, 26, 40	Effect on achievable beta of density profile broadening
20030619A	114819	RWM Feedback with the I-coil
20030723	115323	High betaN sustainment using flat q-profile scenario
20030725A	115406	Higher betaN sustainment using flat q-profile scenario

Continued on next page...

Continued from previous page.

Run	Shots	Experiment title
20030801	115508, 10, 2, 3, 27	Gas jet penetration studies (argon & neon)
20030908	115838, 42	First test of n=2 braking for rotation control
20030919	116133	Fast Wave Coupling to Advanced Tokamak Discharges
20040323	117437, 9, 40-4	Gas jet imaging for disruption mitigation (neon, LSN)
20040408A	117829	Resonant field amplification at low rotation
20040415	117974	Shafranov shift stabilization scans in H-mode plasmas
20040519A	118613	Cross-device rwms with JET
20040624	119079	Pedestal Stability- Ip ramps and localized fueling
20040625	119127	FW Coupling and Profile Control in AT Plasmas
20040726	119632, 41	RWM feedback tool deveopment and FB demonstration
20040727	119664, 71, 3	Develop high betaN , flat q-profile scenario
20040802	119796, 9, 803-5, 16, 17	Formation and Sustainment of Current Hole Plasmas
20040803	119848	Extend n=3 I-coil ELM suppression to higher BT and Ip at Lower ne
20041018	120738, 9, 41, 3, 5-9, 51, 3	Massive gas puff
20041025	120864	q-profile dependence of RWM stability
20050204	121810	q-profile dependence of RWM rotation threshold
20050214	122027	Develop long duration, betan>4 discharges

Continued on next page...

Continued from previous page.

Run	Shots	Experiment title
20050217A	122160	RWM Stabilization with Audio Amplifiers
20050309	122432, 3	Plasma Startup and Systems Checkout
20050314A	122518	Disruption Mitigation
20050325B	122826	disruption mitigation
20060516	124426	Plasma Checkout, Day 1
20060517	124429, 41, 4	Plasma Conditioning, Day 2
20060518	124449	Plasma Startup and Systems Checkout - Day 3
20060531	124715	Plasma Startup and Systems Checkout - Day 8
20060808A	126057	Advanced Tokamak Shape Optimization
20070329	128287	Feedback control of ELM-driven RWM
20070719A	129702, 6, 9	Disruption mitigation with medusa valve
20070808A	130157, 60	Disruption mitigation with medusa valve
20090529	137600-21,23-5	Characterize runaway electron generation and transport (Ar KP)
20090724A	138517-9, 21-22	Deconfinement of Runaway Electrons With RMPs (Ar KP)
20091209	140564-6, 8, 71-89	RE generation, PS pellet injection
20100212	141733-49, 51-60	Control of runaway electron current channel in DIII-D
20100405(A)	142661-92	Control of runaway electron current channel in DIII-D / RMP Suppression of Runaway Electrons
20100406	142707-16, 20, 23, 25-33	Impurity injection into runaway electron beam

Table B.1: A non-exhaustive DIII-D shot history of runaway electron observation demonstrating the wide variety of experiments which can generate runaway electrons.

Appendix C

Pellet injector

The pellet injector used in these studies was a re-creation [73] of the injector originally developed at MIT for the Alcator C-Mod tokamak [46]. During preparation and use of the lithium pellet injector hardware at DIII-D for the present experiments, a number of repairs and modifications were made to the injector to improve operation, all of which are documented below.

C.1 Repairs

When first restarting the injector many component systems had failed, presumably due to neutron damage of electronics though this was never confirmed.

Failure of numerous modules of the Texas Instruments 505 programmable logic controller were attributed to neutron damage. While replacement modules were available through Siemens who purchased the PLC line from TI, these replacement modules also failed occasionally during two years of operation, requiring further replacement.

Photodiode detectors, light emitting photodiodes, and other semiconductor based electronics are gradually degraded by neutron damage [118, 47, 20] often resulting in their eventual failure. The optical isolators used to disengage interlocks in the turbo pump controllers failed apparently due to such degradation, but otherwised powered on fine. Replacement of the turbo controllers repaired the problem. The light emitting diode used for position indicating of the pellet injec-

tor loading wheel had dimmed so much that it no longer triggered the receiving PMT detector. After replacing the LED, the receiver was saturated due to the high intensity, so a $1k\Omega$ potentiometer was inserted in-line with the LED to adjust the LED brightness, which repaired the problem. A minor fire hazard resulted from a failed stepper motor controller which no longer limited current and instead passed through full current available from the power supply, and burned out the motor used to advance the pellet wheel. Future hardware should be screened for such short-circuit failure modes to prevent these fire hazards. Replacement of the stepper motor and controller repaired the problem, though a similar failure could occur in the future.

The pneumatic valves used to actuate vacuum system gate valves by the PLC occasionally stuck. Replacement of the failed valve repaired the problem, though servicing with lubrication could have also repaired the problem.

A short and burned winding was discovered in the variac used to control the output voltage in the high voltage power supply used for actuating the fast gas valves, with no other apparent problems in the supply. No replacement variac or power supply was available, so the winding was repaired and the power supply operated normally afterwards.

Multiple limit switches for the gate valves failed to open and close smoothly, so that the PLC could not tell whether a gate valve had been closed or opened. Where possible these were repaired, but in some instances the limit switches could not be repaired and so had to be bypassed in the PLC logic to enable operation. When these switches were bypassed, the PLC logic was amended to rely on convectron gauge states for vent and pumpdown.

During transportation of the injector between the diagnostics lab where it was stored and the DIII-D pit, some leaks developed in the vacuum system. They were located with a leak checker, and after replacement of copper gaskets on the relevant flanges, the leaks were repaired.

One moderate leak was located after relocating in the DIII-D pit, between the low vacuum turbo roughing line and the downstream gate valve, but was never repaired since it did not effect normal operation. Occasionally the gate valve

would close due to pressure transients exceeding multiple torr from the ORNL pellet injector which shares the roughing lines, in which case the pressure buildup behind the gate valve was exacerbated by this leak. Repair of this leak would be optimal, but operation was possible with it since it existed only on the roughing side of the system. Addition of a connection between the low vacuum and high vacuum roughing lines with a gate valve to enable isolation from these pressure transients while maintaining the ability to pump down from full atmosphere into the low vacuum roughing line would be desirable.

The pellet injector vacuum system is diagrammed in figure C.1 for reference of the mentioned components.

C.2 Modifications

The pellet injector was re-installed at a location farther from DIII-D than the original design due to the existence of new hardware in the old location. This required addition of a curved pellet guide tube to deliver pellets into the new port location. The tube was fabricated with two bends in a $20ft$ long section of $1/2in$ outer diameter $3/8in$ inner diameter extruded non-magnetic stainless steel tubing with a nominal radius of curvature about $7m$. Cheaper welded tubing was avoided since discontinuities from welds might disturb pellet transit. The tube was bent over the top of the $10000gal$ liquid helium dewar in the DIII-D yard, which had a similar radius of curvature. Vacuum flanges were then welded to either end of the tube, and its effect on pellet time of flight and various materials was tested in the lab. These results are recounted in section C.3 on pellet material selection.

The pellet injector began to jam at one point due to a constriction at the throat of the firing tube headers from $0.089in$ to $0.076in$ which caught pellets before they had acquired much velocity. The pellets were nominally sized $0.072in$, however they could rotate in the larger orifice such that they presented a larger diagonal diameter than the $0.076in$ constriction. A sketch of the jamming condition is shown in figure C.2 Previous experiments used brittle wax pellets which would have broken apart in these constrictions, but the present plastic test pellets jammed

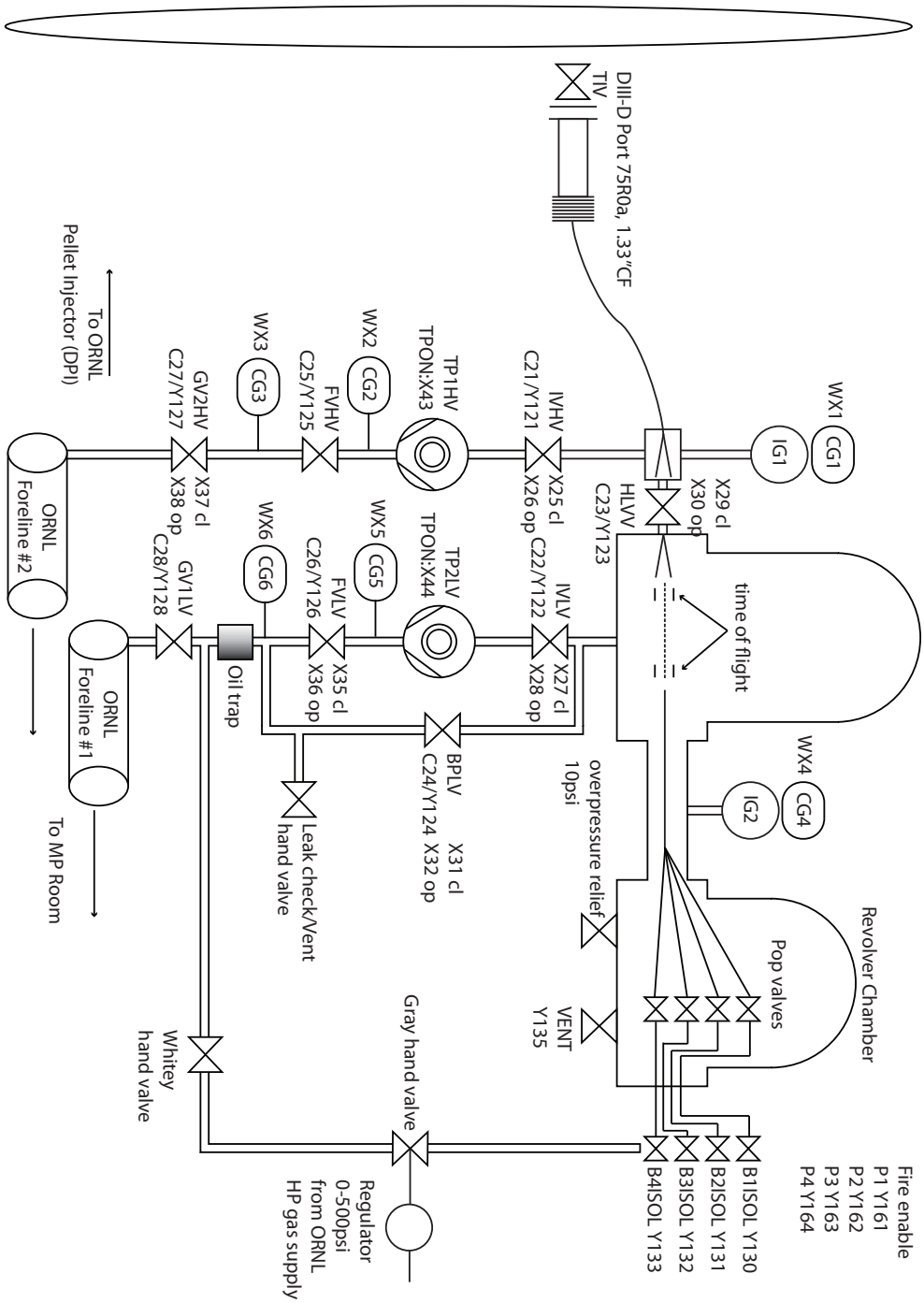

Figure C.1: A diagram of the impurity pellet injector vacuum system.

firmly and had to be manually cleared. Clearing the jams required venting the injector, removing both bell jars and the pellet wheel, then inserting a thin wire down each barrel to clear any jam. The up-range side of each firing tube header was sanded lightly to remove the leading edge of this constriction, but the trailing edge was necessary to stop the firing tubes. A set screw was also added to each firing tube header so that the tube would remain firmly seated, to minimize the chance of further jams. After these modifications the injector ceased jamming.

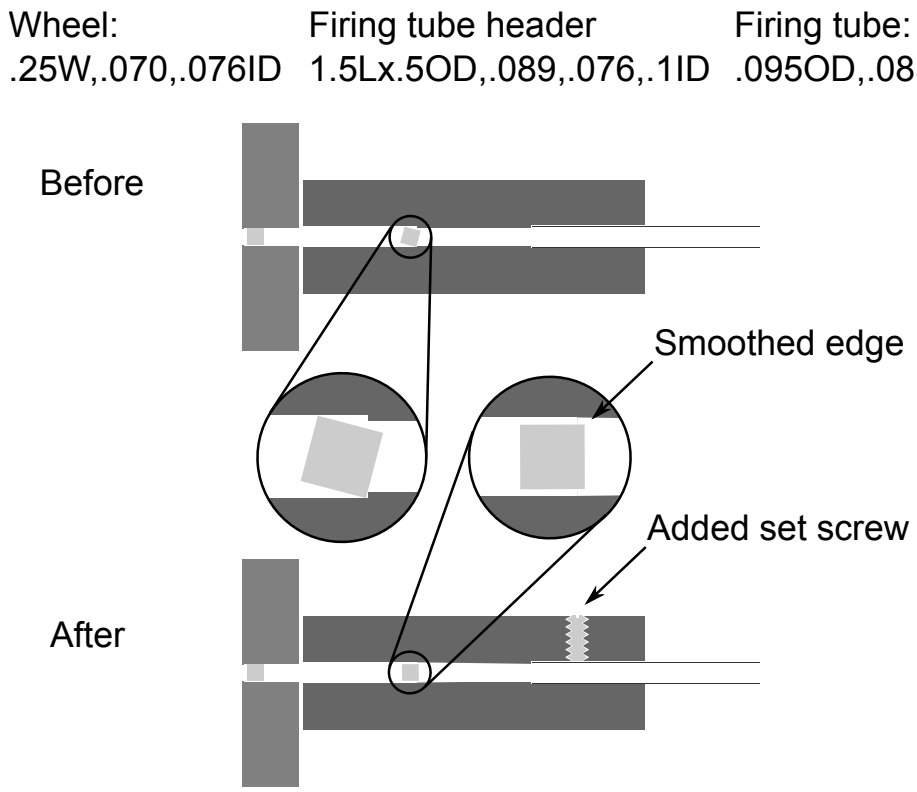

Figure C.2: A sketch of the pellet jamming condition and modifications made to eliminate jamming.

After it became apparent that a significant fraction of misfired pellets were lost due to impact on the side of the pellet catchers located on the down-range side of the propellent gas expansion chamber, an adjustable rig was built so that each pellet firing tube could be aligned independently onto the center of the pellet catcher and a redesign of the pellet catcher was done to provide a larger aperature. Installation of the new catcher required moving the position of the down-range light

gate used for time of flight measurements, so that the time of flight length changed to 270mm. Drawings of these new components are shown in figure C.3.

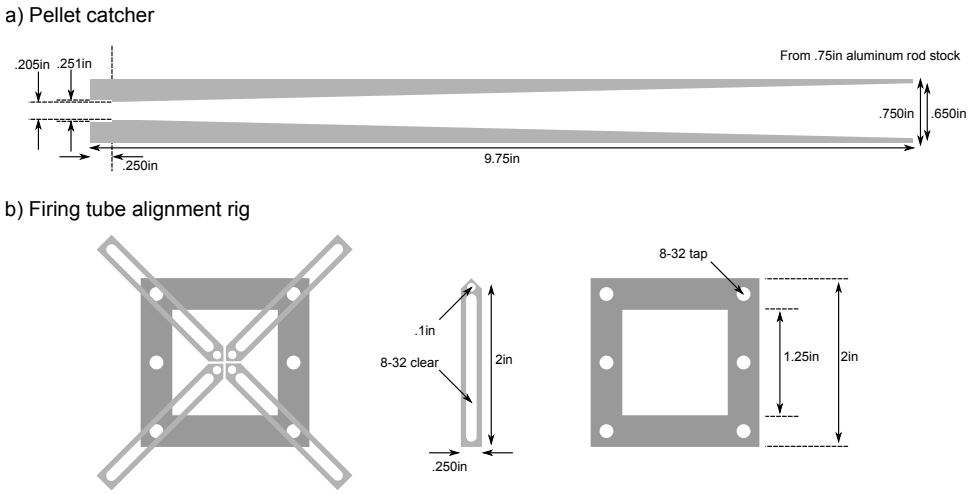

Figure C.3: New parts installed on the pellet injector including a) larger diameter bore pellet catchers and b) an alignment jig.

In addition to the previously discussed modifications to the PLC logic to accomodate gate valve failed limit switches, and somewhat regular replacement of failed modules, progress was made on completing the PLC programming for vent and pumpdown of the vacuum system. While switches were previously installed in the electronics cabinet to control these functions, the corresponding wiring and programming to control the pumpdown and vent sequences was not completed. This topic was low enough priority however that the work was not completed, and manual vacuum system operation was carried out with the assistance of a written procedure to aid operators.

C.3 Pellet material selection

While testing was generally done using pellets punched out of the red dyed LDPE plastic caps which shield vacuum flanges during shipping, this material was deemed unsuitable for use by the vacuum committee due to the unknown composition of the red dye. The vacuum committee approved easily carbon or

simple hydrocarbon plastics, so a variety of these materials were tested.

Pure carbon was initially the most desirable pellet material, since modelling of pure elements is simpler than complicated molecular compounds. Two forms of carbon pellets were tested: amorphous ATJ graphite cylinders, and vitreous carbon spheres. Cylinders were machined on a lathe from graphite rod stock, which required a vacuum operating to remove graphite dust and small custom tools to machine and collect the pellets. Spheres of various sizes were ordered in a small bin, and coarsely sorted using a set of precision seives, then specifically picked over for a nominal diameter of $0.072in$ while rejecting occasional aspherical samples. After loading and test firing these pellets, they often triggered both light gates but rarely triggered the microphone at the end of the guide tube and when they did the trigger times varied by multiples of the average time of flight, resulting in poor timing predictability. By using a fast framing camera to observe the pellets exiting the guide tube into a cube with attached windows, the cause was determined to be shattering of the pellets. While graphite is a well known lubricant in the presence of moisture, it becomes an abrasive in the dry vacuum conditions and travels poorly through the guide tube, grinding and breaking to pieces along the way. The spherical pellets were also observed to have rolled out of the pellet wheel onto the floor of the injector after loading, making their future use questionable. For these reasons carbon was rejected as a pellet material.

After failure with carbon, polyethylene and polystyrene plastics were tested. Pellets were again machined from rod stock using the same small custom tools, with polystyrene machining cleanly, but polyethylene often gumming up the tools. Both pellets performed similarly well in bench tests, with a standard deviation for time of flight close to a tenth of the mean, enabling excellent timing predictability. Due to the simpler machining of polystyrene, this material was selected for typical use. Time of flight tests were carried out using the new tube by timing the delay between pulses from a gate situated near the firing tubes and a microphone strapped to a closed blank flange at the end of the guide tube. Results from these tests are shown in figure C.4

Complications from the molecular composition of these plastic pellets made

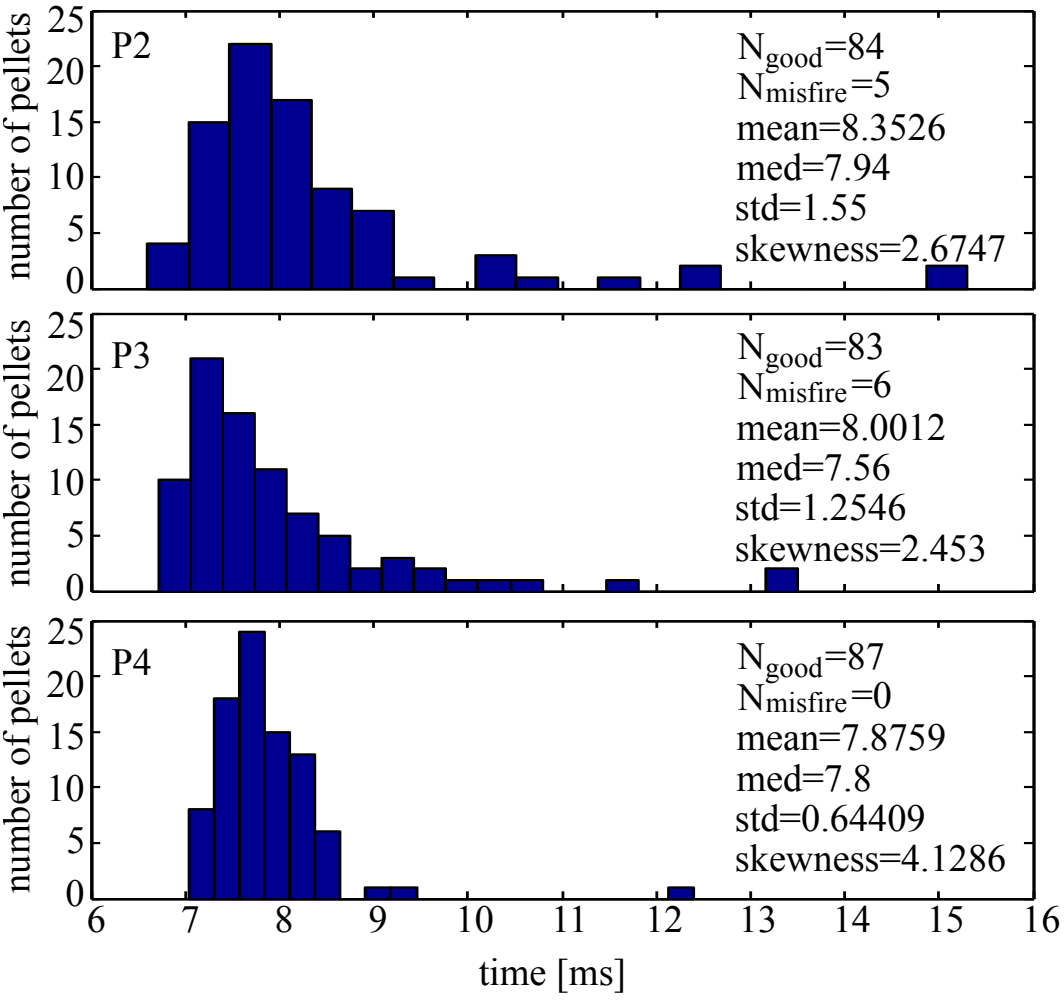

Figure C.4: Timing histograms for $d = 2mm$ polystyrene pellets fired along the curved guide tube in a mockup test.

reverting to some form of elemental carbon once again desirable. To prevent carbon pellets from shattering during transit in the guide tube, it was proposed that a thin layer of polypropylene be deposited on pellets to protect the pellets during flight since the layer would burn off rapidly, leaving the carbon behind. This pellet design was not fabricated or tested.

Appendix D

Comparison of various techniques for calculating runaway current due to avalanche

On timescales much longer than the current quench (CQ) time, any remaining current is typically attributed entirely to runaway electrons (REs), however the amount of current carried by REs during the CQ, and even at the beginning of the CQ, is a slightly less simple inference. In this appendix, various techniques are described for calculating RE current due to the avalanche mechanism. Section D.1 discusses three empirical techniques for calculating RE current from experimental data. A coupled inductor model is discussed in section D.2 and compared with the empirical techniques. In section D.3, the amount of initial RE seed current is calculated based on the final measured RE current and the integrated loop voltage.

D.1 Empirical techniques

Calculation of runaway electron current in disruptions has previously followed [35] the following simple algorithm, the results of which are shown in red on figure D.1:

- Assume runaway current begins evolving at the peak of $-dI/dt$, which is

roughly in the middle of the current quench

- Assume thermal current continues to decay at the inductive rate measured during this peak: $I_{L/R} = I_0 e^{-t\gamma_{CQ}},\ \gamma_{CQ} = max(-dI/dt)/I$
- Runaway current is then calculated as the subtraction of measured current and this decay: $I_r = I_p - I_{L/R}$

However, the actual growth of runaway current should be faster than this due to avalanching runaway current shorting out the inductive electric field, but treatment of this effect requires a density measurement to calculate the avalanche rate γ_{av}, defined below. An upper bound to the runaway current would be assuming that the thermal current decays at the sum of the inductive rate $\gamma_{L/R}$ and the calculated avalanche rate, but this falsely assumes that all current is initially runaway current. This technique is shown as the green lines on figure D.1. A more correct technique involves allowing the thermal current to decay at the sum of the measured inductive rate plus the avalanche rate multiplied by the ratio of runaway current to total current $\gamma = \gamma_{L/R} + \gamma_{av} I_r/I_m$. This technique is shown below as the blue lines on figure D.1. After several CQ times, all three models agree, so these more complicated techniques need only be considered when the quantity of RE current at early times is important.

D.2 Coupled inductor model

A model of runaway electron avalanche is also considered here for comparison with the above techniques for inferring RE current from measured current. During the current quench phase, the electric field exceeds the critical value for avalanche $E_{av} = V_{av}/2\pi R = n_{e\star} e^3 ln\Lambda/4\pi\epsilon_0^2 m_e c^2$, hence confined runaway seed current can exponentially multiply at a rate of [145] $\gamma_{av} = (V/V_{av} - 1)\gamma_0$, through the avalanche process into a relativistic current plateau. The quantity $\gamma_0 = 1/2\tau_A ln\Lambda$, where $\tau_A = m_e c/eE_{av}$ and $E_{av} = 0.14V/m$ for $n_{e\star} = 4 \times 10^{14} cm^{-3}$ which are typical values during the current quench. These values for γ_0 and E_{av} are assumed constant throughout the current quench in the model below.

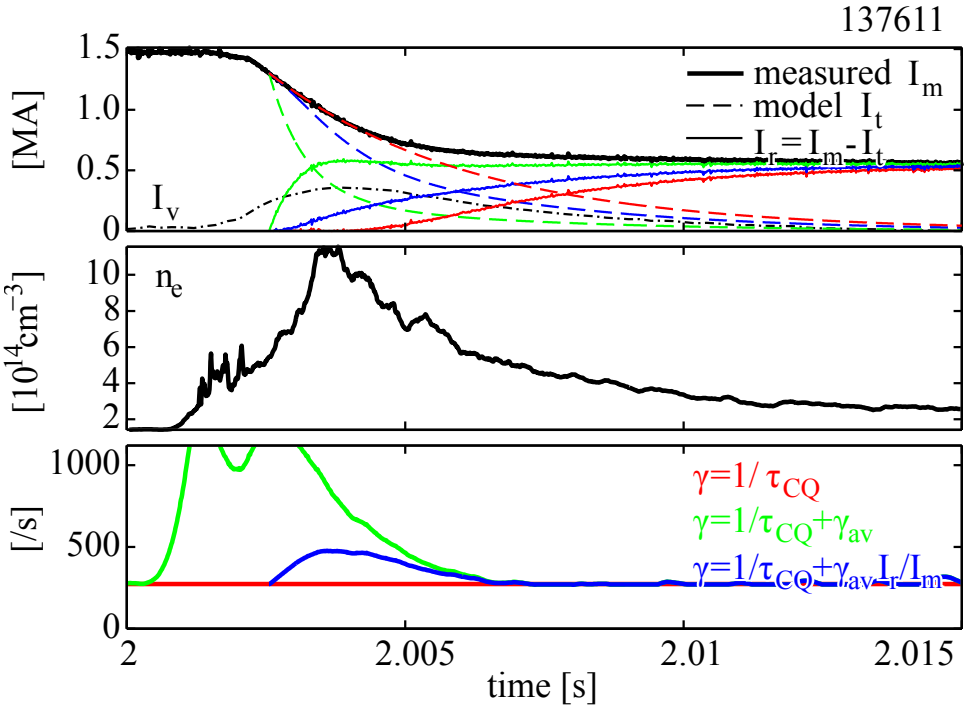

Figure D.1: Runaway electron current I_r calculated by subtracting three different models for thermal current I_t from total measured current I_m, with the density used to calculate the avalanche rate, and the effective time dependent rates for each of the three models. Vessel current I_v is also shown for comparison with the following model.

The avalanche process is modelled by a standard lumped circuit system of coupled resistive inductors building on a similar model developed by other authors [65, 21, 59, 63, 133]. The below model differs from prior work by using appropriate mutual inductances, and explicitly subtracting the avalanche flux consumption (the last term in equation D.1) from thermal flux so that total flux and magnetic energy are conserved when neglecting dissipation.

Self inductances for the thermal and runaway current are assumed identical $L_t = L_r = \mu_0 \ell_i R/2 = 1.05\mu H$ as calculated for a midplane current filament at $R = 1.67m$ with $\ell_i = 1$. Thermal current resistance is calculated semi-empirically as the ratio of the above assumed inductance and the measured current quench time $\tau_{CQ} = 3.7ms$: $R_t = L_t/\tau_{CQ} = 0.289m\Omega$. The vessel inductance is calculated for the wall mode driven by a temporal change in current at the assumed midplane filament: $L_v = 8.4\mu H$, and the vessel resistance calculated for the same mode is $R_v = 4m\Omega$. Mutual inductances between the driven vessel mode and thermal current are calculated as: $M_{tv} = M_{vt} = 1.54\mu H$. This system describes the transfer of flux between thermal (t), vessel (v), and runaway (r) currents, as shown below:

$$L_t \frac{dI_t}{dt} + M_{tv} \frac{dI_v}{dt} = -I_t R_t - L_r I_r \frac{I_t R_t}{V_{av}} \gamma_0 \tag{D.1}$$

$$M_{vt} \frac{dI_t}{dt} + L_v \frac{dI_v}{dt} = -I_v R_v \tag{D.2}$$

$$+L_r \frac{dI_r}{dt} = L_r I_r \left(\frac{I_t R_t}{V_{av}} - 1 \right) \gamma_0 \tag{D.3}$$

Integrating this model using a numerical ODE solver from initial conditions of $I_{m0} = 1.5MA$, $I_{v0} = 0A$ and $I_{r0} = 50kA$ results in time histories for each of the three currents shown in figure D.2, which are similar to experimental observations with one exception. The calculated wall current is notably almost a factor of two smaller than experimentally observed, indicating that the mutual inductance or other wall parameters used may differ somewhat from reality.

When accounting appropriately for dissipation and coupling, magnetic en-

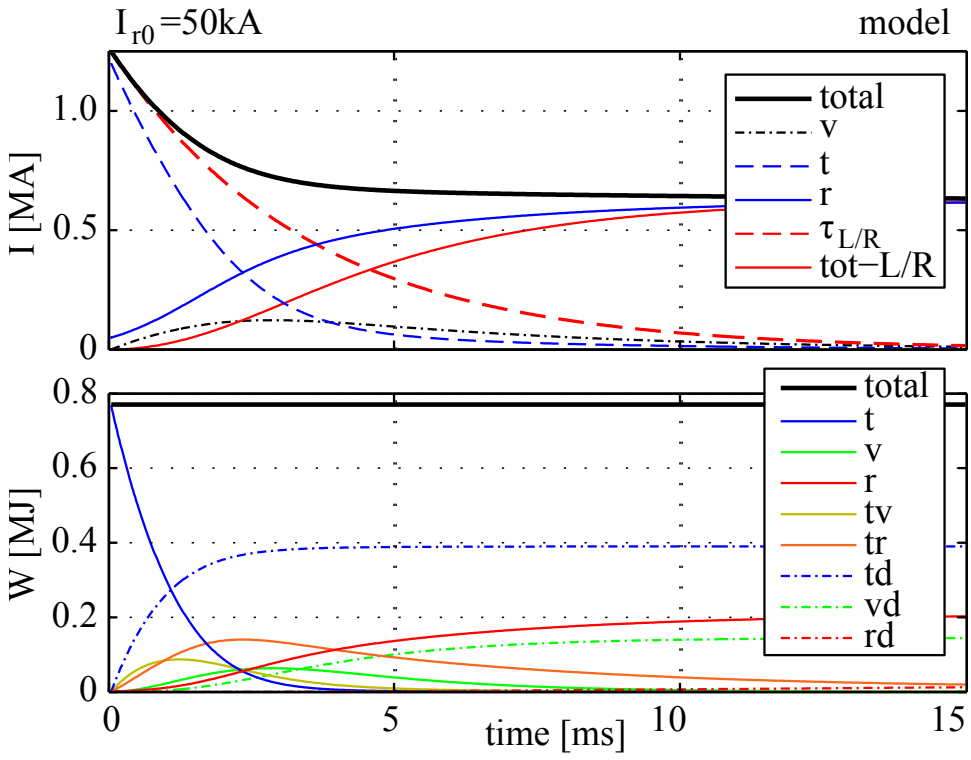

Figure D.2: Current and magnetic energy histories for the avalanche model. An exponential fit to the CQ and the subtraction of this fit from total measured current are shown dashed for comparison with modeled quantities.

ergy is explicitly conserved

$$\begin{aligned} dW/dt =& L_t I_t^2/2 + L_v I_v^2/2 + L_r I_r^2/2 \\ &+ M_{vt} I_v I_t + \int \frac{L_r R_t \gamma_0}{V_{av}} (I_t^2 I_r - I_t I_r^2) dt \\ &+ \int (I_t^2 R_t + I_v^2 R_v + I_r^2 L_r \gamma_0) dt = 0 \end{aligned} \tag{D.4}$$

The first three terms represent the magnetic energy stored in thermal, vessel, and runaway currents respectively. The middle three terms represent magnetic energy coupled between the thermal and vessel currents, and the thermal and runaway currents respectively. The last three terms represent dissipation of magnetic energy by resistance in thermal, vessel, and runaway currents. The time integral of each of these terms is plotted explicitly in figure D.2.

Comparison of figures D.1 and D.2, where the red curves are calculated using the same approach, reveals that the numerical model for avalanche most closely matches the third model for empirically calculating RE current.

D.3 Calculation of runaway electron seed current

The amount of initial RE seed current I_{r0} can be calculated from the expression for runaway gain [132]:

$$G \equiv \frac{I_r}{I_{r0}} = \exp\left(\frac{e}{m_e c \bar{p}} \int_0^\infty (E_\phi - E_A) dt\right) \tag{D.5}$$

where $\bar{p} \equiv \sqrt{3(Z+5)/\pi} ln\Lambda(Z)$ is the normalized momentum.

Some simplifying assumptions are helpful for evaluating this expression in experiments. Since no measure of the effective charge state exists, it is here assumed $Z = 1$, so that $\bar{p} = 29.7$. The critical field for avalanche E_A can be neglected since it is typically small compared with the fields occurring during a CQ. Additionally, the integration is evaluated for $15ms$ from the time the rapid-shutdown is triggered, which is long enough to capture roughly all of the CQ loop voltage. The final RE current I_r is assumed equal to the total measured current at the end

of this $15ms$ integration time, since any remaining thermal current would have mostly dissipated at that point. Using the same set of plasma discharges described in section 3.1, the quantities I_r and $\int E_\phi dt$ were both calculated for each shot as shown in figure D.3a.

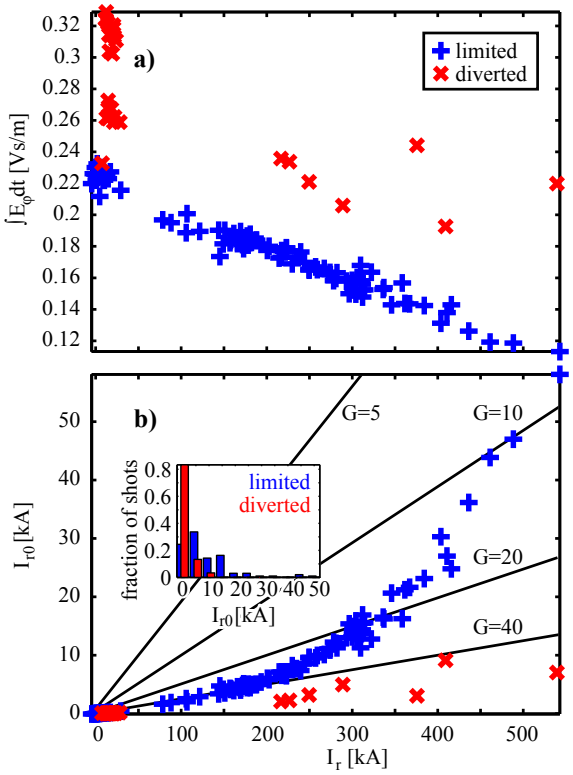

Figure D.3: a) Integrated toroidal field plotted versus the final RE current, and b) initial seed RE current plotted from these versus final RE current.

The RE seed current calculated using this technique ranges from nearly zero to more than $I_{r0} = 50kA$, with the apparent gain varying substantially, as shown in figure D.3b. Greatest gain is seen to occur for only the smallest RE seeds, with the largest calculated values of $G = 98$ for the limited configuration and $G = 659$ for the diverted configuration. Smaller RE gains are believed to occur for larger RE currents as a result of RE 'shorting out' the toroidal electric field.

Though the maximum gain is smaller in the limited configuration than in the diverted configuration, RE seed current is larger on average in the limited configuration as shown in the inlay histogram in figure D.3b. This larger apparent

seed current is consistent with the improved RE seed confinement in the limited configuration discussed in sections 4.2.2 and 4.2.5.

Bibliography

[1] *Data from NIFS DATABASE.*

[2] Special edition on plasma diagnostics for magnetic fusion research. *Fusion Science and Technology*, 53(2), 2008.

[3] Deaths per TWh by energy source. *Next Big Future*, 2011.

[4] Managing radioactive waste. *IAEA Factsheet*, 2011.

[5] F. Andersson. *Runaway Electrons in Tokamak Plasmas.* PhD thesis, Chalmers University of Technology, 2003.

[6] F. Andersson, P. Helander, and L.-G. Eriksson. Damping of relativistic electron beams by synchrotron radiation. *Physics of Plasmas*, 8(12):5221–5229, 2001.

[7] G. Arnoux. Heat load measurement on the JET first wall during disruptions. In *Proceedings of the 19th Plasma Surface Interactions Conference*, 2010.

[8] R Aymar, P Barabaschi, and Y Shimomura. The ITER design. *Plasma Physics and Controlled Fusion*, 44(5):519, 2002.

[9] M. Bakhtiari. Role of bremsstrahlung radiation in limiting the energy of runaway electrons in tokamaks. *Phys. Rev. Lett.*, 94(21):215003, Jun 2005.

[10] M. Bakhtiari, G. J. Kramer, and D. G. Whyte. Momentum-space study of the effect of bremsstrahlung radiation on the energy of runaway electrons in tokamaks. *Physics of Plasmas*, 12(10):102503, 2005.

[11] M. Bakhtiari, H. Tamai, Y. Kawano, G.J. Kramer, A. Isayama, T. Nakano, Y. Kamiya, R. Yoshino, Y. Miura, Y. Kusama, and Y. Nishida. Study of plasma termination using high-Z noble gas puffing in the JT-60U tokamak. *Nuclear Fusion*, 45(5):318, 2005.

[12] C.W. Barnes. *Studies of runaway electron transport in PLT and PDX.* PhD thesis, Princeton University, 1981.

[13] H. W. Bartels. Impact of runaway electrons. *Fusion Engineering and Design*, 23(4):323 – 328, 1994.

[14] L.R. Baylor, A. Geraud, W.A. Houlberg, D. Frigione, M. Gadeberg, T.C. Jernigan, J. De Kloe, P. Kupschus, B.V. Kuteev, P. Lang, A.A.M. Oomens, A.L. Qualls, K.N. Sato, and G.L. Schmidt. An international pellet ablation database. *Nuclear Fusion*, 37(4):445, 1997.

[15] M. J. Berger, J. S. Coursey, M. A. Zucker, and J. Chang. Stopping-power and range tables for electrons, protons, and helium ions. *NISTIR 4999*, 1993.

[16] M.J. Berger. XCOM: Photon cross sections database. *NIST Standard Reference Database 8 (XGAM)*, NBSIR 87-3597, 1998.

[17] H. L. Berk, T. K. Fowler, L. L. LoDestro, and L. D. Pearlstein. Hyperresistivity theory in a cylindrical plasma. *LLNL Internal Report UCRL-ID-142741*, 2001.

[18] Hans Bethe and Walter Heitler. On the stopping of fast particles and on the creation of positive electrons. *Proceedings of the Royal Society of London*, 146(856):83–112, 1934.

[19] M. C. Borrás, C. L. Fiore, K. W. Wenzel, and Y. Takase. Photon activation of the Alcator C-MOD limiter and RF antenna. *Review of Scientific Instruments*, 66(1):942–944, 1995.

[20] J.M. Boudry and L.E. Antonuk. Radiation damage of amorphous silicon photodiode sensors. *Nuclear Science, IEEE Transactions on*, 41(4):703 – 707, aug. 1994.

[21] S A Bozhenkov, M Lehnen, K H Finken, M W Jakubowski, R C Wolf, R Jaspers, M Kantor, O V Marchuk, E Uzgel, G Van Wassenhove, O Zimmermann, D Reiter, and the TEXTOR team. Generation and suppression of runaway electrons in disruption mitigation experiments in TEXTOR. *Plasma Physics and Controlled Fusion*, 50(10):105007, 2008.

[22] F. F. Chen. *Introduction to Plasma Physics and Controlled Fusion*. Plenum Press, New York and London, 1974.

[23] S.C. Chiu, M.N. Rosenbluth, R.W. Harvey, and V.S. Chan. Fokker-planck simulations mylb of knock-on electron runaway avalanche and bursts in tokamaks. *Nuclear Fusion*, 38(11):1711, 1998.

[24] Kurt Cobb. Does queueing theory explain oil's wild price swings? *Resource Insights*, 2008.

[25] N. Commaux. Novel rapid shutdown strategies for runaway electron suppression in DIII-D. *Submitted to Nucl. Fus.*, 2010.

[26] N. Commaux, L. R. Baylor, N. W. Eidietis, T. E. Evans, E. M. Hollmann, D. A. Humphreys, V. A. Izzo, A. N. James, P. B. Parks, J. C. Wesley, and J. H. Yu. Novel rapid shutdown strategies for runaway electron suppression in DIII-D. (CN-180/EXS/P2-02), 2010.

[27] A. M. Cormack. Representation of a function by its line integrals, with some radiological applications. *Journal of Applied Physics*, 34(9):2722–2727, 1963.

[28] R. C. Davidson, B. H. Hui, and C. A. Kapetanakos. Influence of self-fields on the filamentation instability in relativistic beam-plasma systems. *Physics of Fluids*, 18(8):1040–1044, 1975.

[29] H. Dreicer. *The extension of the kinetic theory of ionized gases to include coulomb interaction, elastic, and inelastic collisions with molecules.* PhD thesis, Massachusetts Institute of Technology, 1955.

[30] H. Dreicer. Electron and ion runaway in a fully ionized gas. I. *Phys. Rev.*, 115(2):238–249, 1959.

[31] H. Dreicer. Electron and ion runaway in a fully ionized gas. II. *Phys. Rev.*, 117(2):329–342, 1960.

[32] F. J. Dyson. *Disturbing The Universe.* Basic Books, New York, NY, 1979.

[33] N.A. Dyson. *X-rays in atomic and nuclear physics.* Longman Group Limited, London, 1973.

[34] I. Entrop. *Confinement of relativistic runaway electrons in tokamak plasmas.* PhD thesis, Technische Universiteit Eindhoven, 1999.

[35] T.E. Evans, D. G. Whyte, and P. L. Taylor. The production and confinement of runaway electrons with impurity Killer pellets in DIII-D. In *Proceedings of the International Atomic Energy Agency 17th Fusion Energy Conference*, number IAEA-F1-CN-69/EXP3/07, page 847, 1999.

[36] T Fehér, H M Smith, T Fülöp, and K Gál. Simulation of runaway electron generation during plasma shutdown by impurity injection in iter. *Plasma Physics and Controlled Fusion*, 53(3):035014, 2011.

[37] Tamás Fehér. *Simulation of runaway electron generation during plasma shutdown by impurity injection.* PhD thesis, Chalmers University of Technology, 2011.

[38] R. J. Fonck, A. T. Ramsey, and R. V. Yelle. Multichannel grazing-incidence spectrometer for plasma impurity diagnosis: SPRED. *Appl. Opt.*, 21(12):2115–2123, Jun 1982.

[39] J. P. Freidberg. Ideal magnetohydrodynamic theory of magnetic fusion systems. *Rev. Mod. Phys.*, 54(3):801–902, Jul 1982.

[40] J.P. Freidberg. *Ideal magnetohydrodynamics*. Plenum Press, 1987.

[41] G Fuchs, Y Miura, and M Mori. Soft x-ray tomography on tokamaks using flux coordinates. *Plasma Physics and Controlled Fusion*, 36(2):307, 1994.

[42] T. Fulop. Destabilization of magnetosonic-whistler waves by a relativistic runaway beam. In *Proceedings of the 33rd European Physical Society Conference*, 2006.

[43] G. Fussmann. On the motion of runaway electrons in momentum space. *Nuclear Fusion*, 19:327–334, March 1979.

[44] G. Fussmann, D. Campbell, A. Eberhagen, W. Engelhardt, F. Karger, M. Keilhacker, O. Klüber, K. Lackner, S. Sesnic, F. Wagner, K. Behringer, O. Gehre, J. Gernhardt, E. Glock, G. Haas, M. Kornherr, G. Lisitano, H. M. Mayer, D. Meisel, R. Müller, H. Murmann, H. Niedermeyer, W. Poschenrieder, H. Rapp, N. Ruhs, F. Schneider, G. Siller, and K. H. Steuer. Long-pulse suprathermal discharges in the ASDEX tokamak. *Phys. Rev. Lett.*, 47(14):1004–1007, Oct 1981.

[45] K Gál, T Fehér, H Smith, T F ul op, and P Helander. Runaway electron generation during plasma shutdown by killer pellet injection. *Plasma Physics and Controlled Fusion*, 50(5):055006, 2008.

[46] D.T. Garnier. *Lithium pellet injection experiments on the Alcator C-Mod Tokamak*. PhD thesis, Massachusetts Institute of Technology, 1996.

[47] K. Gill, G. Hall, and B. MacEvoy. Bulk damage effects in irradiated silicon detectors due to clustered divacancies. *Journal of Applied Physics*, 82(1):126–136, 1997.

[48] R. D. Gill. Generation and loss of runaway electrons following disruptions in JET. *Nuclear Fusion*, 33(11):1613, 1993.

[49] R. D. Gill. Direct observations of runaway electrons during disruptions in the JET tokamak. *Nucl. Fus.*, 40(2):163–174, 2000.

[50] R. S. Granetz and P. Smeulders. X-Ray tomography on JET. *Nuclear Fusion*, 28(3):457–476, Mar 1988.

[51] R. S. Granetz, D. G. Whyte, and V. A. Izzo. Studies of runaway electrons during disruptions in Alcator C-Mod. *APS Meeting Abstracts*, pages 3013–+, November 2008.

[52] R. S. Granetz, D. G. Whyte, and V. A. Izzo. Effect of plasma elongation on disruption runaway electrons. *APS Meeting Abstracts*, November 2009.

[53] D. S. Gray, E. M. Hollmann, S. C. Luckhardt, J. Chalfant, L. Chousal, R. Hernandez, E. Jones, and A. G. Kellman. Plasma radiometry with 30 chord resolution for fast transients in the DIII-D tokamak. *Review of Scientific Instruments*, 75(10):4133–4135, 2004.

[54] A. V. Gurevich. Runaway electron mechanism of air breakdown and preconditioning during a thunderstorm. *Phys. Lett. A*, 165:463–468, 1992.

[55] Aleksandr V Gurevich, A N Karashtin, Vladimir A Ryabov, Aleksandr P Chubenko, and Aleksandr L Shepetov. Nonlinear phenomena in the ionospheric plasma. effects of cosmic rays and runaway breakdown on thunderstorm discharges. *Physics-Uspekhi*, 52(7):735, 2009.

[56] D. A. Hammer and N. Rostoker. Propagation of high current relativistic electron beams. *Physics of Fluids*, 13(7):1831–1850, 1970.

[57] R. D. Hazeltine and J. D. Meiss. *Plasma confinement*. Dover press, 2003.

[58] W. W. Heidbrink. Measurements of the neutron source strength at DIII-D. *Rev. Sci. Inst.*, 68(1):536–539, 1997.

[59] P. Helander, F. Andersson, L.-G. Eriksson, T. Fülöp, H. Smith, D. Anderson, and M. Lisak. Runaway electron generation in tokamak disruptions. *Proceedings of the 20th IAEA Fusion Energy Conference*, (TH/P4-39), 2004.

[60] P. Helander, L.-G. Eriksson, and F. Andersson. Suppression of runaway electron avalanches by radial diffusion. *Physics of Plasmas*, 7(10):4106–4111, 2000.

[61] P Helander, L-G Eriksson, and F Andersson. Runaway acceleration during magnetic reconnection in tokamaks. *Plasma Physics and Controlled Fusion*, 44(12B):B247, 2002.

[62] E. M. Hollmann. Measurements of impurity and heat dynamics during noble gas jet-initiated fast plasma shutdown for disruption mitigation in DIII-D. *Nucl. Fus.*, 45:1046–1055, 2005.

[63] E. M. Hollmann. Effect of applied toroidal electric field on the growth/decay of plateau-phase runaway electron currents in diii-d. *Submitted to Nucl. Fus.*, 2010.

[64] E. M. Hollmann, N. Commaux, N. W. Eidietis, T. E. Evans, D. A. Humphreys, A. N. James, T. C. Jernigan, P. B. Parks, E. J. Strait, J. C. Wesley, J. H. Yu, M. E. Austin, L. R. Baylor, N. H. Brooks, V. A. Izzo, G. L. Jackson, M. A. van Zeeland, and W. Wu. Experiments in DIII-D toward achieving rapid shutdown with runaway electron suppression. *Physics of Plasmas*, 17(5):056117, 2010.

[65] E. M. Hollmann, P. B. Parks, and H. A. Scott. 0-d modeling of fast radiative shutdown of tokamak discharges following massive gas injection. *Contributions to Plasma Physics*, 48(1-3):260–264, 2008.

[66] M. K. Hubbert. Nuclear energy and the fossil fuels. In *Presented before the Spring meeting of the Souther District Division of Production*, 1956.

[67] D. A. Humphreys and N. Eidietis. Control of runaway electrons. *Submitted to Nucl. Fus.*, 2011.

[68] D. A. Humphreys and A. G. Kellman. Analytic modeling of axisymmetric disruption halo currents. *Physics of Plasmas*, 6(7):2742–2756, 1999.

[69] L.C. Ingesson, B. Alper, H. Chen, A.W. Edwards, G.C. Fehmers, J.C. Fuchs, R. Giannella, R.D. Gill, L. Lauro-Taroni, and M. Romanelli. Soft X ray tomography during ELMs and impurity injection in JET. *Nuclear Fusion*, 38(11):1675, 1998.

[70] A. N. Sekar Iyengar. Runaway electron studies in the startup phase of very low edge safety factor discharges in the SINP tokamak. *Nucl. Fus.*, 38(8):1177–1181, 1998.

[71] V.A. Izzo. Runaway electron confinement modeling for rapid shutdown scenarios in diii-d, alcator c-mod and iter. *Accepted to Nucl. Fus.*, 2011.

[72] V.A. Izzo, A.N. James, E.M. Hollmann, J.H. Yu, D.A. Humphreys, J.C. Wesley, L.L. Lao, P.B. Parks, P.E. Sieck, D.G. Whyte, G.M. Olynyk, and R.S. Granetz. Runaway electron confinement modeling for DIII-D, Alcator C-Mod and ITER. (CN-180/THS/9-2), 2010.

[73] G. L. Jackson, E. A. Lazarus, G. A. Navratil, R. Bastasz, N. H. Brooks, D. T. Garnier, K. L. Holtrop, J. C. Phillips, E. S. Marmar, T. S. Taylor, D. M. Thomas, W. R. Wampler, D. G. Whyte, and W. P. West. Enhanced performance discharges in the DIII-D tokamak with lithium wall conditioning. *Journal of Nuclear Materials*, 241-243:655 – 659, 1997.

[74] G.L. Jackson, T.A. Casper, T.C. Luce, D.A. Humphreys, J.R. Ferron, A.W. Hyatt, J.A. Leuer, T.W. Petrie, F. Turco, and W.P. West. Simulating ITER plasma startup and rampdown scenarios in the DIII-D tokamak. *Nuclear Fusion*, 49(11):115027, 2009.

[75] J.D. Jackson. *Classical Electrodynamics, 3rd Ed.*, chapter 14, pages 668–671. John Wiley and Sons, Inc., Hoboken, New Jersey, 1988.

[76] J.D. Jackson. *Classical Electrodynamics, 3rd Ed.*, chapter 14, page 679. John Wiley and Sons, Inc., Hoboken, New Jersey, 1988.

[77] J.D. Jackson. *Classical Electrodynamics, 3rd Ed.* John Wiley and Sons, Inc., Hoboken, New Jersey, 1988.

[78] A. N. James, M. E. Austin, N. Commaux, N. Eidietis, T. Evans, E. M. Hollmann, D. A. Humphreys, A. Hyatt, V. A. Izzo, T. C. Jernigan, R. J. La Haye, P. B. Parks, E. J. Strait, G. R. Tynan, J. C. Wesley, and J. H. Yu. Measurements of hard x-ray emission from runaway electrons in DIII-D. *to be submitted to Nuclear Fusion*, 2011.

[79] A. N. James, E. M. Hollmann, and G. R. Tynan. Spatially distributed scintillator arrays for diagnosing runaway electron transport and energy behavior in tokamaks. *Review of Scientific Instruments*, 81(10):10E306, 2010.

[80] A. N. James, E. M. Hollmann, J. H. Yu, M. E. Austin, N. Commaux, T. Evans, D. A. Humphreys, T. C. Jernigan, P. B. Parks, S. Putvinski, E. J. Strait, G. R. Tynan, and J. Wesley. Pellet interaction with runaway electrons. *Journal of Nuclear Materials*, In Press, Corrected Proof:–, 2011.

[81] A. Janos. Disruptions in the TFTR tokamak. In *Proceedings of the 15th International Atomic Energy Agency Fusion Energy Conference*, 1993.

[82] A. C. Janos, E. Fredrickson, M. Corneliussen, K. M. McGuire, M. Bell, A. Cavallo, Y. Nagayama, D. K. Owens, and M. Ulrickson. Disruptions in TFTR. *Journal of Nuclear Materials*, 176-177:773 – 778, 1990.

[83] R. Jaspers, N. J. Lopes Cardozo, A. J. H. Donne, H. L. M. Widdershoven, and K. H. Finken. A synchrotron radiation diagnostic to observe relativistic runaway electrons in a tokamak plasma. *Review of Scientific Instruments*, 72(1):466–470, 2001.

[84] R. Jaspers, N. J. Lopes Cardozo, K. H. Finken, B. C. Schokker, G. Mank, G. Fuchs, and F. C. Schüller. Islands of runaway electrons in the TEXTOR tokamak and relation to transport in a stochastic field. *Phys. Rev. Lett.*, 72(26):4093–4096, Jun 1994.

[85] R.J. Jaspers. *Relativistic runaway electrons in tokamak plasmas*. PhD thesis, Technische Universiteit Eindhoven, 1995.

[86] R. Jayakumar and H. H. Fleischmann. Density and energy distribution of epithermal secondary electrons in a plasma with fast charged particles. *Physics Letters A*, 139(7):313 – 317, 1989.

[87] R. Jayakumar, H. H. Fleischmann, and S. J. Zweben. Collisional avalanche exponentiation of runaway electrons in electrified plasmas. *Physics Letters A*, 172(6):447 – 451, 1993.

[88] Erik B. Johnson, Christopher J. Stapels, Xiao Jie Chen, Frank L. Augustine, and James F. Christian. Large-area CMOS solid-state photomultipliers and recent developments. *Nuclear Instruments and Methods in Physics Research Section A: Accelerators, Spectrometers, Detectors and Associated Equipment*, In Press, Corrected Proof:–, 2010.

[89] C. A. Kapetanakos. Filamentation of intense relativistic electron beams propagating in dense plasmas. *Applied Physics Letters*, 25(9):484–486, 1974.

[90] Yasunori Kawano, Tomohide Nakano, Akihiko Isayama, Nobuyuki Asakura, Hiroshi Tamai, Hirotaka Kubo, Hidenobu Takenaga, Mohammad Bakhtiari, Shunsuke Ide, Takashi Kondoh, and Takaki Hatae. Characteristics of post-disruption runaway electrons with impurity pellet injection. *J. Plasma Fusion Res.*, 81(8):593–601, 2005.

[91] I. Kawrakow. The EGSnrc Code System: Monte Carlo simulation of electron and photon transport. *NRCC Report*, PIRS-701, 2009.

[92] A. G. Kellman, J. W. Cuthbertson, T. E. Evans, D. A. Humphreys, A. W. Hyatt, G. L. Jahns, T. C. Jernigan, C. J. Lasnier, R. L. Lee, J. A. Leuer, S. Luckhardt, M. J. Schaffer, P. L. Taylor, D. G. Whyte, D. Wròblewski, and J. Zhang. Disruption studies in DIII-D. In *Proceedings of the International Atomic Energy Agency 16th Fusion Energy Conference*, number IAEA-F1-CN-64/AP1-20, 1996.

[93] H. Knoepfel and D.A. Spong. Runaway electrons in toroidal discharges. *Nuclear Fusion*, 19(6):785, 1979.

[94] G.F. Knoll. *Radiation detection and measurement*. John Wiley & Sons, New York, NY, 2000.

[95] A V Korol, O I Obolensky, A V Solov'yov, and I A Solovjev. The full relativistic description of the bremsstrahlung process in a charged particle-atom collision. *Journal of Physics B: Atomic, Molecular and Optical Physics*, 34(9):1589, 2001.

[96] H. A. Kramers. On the theory of x-ray absorption and of the continuous x-ray spectrum. *Philosophical Magazine*, 46(275):836 – 871, 1923.

[97] T. Kudyakov. Measurements of runaway electrons in the TEXTOR tokamak. In *Proceedings of the 36th European Physical Society Conference*, 2009.

[98] T. Kudyakov. *Spectral measurements of runaway electrons in the TEXTOR tokamak*. PhD thesis, Heinrich-Heine-Universität Düsseldorf, 2009.

[99] T. Kudyakov, K. H. Finken, M. W. Jakubowski, M. Lehnen, Y. Xu, B. Schweer, T. Toncian, G. Van Wassenhove, O. Willi, and the TEXTOR team. Spatially and temporally resolved measurements of runaway electrons in the TEXTOR tokamak. *Nuclear Fusion*, 48(12):122002, 2008.

[100] R.M. Kulsrud. *Plasma physics for astrophysics*. Princeton University Press, 2005.

[101] B. Kuteev, V. Skokov, V. Sergeev, V. Timokhin, S. Krylov, Yu. Pavlov, A. Ponomarev, V. Pustovitov, D. Sarychev, and L. Khimchenko. Threshold effects in the interaction of a plasma with injected pellets in the t-10 tokamak. *JETP Letters*, 84:239–242, 2006. 10.1134/S0021364006170024.

[102] O.J. Kwon, P.H. Diamond, F. Wagner, G. Fussmann, ASDEX Team, and NI Team. A study of runaway electron confinement in the ASDEX tokamak. *Nuclear Fusion*, 28(11):1931, 1988.

[103] M. Lamoureux and P. Charles. General deconvolution of thin-target and thick-target bremsstrahlung spectra to determine electron energy distributions. *Radiation Physics and Chemistry*, 75(10):1220 – 1231, 2006. Bremsstrahlung: Theory and Experiment.

[104] M. Lamoureux, P. Waller, P. Charles, and N. B. Avdonina. Bremsstrahlung from thick targets and a diagnostic for electron energy distributions. *Phys. Rev. E*, 62(3):4091–4095, Sep 2000.

[105] L. L. Lao, H. E. St. John, Q. Peng, J. R. Ferron, E. J. Strait, T. S. Taylor, W. H. Meyer, C. Zhang, and K. I. You. MHD equilibrium reconstruction in the DIII-D tokamak. *Fusion Science and Technology*, 48(2):968–977, 2005.

[106] L. L. Lao, H. St. John, R. D. Stambaugh, and W. Pfeiffer. Separation of β_p and ℓ_i in tokamaks of non-circular cross-section. *Nuclear Fusion*, 25(10):1421, 1985.

[107] M. Lehnen. Runaway generation during disruptions in JET and TEXTOR. *Journal of Nuclear Materials*, 390–391:740–746, 2009.

[108] M. Lehnen, S. A. Bozhenkov, S. S. Abdullaev, and M. W. Jakubowski. Suppression of runaway electrons by resonant magnetic perturbations in textor disruptions. *Phys. Rev. Lett.*, 100(25):255003, Jun 2008.

[109] Nikolai Lehtinen. *Relativistic Runaway Electrons Above Thunderstorms*. PhD thesis, Stanford, 2000.

[110] L.L. Lengyel, K. Bchl, G. Pautasso, L. Ledl, A.A. Ushakov, S. Kalvin, and G. Veres. Modelling of impurity pellet ablation in ASDEX Upgrade (neon) and Wendelstein W7-AS (carbon) by means of a radiative ('killer') pellet code. *Nuclear Fusion*, 39(6):791, 1999.

[111] W.R. Leo. *Techniques for nuclear and particle physics experiments: a how-to approach*. Springer-Verlag, Berlin, Heidelberg, 1994.

[112] J.D. Lindl. *Inertial confinement fusion: the quest for ignition and energy gain using indirect drive*. AIP Press, 1998.

[113] M. Lipa, G. Martin, R. Mitteau, V. Basiuk, M. Chatelier, J. J. Cordier, and R. Nygren. Effects of supra-thermal particle impacts on Tore Supra plasma facing components. *Fusion Engineering and Design*, 66-68:365 – 369, 2003. 22nd Symposium on Fusion Technology.

[114] John Lohr. Electron density measurements from cutoff of electron cyclotron emission in the DIII-D tokamak. *Review of Scientific Instruments*, 59(8):1608–1610, 1988.

[115] H. W. Lu, L. Q. Hu, S. Y. Lin, S. F. Wang, G. Q. Zhong, and the HT-7 team. Runaway electron measurements in the east tokamak. *Contributions to Plasma Physics*, 50(2):141–145, 2010.

[116] J. L. Luxon. A design retrospective of the DIII-D tokamak. *Nuclear Fusion*, 42(5):614, 2002.

[117] G. Martin, F. Sourd, F. Saint-Laurent, J. Bucalossi, and L. G. Eriksson. Disruption Mitigation on Tore Supra. *Proceedings of the 20th IAEA Fusion Energy Conference*, (EX/10-6Rc), 2004.

[118] M McPherson, B K Jones, and T Sloan. Effects of radiation damage in silicon P-I-N photodiodes. *Semiconductor Science and Technology*, 12(10):1187, 1997.

[119] K. R. Middaugh, B. D. Bray, C. L. Hsieh, B. B. McHarg, and B. G. Penaflor. DIII-D Thomson scattering diagnostic data acquisition, processing, and analysis software. *IEEE Transactions on Nuclear Science*, 47:263–266, April 2000.

[120] C. Møller. Über den sto zweier teilchen unter berücksichtigung der retardation der kräfte. *Zeitschrift für Physik A Hadrons and Nuclei*, 70:786–795, 1931.

[121] C. Møller. Zur theorie des durchgangs schneller elektronen durch materie. *Annalen der Physik*, 406(5):531–585, 1932.

[122] Alfred Mondelli and Edward Ott. Straight and toroidal plasma equilibria with an intense relativistic electron current component. *Physics of Fluids*, 17(5):1017–1025, 1974.

[123] H. E. Mynick and J. D. Strachan. Transport of runaway and thermal electrons due to magnetic microturbulence. *Physics of Fluids*, 24(4):695–702, 1981.

[124] Werner Nakel. The elementary process of bremsstrahlung. *Physics Reports*, 243(6):317 – 353, 1994.

[125] Ramesh Narayanan and A N Sekar Iyengar. Comparative study of runaway electron diusion in the rise phase of low q_a and normal q_a discharges in the SINP tokamak. *Pramana Journal of Physics*, 75(4):691–708, 2010.

[126] R. Nygren, T. Lutz, D. Walsh, G. Martin, M. Chatelier, T. Loarer, and D. Guilhem. Runaway electron damage to the Tore Supra phase III outboard pump limiter. *Journal of Nuclear Materials*, 241-243:522 – 527, 1997.

[127] CINDA: Bibliographical Information on nuclear reaction data.

[128] Bhooshan Paradkar, J. Ghosh, P. K. Chattopadhyay, R. L. Tanna, D. Raju, S. B. Bhatt, C. V. S. Rao, Sankar Joisa, Santanu Banerjee, R. Manchanda, C. N. Gupta, Y. C. Saxena, and Aditya Team. Runaway-loss induced negative and positive loop voltage spikes in the Aditya tokamak. *Physics of Plasmas*, 17(9):092504, 2010.

[129] V. V. Parail and O. P. Pogutse. The kinetic theory of runaway electron beam instability in a tokamak. *Nuclear Fusion*, 18:303–314, March 1978.

[130] V. V. Parail and O. P. Pogutse. Runaway electrons in a tokamak. volume 11 of *Reviews of Plasma Physics*, 1986.

[131] R. L. Parker. *Geophysical inverse theory*. Princeton University Press, Princeton, NJ, 1994.

[132] P. B. Parks. A handy formula for surveying runaway electron seed currents levels using the MGI experimental data base. Internal Communication.

[133] P. B. Parks. On an improved torus inductance model for kprad code. Internal Communication, 2006.

[134] P. B. Parks. Personal Correspondence, 2011.

[135] P. B. Parks and R. J. Turnbull. Effect of transonic flow in the ablation cloud on the lifetime of a solid hydrogen pellet in a plasma. *Physics of Fluids*, 21(10):1735–1741, 1978.

[136] G. Pautasso, D. Coster, X. Bonnin, T. Eich, J.C. Fuchs, B. Kurzan, K. McCormick, B. Reiter, and V. Rohde. Disruption mitigation in ASDEX Upgrade with the in-vessel fast valve. *Proceedings of the 22nd IAEA Fusion Energy Conference*, (EX/P9-1), 2008.

[137] G. Pautasso, Y. Zhang, B. Reiter, L. Giannone, A. Herrmann, O. Kardaun, V.E. Lukash, M. Maraschek, Y. Nakamura, G.Sias, and M. Sugihara. Contribution of ASDEX Upgrade to disruption studies for ITER. *Proceedings of the 23rd IAEA Fusion Energy Conference*, (EXS/P2-15), 2010.

[138] Huba Beam Physics, J. D. Huba, and Beam Physics Branch. NRL Plasma Formulary, 2002.

[139] V. V. Plyusnin. Study of runaway electron generation during major disruptions in JET. *Nucl. Fus.*, 46:277–284, 2006.

[140] V. D. Pustovitov. Magnetic diagnostics: General principles and the problem of reconstruction of plasma current and pressure profiles in toroidal systems. *Nuclear Fusion*, 41(6):721, 2001.

[141] S. Putvinski. Evaporation of beryllium pellets in iter plasmas. *ITER internal report - ITER-D-2MJPGH*, 2009.

[142] S Putvinski, P Barabaschi, N Fujisawa, N Putvinskaya, M N Rosenbluth, and J Wesley. Halo current, runaway electrons and disruption mitigation in ITER. *Plasma Physics and Controlled Fusion*, 39(12B):B157, 1997.

[143] A. B. Rechester. Electron heat transport in a tokamak with destroyed magnetic flux surfaces. *Phys. Rev. Lett.*, 40(1):38–41, 1978.

[144] P Reynolds and H M Skarsgard. A plasma betatron. *Journal of Nuclear Energy. Part C, Plasma Physics, Accelerators, Thermonuclear Research*, 1(1):36, 1959.

[145] M. Rosenbluth and S. Putvinski. Theory for avalanche of runaway electrons in tokamaks. *Nucl. Fus.*, 37(10):1355–1362, 1997.

[146] F. Saint-Laurent. Control of runaway electron beams on Tore-Supra. In *Proceedings of the 36th European Physical Society Conference*, 2009.

[147] D. P. Schissel, R. E. Stockdale, H. St. John, and W. M. Tang. Measurements and implications of Z_{eff} profiles on the DIII-D tokamak. *Physics of Fluids*, 31(12):3738–3743, 1988.

[148] V. Y. Sergeev, O. A. Bahaeva, B. V. Kuteev, and M. Tendler. Studies of the impurity pellet ablation in the high-temperature plasma of magnetic confinement devices. *Plas. Phys. Rep.*, 32(5):363–377, May 2006.

[149] V. D. Shafranov. On Magnetohydrodynamical Equilibrium Configurations. *Soviet Journal of Experimental and Theoretical Physics*, 6:545–+, 1958.

[150] H. M. Skarsgard and J. V. Gore. High field air-cored betatron used to investigate intense runaway electron streams. *Review of Scientific Instruments*, 36(12):1807–1812, 1965.

[151] H M Smith, T Fehér, T Fülöp, K Gál, and E Verwichte. Runaway electron generation in tokamak disruptions. *Plasma Physics and Controlled Fusion*, 51(12):124008, 2009.

[152] H M Smith and E Verwichte. Hot tail runaway electron generation in tokamak disruptions. *Physics of Plasmas*, 15(7):072502, 2008.

[153] R. T. Snider, R. Evanko, and J. Haskovec. Toroidal and poloidal soft x-ray imaging system on the DIII-D tokamak. *Review of Scientific Instruments*, 59(8):1807–1809, 1988.

[154] Y. A. Sokolov. "Multiplication" of accelerated electrons in a tokamak. *JETP Lett.*, 29(4):218–221, 1979.

[155] Lyman Spitzer and Richard Härm. Transport phenomena in a completely ionized gas. *Phys. Rev.*, 89(5):977–981, Mar 1953.

[156] E. J. Strait. Magnetic diagnostic system of the DIII-D tokamak. *Review of Scientific Instruments*, 77(2):023502, 2006.

[157] E. J. Strait, E. D. Fredrickson, J.-M. Moret, and M. Takechi. Magnetic Diagnostics. *Fusion Science and Technology*, 53(2):304–334, 2008. Special issue on plasma diagnostics for magnetic fusion research.

[158] D.W. Swain and G.H. Neilson. An efficient technique for magnetic analysis of non-circular, high-beta tokamak equilibria. *Nuclear Fusion*, 22(8):1015, 1982.

[159] H. Tamai. Runaway current termination in JT-60U. *Nucl. Fus.*, 42:290–294, 2002.

[160] P. L. Taylor. Evidence of runaway electron activation of limiters in may 2010 vent. Internal Communication, 2010.

[161] H. Tsuchiya, T. Enoto, S. Yamada, T. Yuasa, M. Kawaharada, T. Kitaguchi, M. Kokubun, H. Kato, M. Okano, S. Nakamura, and K. Makishima. Detection of high-energy gamma rays from winter thunderclouds. *Phys. Rev. Lett.*, 99(16):165002, Oct 2007.

[162] V. M. Vasyliunas. Upper limit on the electric field along a magnetic o line. *Jour. Geophys. Res.*, 85(A9):4616–4620, 1980.

[163] G. Wang, E. J. Doyle, W. A. Peebles, L. Zeng, T. L. Rhodes, S. Kubota, X. Nguyen, and N. A. Crocker. High-resolution dual-polarization frequency modulated reflectometer density profile measurements on DIII-D. *Review of Scientific Instruments*, 75(10):3800–3803, 2004.

[164] J. D. Wesson. *Tokamaks*, chapter 3.3. Clarendon Press, Oxford, 3rd edition, 2004.

[165] J. D. Wesson. *Tokamaks*. Clarendon Press, Oxford, 3rd edition, 2004.

[166] D.G. Whyte. Energy balance, radiation and stability during rapid plasma termination via impurity pellet injections on DIII-D. In *Proc. of 24th European Conference on Controlled Fusion and Plasma Physics*, page 1137, 1997.

[167] C. T. R. Wilson. The acceleration of β-particles in strong electric fields such as those of thunderclouds. *Mathematical Proceedings of the Cambridge Philosophical Society*, 22(04):534–538, 1925.

[168] W. Wu, P. B. Parks, and V. A. Izzo. 1-D Modeling of Massive Particle Injection (MPI) in Tokamaks. *APS Meeting Abstracts*, pages 3013–+, November 2008.

[169] G. A. Wurden. The Real Mission of ITER. *APS Meeting Abstracts*, pages 4004–+, November 2009.

[170] Zensho Yoshida. A self-consistent equilibrium model of plasma–beam systems. *Physics of Fluids B: Plasma Physics*, 1(8):1702–1708, 1989.

[171] R. Yoshino and S. Tokuda. Runaway electrons in magnetic turbulence and runaway current termination in tokamak discharges. *Nuclear Fusion*, 40(7):1293, 2000.

[172] R. Yoshino, S. Tokuda, and Y. Kawano. Generation and termination of runaway electrons at major disruptions in JT-60U. *Nuclear Fusion*, 39(2):151, 1999.

[173] J. H. Yu. Fast camera observations of runaway electrons in DIII-D disruptions, 2011.

[174] M. A. Van Zeeland, R. L. Boivin, T. N. Carlstrom, T. Deterly, and D. K. Finkenthal. Fiber optic two-color vibration compensated interferometer for plasma density measurements. *Review of Scientific Instruments*, 77(10):10F325, 2006.

[175] Q.-G. Zong. Energetic electron response to ULF waves induced by interplanetary shocks in the outer radiation belt. *J. Geophys. Res.*, 114(A10204), 2009.

[176] S. J. Zweben. *A Investigation of High Energy Runaway Electron Confinement in the Oak Ridge Tokamak*. PhD thesis, Cornell University, May 1978.

[177] S. J. Zweben, D. W. Swain, H. H. Fleischmann, and B. V. Waddell. High-energy runaway orbits in the presence of an m = 2 magnetic island. *Nuclear Fusion*, 20:477–482, April 1980.